
High Performance Polyamide Nanocomposite Membranes for Water Desalination

Dissertation

zur Erlangung des akademischen Grades eines Doktors der Naturwissenschaften

- Dr. rer. nat.-

vorgelegt von

Ahmed Mohamed Abdelhamid Abdelsamad

geboren in Bani Souwaif, *Ägypten*

Fakultät für Chemie

der

Universität Duisburg-Essen

Essen 2019

DuEPublico

Duisburg-Essen Publications online

UNIVERSITÄT
DUISBURG
ESSEN

Offen im Denken

ub | universitäts
bibliothek

Diese Dissertation wird über DuEPublico, dem Dokumenten- und Publikationsserver der Universität Duisburg-Essen, zur Verfügung gestellt und liegt auch als Print-Version vor.

DOI: 10.17185/duepublico/70337

URN: urn:nbn:de:hbz:464-20190815-110352-8

Alle Rechte vorbehalten.

Dedication

this thesis is dedicated with all love to my wife (Nada) and my wonderful children (Suhib and Ali) for their love, patience and sacrifice provided over the time of this study

Approved by the examining committee on July 11, 2019 (the date of oral examination)

Chair: **Prof. Dr. Alexander Probst**

Advisor: **Prof. Dr. Mathias Ulbricht**

Reviewer: **Prof. Dr. Stephan Barcikowski**

The work presented here was carried out in the period from April 2015 till October 2018 at the Department of Technical Chemistry II – Faculty of Chemistry – University of Duisburg-Essen, under supervision of Prof. Dr. Mathias Ulbricht.

Hereby, I declare that this dissertation represents my own work, except where due acknowledgement is made.

Signature: *Ahmed.. Abdelsamad...*

- Ahmed Abdelsamad -

Abstract

Thin film nanocomposite (TFN) membranes contain nanoparticles in the thin polyamide (PA) top layer, resulting in a remarkable increase in water permeability without compromising the salt rejection. Mesoporous silica nanoparticles (MSN) have gained much attention as nanofillers for improved performance PA TFN membranes. However, aggregation of MSN inside the PA layer and their tendency to fast dissolution in aqueous solutions are serious challenges which strongly affect the separation performance of MSN-based TFN membranes. In this work, these challenges were addressed by controlling the functionalization of MSN with hydrophobic organo-silane, such as octadecyltrichlorosilane (OTS) or methyltrichlorosilane (MTS), before incorporating in the PA layer. MSN were synthesized first by sol-gel process and then functionalized using post-grafting method during silanization reaction. The functionalization was tuned in order to allow the hydrophobic alkyl group of the silane molecule to graft both the external surface of MSN as well as their interior pores or to modify only their external surface depending on the functionalization procedure and the silane concentration. The model of functionalization and the amount of OTS or MTS grafted on the surface were estimated through the nitrogen adsorption measurement and thermogravimetric analysis. The functionalized MSN with a particle diameter of ≈ 80 nm were thereafter easily dispersed in the organic solvent during the TFN membrane preparation via interfacial polymerization method. The membrane performance was then assessed based on water permeability and salt rejection measurements. Several parameters were found to have a strong influence on the membrane performance such as concentration of grafted OTS or MTS and the NPs loading inside the PA layer. The low aggregation and good integration of the functionalized nanofillers inside the PA layer produced TFN membranes with superior initial water permeability. The results revealed that the initial water permeability of the TFN membranes with OTS functionalized MSN achieved $\approx 65\%$ higher initial permeability than the reference TFC membrane at the optimum OTS amount and NPs loading, without sacrificing the membrane selectivity. Whereas the corresponding TFN membranes with MTS functionalized MSN achieved $\approx 130\%$ higher permeance but with 2% less salt rejection than the reference TFC membrane at the same conditions. The controlled functionalization of MSN nanofillers not only can improve membrane performance but also can provide a deeper understanding of the role of porous structure of MSN on the separation mechanism. This work clearly emphasizes the direct relationship between the internal pores of MSN inside the PA barrier layer and increasing or decreasing the water permeability of resulting TFN membranes. Furthermore, it was investigated, how hydrophobic functionalization of MSN can improve the stability of MSN in

aqueous solutions and improve the stability of the respective TFN membranes over prolonged filtration time at different pH values. The results showed that TFN membranes containing the OTS-functionalized MSN had only $\approx 6\%$ (or 7.5% for MTS-functionalized MSN) decline in salt rejection compared to 34.5% decline for the membrane containing unfunctionalized nanofillers accompanied by increasing in water permeability after 240 h filtration time (120 h at pH 5 then 120 h at pH 9). According to these results, it was concluded that the functionalized MSN have low dissolution tendency due to the formation of a protective organic layer leading to enhanced long-time stability of the TFN membranes. Finally, the durability of the barrier layer after a prolonged use for desalination performance of PA TFN membranes was also investigated.

Acknowledgement

I gladly offer these honorable mentions addressed to all great persons who have positively influenced on the progress of my thesis work as well as my personal development.

First and foremost, I would like to thank my advisor **Prof. Dr. Mathias Ulbricht**, the person who gave me the opportunity to go through my doctoral work in his group. Without his enthusiastic supervision, inspiration, guidance, the completion of this thesis would not have been possible. I appreciate all his contributions of time, ideas and his endless support. Words cannot express the deepness of my gratitude to him.

I would like to thank the Egyptian Ministry of Higher Education (**MoHE**) and the German Academic Exchange Service (**DAAD**) for the financial support through German Egyptian Research Long- Term Scholarship “GERLS”, and I thank the support introduced from the **university of Duisburg-Essen** through the graduation grant.

I also want to thank Prof. Dr. Stephan Barcikowski for kindly reviewing my thesis and Prof. Dr. Alexander Probst for kindly being the chair of my defense committee.

I would like also to express my deep gratitude to Dr. Ahmed S. G. Khalil, who guided me to work in the field of membrane technology. I thank him for his sincere advice, supporting and motivating me. I owe him a big part of my success.

I am grateful to Dipl.-Ing. Danielzik Inge, Dipl.-Ing. Kallweit Tobias and Claudia Schenk for their technical support during the course of this work. My great thanks also go to Mrs. Roswitha Nordmann for her kind help.

Furthermore, I am very thankful to all the current and former friends, and colleagues at the department of Technical Chemistry II for the friendly and motivating working atmosphere. In particular, my dear friend Ibrahim ElSherbiny for his support, suggestions and the inspiring discussion on my work. I would also like to thank Alexander Dundua, Miao Li and Mohamed Elleithy for their often fruitful discussions. Special thanks are devoted to Xi Lin, Qirong Ke, Patrick May for their sincere support and great help. I would like also to thank Marcel Matthias for working together during his practice work and master thesis. My grateful thanks are also extended to, Jan Wiczorek, Clemens Alexowsky, Inga Frost, Marta Bojarska, Thorsten van den Berg, Dominic Büning, and Clelia Emin for their help and also for enjoyable time we spent together. In parallel, my great appreciation is going to my colleagues and friends from National Research Center (NRC), Egypt, in particular, my best friend Mohamed Hamed, Dr. Tarek Gad-Allah, and Mahmoud Abdel Wahed, for their endless support.

Finally, my deep thanks go to my beloved parents and my siblings for their prayers and spiritual support and the most gratefulness is to my Lord Allah, for his protection and the privilege of knowing him

Two scientific papers have been published out of this work:

1. **A.M.A. Abdelsamad**, A.S.G. Khalil, M. Ulbricht, Influence of controlled functionalization of mesoporous silica nanoparticles as tailored fillers for thin-film nanocomposite membranes on desalination performance, *Journal of Membrane Science*. 563 (2018) 149.
2. **A.M.A. Abdelsamad**, M. Matthias, A.S.G. Khalil, M. Ulbricht, Nanofillers dissolution as a crucial challenge for the performance stability of thin-film nanocomposite desalination membranes, *Separation and Purification Technology* 228 (2019) 115767

List of contents

Abstract	i
Acknowledgement	iii
List of contents	vi
1. Introduction	1
1.1 Aim of the work	3
1.2 Objectives and structure of the thesis	5
2. Theory and Literature review	7
2.1 Membrane-based process for water treatment	7
2.2 Water desalination technologies	7
2.3 Reverse Osmosis	8
2.3.1 Principals and applications of RO	9
2.3.2 Conventional polymeric RO membrane materials	10
2.3.3 Thin film composite (TFC) membranes	10
2.3.4 Fabrication and structure of polyamide (PA) TFC RO membranes	11
2.3.5 Membrane transport theories	12
2.3.5.1 Solution-diffusion model (SDM)	13
2.3.5.2 Factors contribute to transport	14
2.3.6 Challenges of TFC membranes	18
2.3.6.1 Trade-off relationship between permeance and salt rejection	18
2.3.6.2 Fouling	18
2.3.6.3 Chlorination	18
2.3.7 Strategies to improve membrane performance and antifouling properties	18
2.3.7.1 Optimization the preparation conditions	18
2.3.7.2 Optimization the support membrane	20
2.3.7.3 Surface modification	21
2.3.7.4 Aquaporin_based PA RO membranes	22
2.4 Thin film nanocomposite (TFN) membranes	23
2.4.1 Overview of TFN membranes	23
2.4.2 TFN membranes fabrication	26
2.4.3 Chemical, mechanical and antifouling properties of TFN membranes	28
2.4.4 Separation mechanism of TFN membranes	28

2.5 Mesoporous silica nanoparticles (MSN) as nanofiller	30
2.5.1 Classification of porous materials	31
2.5.2 Overview of MSN history	33
2.5.3 Synthesis of MSN	35
2.5.3.1 Factors affect the sol-gel reaction	35
2.5.3.2 Formation mechanism of MSN	37
2.5.3.3 Control of characteristics of MSN	40
2.5.4 Challenges of MSN as nanofillers (agglomeration, dissolution and uncertainty of separation mechanism)	41
2.5.5 Modification of MSN	42
3. Materials and methods	46
3.1 Materials	46
3.1.1 Materials for MSN	46
3.1.2 Materials for membranes	46
3.2 Preparation and characterization of MSN nanofillers	47
3.2.1 Preparation of MSN	47
3.2.2 Controlled functionalization of MSN	48
3.2.2.1 External pore surface functionalization (LMSN)	48
3.2.2.2 Internal and external pore surfaces functionalization (HMSN)	48
3.2.3 Dissolution of MSN	49
3.2.3.1 Determination of dissolved silica concentration:	49
3.2.4 Characterization of MSN	51
3.2.4.1 Hydrodynamic particle size analysis	51
3.2.4.2 Analysis of solid state structure	51
3.2.4.3 Nitrogen adsorption measurements	51
3.2.4.4 Determination of MSN density	51
3.2.4.5 Characterization of Nanofillers morphology	51
3.2.4.6 Surface chemistry of the nanofillers	51
3.2.4.7 Thermogravimetric analysis	52
3.3 Membrane preparation and characterization	53
3.3.1 Preparation of PES support membrane	53
3.3.2 Preparation of TFC and TFN membranes	53
3.3.3 Characterization of membranes	55

3.3.3.1 The membrane surface chemistry	55
3.3.3.2 The membrane surface charge	55
3.4 Evaluation of membrane performance	56
3.4.1 Evaluation of pure water and pure ethanol permeabilities	56
3.4.2 Evaluation of initial separation performance	57
3.4.3 Evaluation of long-term membrane stability	57
3.4.4 Evaluation of barrier layer durability of the pre-tested membranes	58
4. Results and discussion	59
4.1 Development of MSN nanofillers	59
4.1.1 Preparation of the base MSN	59
4.1.1.1 Control of MSN particle size	59
4.1.1.2 Surfactant removal	63
4.1.2 Surface functionalization of MSN	64
4.1.2.1 Controlled OTS-functionalization of MSN	64
4.1.2.2 Characterization of the functionalized NPs	65
4.2 TFN membrane preparation, characterization and initial performance evaluation	72
4.2.1 Characterization of TFN membranes	72
4.2.2 Influence of OTS functionalization on the initial membrane performance	75
4.2.3 Influence of MSN loading on membrane performance	78
4.3 Stability of MSN	85
4.3.1 Dissolution of MSN	85
4.3.2 Influence of the dissolution on the NPs structure	88
4.4 Stability of TFN membranes	94
4.4.1 Influence of MSN nanofillers dissolution on TFN membrane separation performance and barrier layer structure	94
4.5 Influence of silane molecule size used for MSN functionalization	99
4.5.1 Influence of MTS functionalization on MSN properties:	99
4.5.2 Influence of MTS functionalization on the TFN membrane performance	101
5. Conclusions	105
6. Outlook	108
7. References	109

Appendix A	I
List of Tables	I
List of Figures	II
List of Equations	V
Abbreviations	VI
Appendix B	IX
Curriculum vitae	IX

Chapter 1

1. Introduction

Water is a vital source for different aspects of human life. It represents 75% from body weight in infants and 55% in elderly [1]. Therefore, without water, humans can only survive for days. Due to the increasing population growth, industrialization, contamination and climate change, the stress on the shrinking resources of fresh water is increasing [2,3]. Because of these factors, among others, World Water Development Report (WWDR) 2018 reported that the global demand for water has been increasing at a rate of 1% per year [4]. Moreover, the report estimated that about 3.6 billion people (nearly the half of world population) live in regions that are potentially water-scarce at least one month per year. This number probably reaches 4.8-5.7 billion by 2050.

However, water covers about 71% of the earth surface, the vast majority of this water exists on oceans as salt water ($\approx 97,5$) and the remaining 2.5 % is fresh water, present in glaciers, ground water and other inaccessible forms. Only 0.014 % of the world's total fresh water is directly accessible for human use [5,6].

Consequently, insufficient availability of fresh water supply to meet the expanding need to water, is a serious challenge in many areas around the globe. The salinity content of seawater is usually in the range of 35000-45000 ppm and for brackish water is up to 10000 ppm [7], in the form of total dissolved solid (TDS). According to the World Health Organization (WHO), the salinity content in drinking water should not exceed 1000 ppm. Therefore, the high TDS value in both seawater and brackish water making them unsuitable for drinking and most domestic uses [8,9]. In this respect, the potential of desalination as a general strategy to minimize the TDS of the salt water down to the recommended level is more insistent [7].

To date, reverse osmosis (RO) is the leading technology for water desalination, and the installations of RO have been dominating about 80% of the current global desalination plants [10]. This is attributed to the lower energy consumption of RO compared to different techniques used for desalination [10–12]. The specific energy consumption (SEC) of RO and other techniques for desalination is summarized in **Table 1.1**. However, the consumed energy in RO is 3-6 KWh/m³, that is much higher than the minimum theoretical energy required for separating dissolved solids from water (equals 1.06 kW h/m³ for seawater at 35,000 ppm salt and at a typical 50% recovery) [7,9]. Consequently, there is still a need to further improve the efficiency of RO process. Apparently, a membrane with a high permeability allows water to easily pass through the membrane, which saves energy to pump the feed and reduce the overall cost of RO process, which is presented in **Figure 1.1** [10,13].

Table 1-1: Specific energy consumption (SEC) for desalinating raw water with concentration of 35,000 mg/L at 50% recovery and < 500 ppm product water quality by different desalination technologies [227]

Technology	Specific Energy Consumption (kWh/m ³)		
	Electrical energy	Thermal energy	Total equivalent electrical energy
BWRO	0.5–3	None	0.5–3
SWRO	3-6	None	3-6
ED	1–3.5	None	1–3.5
EDR	1-2	None	1-2
MVC	7-15	None	7-15
FO	0.2–0.5	20–150	10–68
MD	1.5–4	4-40	3–22
MSF	2.5-5	40-120	21–59
MED	2-2.5	30-120	15–57
MEB	2	60	30

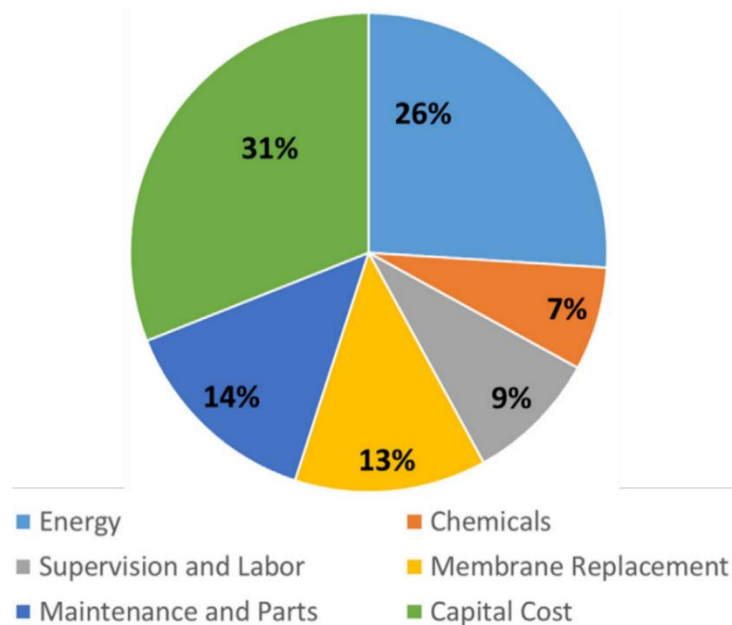


Figure 1.1: Typical Seawater RO plant cost composition [10]

Since 1980, the RO market is dominated by polyamide (PA) thin film composite (TFC) membranes. Although, TFC membranes have been received several improvements in the last few decades, the trade-off relationship between the membrane permeability and selectivity is still the most challenge facing any further development of these membranes [14]. One of the

most potential strategies to improve the TFC separation performance was introduced by Hoek and coworkers in 2007 by incorporation of porous nanoparticles into the matrix of PA barrier layer [15]. This new class of membranes was named Thin Film Nanocomposite (TFN) membranes. It was reported that introduction of NPs into the PA layer could enhance remarkably the separation performance and membrane stability, e.g., higher water permeability without sacrificing the membrane selectivity, increased anti-fouling properties, and in some cases increased chlorine resistance [16]. Mesoporous silica nanoparticles (MSN) are among the most frequently employed nanofillers for preparation of such PA TFN membranes, because their highly ordered structure which allows water to easily diffuse throughout the pore channels and due to their simple preparation and modification [17,18].

However, there are three main challenges facing the application of MSN-based TFN membranes in the large scale:

- ✚ During the membrane preparation, the hydrophilic properties of MSN, facilitate the undesired aggregation which hinders their integration into the PA layer, particularly when the MSN is dispersed in the organic phase during the interfacial polymerization (IP) reaction [19].
- ✚ MSN are susceptible to hydrolysis under alkaline conditions because their surface is covered with silanol (Si-OH) groups, which may result in undesired dissolution in water. Therefore, the intrinsic instability could critically impact the membrane performance [20,21].
- ✚ The mechanism of water permeability enhancement is not quite understandable and needs further and detailed investigations to show whether the MSN share the water transport through their internal mesopores or just by changing the structure/mesh size of the PA layer toward looser but highly selective barrier [17].

Accordingly, these issues may lead to a degradation in the membranes' barrier properties as well as loss of performance over time. Therefore, it had been motivated to search for new solutions to address these challenges, which was the ultimate objective of this thesis.

1.1 Aim of the work

Functionalization of MSN with hydrophobic silane-based organic substances, such as octadecyltrichlorosilane (OTS) or methyltrichlorosilane (MTS), can potentially mitigate the challenges of MSN-based TFN membranes and overcome the limitations of MSN as nanofillers. According to the state of the art, it is uncommon to use hydrophobic nanofillers to prepare TFN membranes, Nevertheless, the hydrophobic functionalization of MSN aims to achieve several goals. First of all, the MSN were synthesized by sol-gel approach and

functionalized via silanization reaction. The silane functionalization is controlled via modifying the external surface only of the as-synthesized MSN, then removing the surfactant template, which is still filling the internal pores, yielding MSN with hydrophobic external surface and hydrophilic pores (below referred to as “LMSN”). Alternatively, the silane functionalization was performed on both the internal pores surfaces and the external particles surfaces, by removing the surfactant before functionalization process. Therefore, the obtained MSN have concurrently hydrophobic external surface and hydrophobic internal pores. (below referred to as “HMSN”). An illustration for the controlled functionalization is presented in **Figure 1.2**.

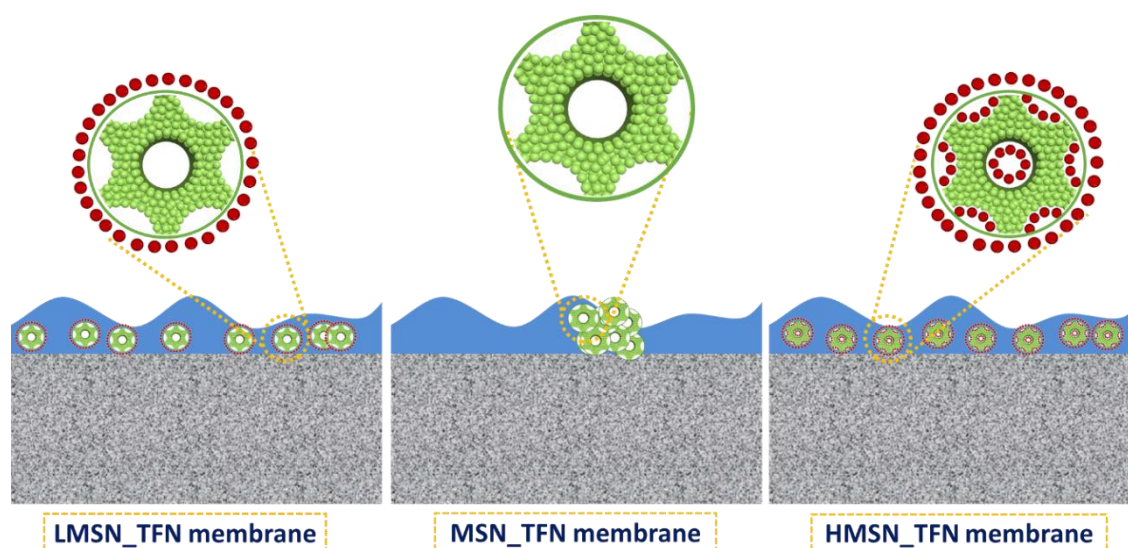


Figure 1.2: Scheme illustrating the incorporation of different MSN nanofillers inside the PA layer and the structure of functionalized MSN

Consequently, with this hydrophobic functionalization, the dispersion of MSN in the organic solvent can be improved during the preparation of membranes to achieve better distribution of NPs inside the PA film without aggregation that occurs in case of the hydrophilic NPs. Moreover, the hydrophobic layer formed on the surface and inside the internal mesopores of MSN is expected to increase the stability of NPs due to the improved anti-dissolution properties in the aqueous solution. This stability of the nanofillers may lead to increasing of the membrane stability.

In addition, with the variation of the porous structure through hydrophilic or hydrophobic mesopores, the role of MSN nanofillers in water transport can be simply investigated via comparing the water permeability in the two cases.

The method assumed to control the functionalization of MSN has been described in the literature for other applications; nevertheless, to the best of our knowledge, using the concept of LMSN and HMSN to investigate the role of nanofiller in the water transport and studying

the influence of MSN dissolution onto the stability of the corresponding TFN membranes has not yet been reported.

1.2 Objectives and structure of the thesis

This thesis is focused on development of new MSN-based TFN membranes with enhanced separation performance and membrane stability for water desalination via RO process. The objectives of this work and the work plan can be presented in the following:

1. Development of controlled functionalized MSN as nanofillers for TFN membranes

This objective can be achieved during the following:

- Preparation of MSN using the sol-gel method in presence of surfactant template and optimization the preparation conditions for control the particle size of MSN.
- Characterization of the prepared NPs and selection of the MSN sample with the optimum characteristics in terms of particle and pore sizes for functionalization process.
- Functionalization of the selected MSN sample using post grafting method in presence of silane compound (OTS).
- Adaptation of the functionalization in presence or absence of the surfactant to control the location of functional groups whether on the external surface of the NPs and/or inside the internal pores together.
- Full characterization of the functionalized MSN in terms of nitrogen adsorption, thermal gravimetric analyses, FTIR measurement and studying the morphology and porous structure.

2. Development of high-performance MSN-based TFN membranes containing the tailored MSN nanofillers.

This objective can be achieved during the following:

- Preparation of the PA TFC membrane and adaption of the IP conditions.
- Incorporation of unfunctionalized and functionalized MSN with different OTS concentration into the PA layer (TFN membranes).
- Characterization of both TFC and TFN membranes including investigation of membrane surface chemistry, charge, hydrophilicity, and morphology.
- Studying the influence of OTS concentration, in case of LMSN and HMSN, on the pure water and ethanol permeabilities and on the separation performance in aqueous NaCl (2000 ppm) solution using dead-end filtration set-up.
- Understanding the role of mesoporous structure on water transport through the membrane via comparing the permeance in case of LMSN (with the hydrophilic pore) and HMSN (with the hydrophobic pores).

- Investigation of the influence of nanofillers loading on the separation performance.

3. Studying the stability of Nanoparticles and membranes

This objective can be achieved during the following:

- Investigation of the influence of OTS functionalization on the stability of LMSN and HMSN, by measuring the dissolved silica concentration released from NPs dispersed in aqueous solution at pH 5 and pH 9.
- Investigation of the impact of nanofillers functionalization on the stability of TFN membranes by measuring the long-term separation performance in aqueous NaCl (2000 ppm) solution using cross flow filtration set-up at pH 5 and pH 9.
- Investigation of the durability of the barrier layer after the long-term separation performance and compared the results to the initial membrane performance.

4. Studying the influence of different size of silane molecules for MSN functionalization on the membrane performance.

This objective can be achieved during the following:

- Using smaller silane compounds such as methyltrichlorsilane (MTS) for functionalization of MSN instead of OTS and comparing the effect on the properties of both NPs and TFN membranes.

This thesis is divided into five chapters. **Chapter 1** (current) is an introduction demonstrating the motivation and main objectives of this thesis. **Chapter 2** provides the theory and literature review on the preparation of PA TFC and TFN RO membranes, challenges, and current trends for enhancing their separation performance. In addition, the chapter provides the development of mesoporous materials, such as MSN, and their preparation and functionalization to be adapted for several applications. **Chapter 3** demonstrates the methodology for preparation of TFC and TFN membranes, as well as synthesis and functionalization of NPs. In addition, the tools and instruments which have been used for the characterization. **Chapter 4** shows and discusses in detail the obtained results. Finally, general conclusions of this research and highlights some recommendations for future studies are provided in **Chapter 5**.

Chapter 2

2. Theory and Literature review

2.1 Membrane-based process for water treatment

The most current drinking water treatment plants use conventional treatment methods like coagulation–flocculation, sedimentation, sand filtration, disinfection and ozonation to produce fresh potable water [22]. However, these technologies are mainly designed to remove macro pollutants such as suspended solids, natural organic matter, dissolved iron and manganese, etc. [23]. This limitation of the conventional methods has driven various researchers to recommend alternative processes for water treatment.

Today, water treatment using membrane technology plays an increasingly important role in drinking and wastewater treatment, brackish and seawater desalination. The advantages of membrane filtration processes include simplicity, predictability, scalability, energy and contaminant removal efficiency and limited dependence on chemicals except for cleaning purposes [24,25].

Although the use of concentration-driven processes such as dialysis and pervaporation processes for industrial and environmental separations has increased in the past few decades, pressure-driven membrane processes remain the most widely used membrane technologies for water treatment applications [24,26]. Pressure-driven membranes are classified according to their characteristic pore size, applied pressure range or their application into microfiltration (MF), ultrafiltration (UF), nanofiltration (NF) and reverse osmosis (RO) (**Table 2.1**) [27,28]

Table 2-1: Pressure driven membranes characterizations [24]

Membrane type	Pore sizes (nm)	Pressure range	Species
MF	50-1000	0.1-2.0	Yeasts & fungi – Bacteria - Oil emulsions - Colloidal solids
UF	2-50	1.0-5.0	Viruses - Proteins/polysaccharides
NF	<2	5.0-20	Humic/nucleic acids - Antibiotics
RO	0.3–0.8	10-100	Inorganic ions (salts)

However, water treatment of the existing water resources is important, it can only improve the water quality not increase water supply. The only methods to increase water supply beyond what is available from the hydrological cycle are water reuse and desalination [11,29].

2.2 Water desalination technologies

Saline water represents about 97% of all water on the Earth [30]. Therefore, converting even a tiny fraction of this water to fresh water, could help effectively to overcome the current and

future water crisis. Desalination is the technology that converts saline water (seawater or brackish water) into fresh water by removing the salts. The salinity is expressed by the content of total dissolved solids (TDS) in water. Salinity level ranges for different feedwaters are shown in **Table 2.2**. According to the TDS value of the feed water quality, the desalination technology can be properly selected [31].

Table 2-2: Feedwater characterization by TDS content [32]

Water source	Minimum Salinity TDS (ppm)	Maximum Salinity TDS (ppm)
Seawater	15000	50000
Brackish Water	1500	15000
River Water	500	1500
Pure Water	0	500

The need for desalination continues to grow with the global cumulative capacity (contracted as of June 2017) reached about 100 million m³/d, compared to about 75 million m³/d in 2010 [32].

The two main types of desalination technologies are thermal, and membrane based. In thermal desalination, the seawater is heated until evaporation, and the vapor is condensed to produce fresh water. The most applicable technologies of thermal desalination are multi-stage flash (MSF), multiple-effect distillation (MED) and thermal vapor compression (TVC) [7]. On the other hand, the membrane desalination is based on separation of salt through a membrane rather than distillation. About 50% of the world's total desalination capacity lies in the Middle East[33]. Thermal desalination still represents the main desalination technology in this region because low cost of fossil fuel-based energy [31]. Nevertheless, in the last few years, water desalination based on RO technology has seen a significant increase [34].

2.3 Reverse Osmosis

Nowadays, reverse osmosis (RO) is considered the key technology for desalting water. As shown in **Figure 2.1**, in 2015, RO accounts for 65% of the global production capacity [2,35].

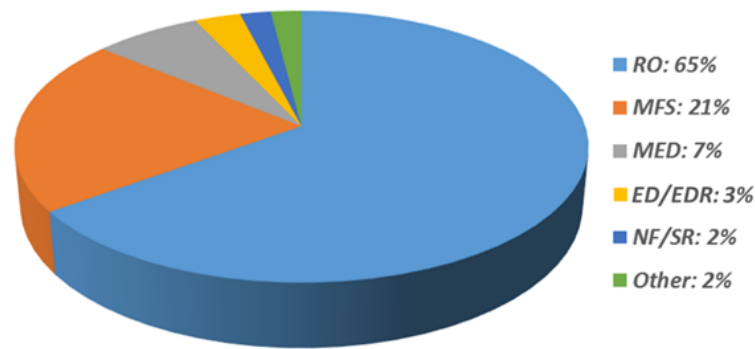


Figure 2.1: Total capacity installed by different desalination technologies. RO: Reverse Osmosis; MSF: Multi-stage flash; MED: Multi-effect distillation; ED/EDR: Electrodialysis/Electrodialysis Reversal; NF/SR: Nanofiltration/Sulfate Removal.

2.3.1 Principals and applications of RO

Osmosis is a natural phenomenon in which water is diffused from the solution with the low solute concentration to the solution with the high solute concentration through a semi-permeable membrane (**Figure 2.2**) [36]. The driving force for this phenomena is the osmotic pressure difference (the chemical potential difference) which causes water transport across the membrane until the equilibrium in solute concentration is reached [37].

RO is not a spontaneous process, in which a sufficient hydraulic pressure (ΔP) is applied to overcome the osmotic pressure difference causing water transport in opposite direction. i.e. from the solution with the high solute concentration to the solution with the low solute concentration [31] (cf. **Figure 2.2**).

The most common application of the RO is desalting water from seawater or brackish water. However, RO technology can be used for other applications such as production of ultrapure water [38], oil/water separation [39] and wastewater treatment [40].

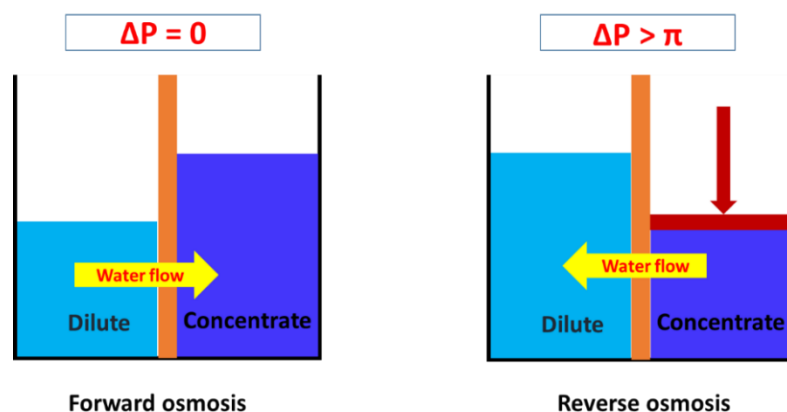


Figure 2.2: Schematic showing the water flow direction across the FO and RO membranes

2.3.2 Conventional polymeric RO membrane materials

In 1959, Reid and Breton reported the first RO hand-cast thin cellulose acetate (CA) membrane [41]. Despite this membrane exhibited 98% salt rejection, its very low permeate flux ($<10 \text{ mL}\cdot\text{m}^{-2}\cdot\text{h}^{-1}$) had prevented its commercialization [12]. Next, Loeb and Sourirajan developed asymmetric cellulose acetate (CA) membrane containing a dense layer of 200 nm on top of a thick porous structure (50-150 μm) in one-step casting [42] and this was the first successful trial that made RO possible in application. Then, cellulose triacetate RO membrane was developed because of its higher thermal and pH stability than cellulose diacetate membranes. Despite of the susceptibility of the acetate group to hydrolysis in both acidic and basic conditions, as well as sensitivity to microbial contamination, that limited its application [43], CA remained the best membrane material for RO until 1969.

The first non-cellulosic RO membrane was developed by Richter and Hoehn, and was comprising an aromatic PA hollow-fiber membrane [44]. This membrane was consequently commercialized and utilized in desalination of brackish water application. Despite the commercial success of this membrane, the high susceptibility to attack by disinfectants such as chlorine was observed after prolonged use. Subsequently, more chlorine-resistant asymmetric RO membranes based on polypiperazine-amides were developed [45] but their rejection was below the acceptable level required for commercialization [12].

2.3.3 Thin film composite (TFC) membranes

One of the most important drawbacks of CA asymmetric RO membrane prepared during one-step casting is the densification (compaction) of membrane under pressure, which causes gradual lowering of membrane flux [46,47]. This led to developing the concept of thin-film composite (TFC) membranes, in which the skin and supportive layers of the membrane are fabricated from different materials. One of the most common materials which used as a support is polysulfone (PSf), as it has good resistance to compaction, potential flux and good chemical and mechanical stability [48].

Using of PSf as a support was successfully introduced by Cadotte during fabrication of the first comparable non-cellulosic RO membrane via the IP reaction of polythylenimine and toluene di-isocyanate. The resulted membrane named NS-100, which considered a major technological milestone in the history of RO processes [49].

However, NS-100 membranes demonstrated superior rejection of organic compounds, and good stability in high temperature, acidic and alkaline environments, but they have no resistance to chlorine, and have low mechanical stability. Subsequently, Cadotte found that high selective

and water permeable RO membranes can be produced using the IP reaction between aromatic amines and aromatic acyl halides containing at least three carbonyl halide groups [50]. The best example was FT-30 RO membrane that was prepared by IP reaction between 1,3-benzenediamine (m-phenylene diamine, MPD) with 1,3,5-benzenetricarbonyl trichloride (trimesoyl chloride, TMC) [51].

2.3.4 Fabrication and structure of polyamide (PA) TFC RO membranes

The typical TFC PA RO membrane is composed of three different layers (**Figure 2.3**) including:

- A thin layer of aromatic PA (100- 200 nm). This layer is the selective layer of the membrane so it should be dense enough to retain the salt ions. The pore size of PA layer is created from the interstitial voids between the polymer chain to be ≤ 0.5 nm [52].
- A thick layer of PSf or polyethersulfone (PES) with a thickness of 20-50 μm . This layer works as a support to provide the membrane with the required mechanical stability.
- Another thick layer of nonwoven such as polyester (> 100 μm) acts as a backing layer that provides additional mechanical strength [53].

This multi-layer structure of TFC RO membranes enables the manufacturers to optimize each layer independently, in order to combine high water permeability and high salt rejection [54].

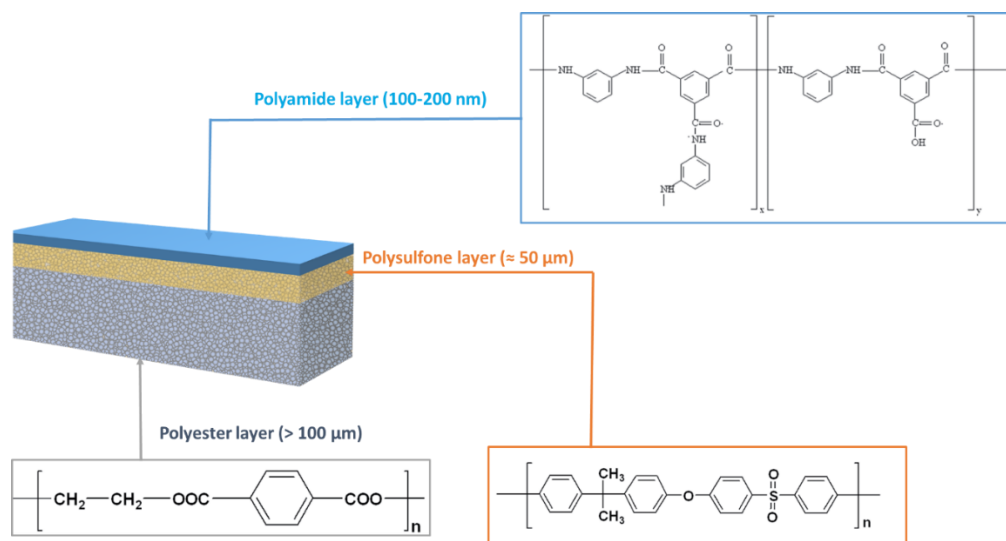


Figure 2.3: Schematic of the TFC membrane structure and its composition

IP is still the most popular method for preparation of TFC PA RO membrane, since the first appearance of FT-30 membrane by Cadotte until now. In the IP method, two completely immiscible solvents containing the two monomers are contacted together over a support membrane and the reaction occurs at the interface located over the membrane surface [55].

MPD and TMC are still the most common examples of diamine and trihalide acid monomers, respectively.

For preparation of membrane, firstly, the support membrane is immersed in an aqueous solution of MPD for a certain time then the excess of monomers is removed. Thereafter, an organic solvent containing TMC is allowed to contact with the support to start the IP reaction [56]. Because MPD has partial miscibility in the organic solvent (such as n-hexane), it diffuses into the organic phase to react with TMC and form the polyamide film. This asymmetric solubility of the two monomers in the two solvents allows the reaction to be diffusion controlled reaction [57].

The formation of PA was described to include three stages [58]:

- Formation of a loose polymer: at the initial stage, a loose polymer film is formed due to the first interaction between the MPD which diffused to the interface and TMC.
- Formation of dense polymer: with increasing number of diffused MPD molecules to the interface a dense polymer is formed.
- Reaction inhibition: the formed dense layer of PA hinders the further diffusion of MPD and the reaction is limited.

The kinetics studies of IP have shown that the initial formation of PA layer occurs rapidly, about 50% of the total thickness is achieved in 2 seconds [59], followed by a slowing down. Accordingly, the IP reaction is a self-limiting or a self-inhibiting reaction, which means that the polymer film inhibits its own growth even with extended time [60,61]. However it has been recently reported that the self-inhibiting regime is not severely occurred, and the formed layer can be continued to grow, even though in slow rate, to maximize the thickness. Therefore, the IP reaction is mostly limited by a continuous rapid supply of monomers particularly the MPD [62].

2.3.5 Membrane transport theories

RO membranes are assumed to be dense or nonporous. Although this assumption is unclear because the pores must be present otherwise no transport will occur, however it is used just to explain that the pores of RO membranes are very small. Kim et al. [63] characterized the pore size of crosslinked PA formed by MPD/TMC via positron annihilation lifetime spectroscopy (PALS). They found that there are two kinds of pores; network pores with diameter of 0.42-0.48 nm and aggregate pores with diameter of 0.7-0.9 nm as presented in **Figure 2.4**.

Because this confusion of the term porous or nonporous, two different models were assumed to describe the water-salt separation by PA TFC membrane; pore-flow model (PFM) and

solution-diffusion model (SDM). The former considers the PA layer is porous. Water and solute move through the pores by diffusion and convection [64,65]. The SDM is more popular for describing the RO membrane performance because of its simplicity and wide applicability.

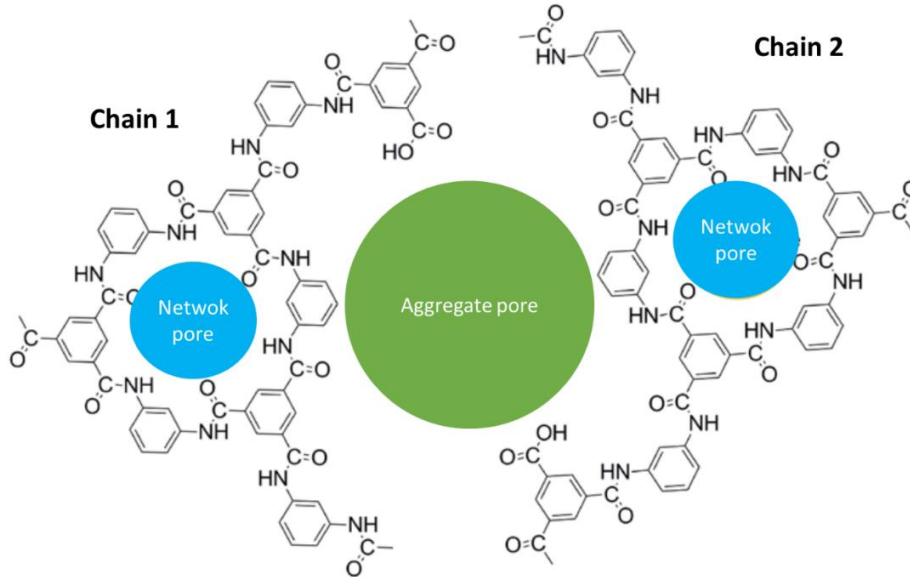


Figure 2.4: Schematic illustration of possible molecular structure of network and aggregate pores in aromatic PA TFC membranes synthesized by reaction of MPD and TMC [64]

2.3.5.1 Solution-diffusion model (SDM)

In SDM, the permeant dissolves in the membrane material and then diffuses through the membrane because of the concentration gradient across the membrane. Transport of water or salt across a RO membrane generally includes three steps: i) absorption of water from the feed into the membrane, ii) diffusion through the membrane thickness and iii) desorption of water from the membrane surface to the permeate [34]. This diffusion is best described by Fick's law of diffusion (**Equation 2.1**)

$$J_i = -D_i \frac{dc_i}{dx_i}$$

Equation 2.1: Fick's law of diffusion

where, J_i is the flux of the component i (water or solute) through the membrane, D_i is the diffusion coefficient of the constituent in the membrane and $\frac{dc_i}{dx}$ is the concentration gradient across the membrane. In order to occur water transport through the RO membrane, the applied hydrostatic pressure must be greater than the osmotic pressure of the solution (cf. **Figure 2.2**). This pressure difference creates a chemical potential, which is represented as a concentration gradient, across the membrane that drives water flow through the membrane from the feed side

into the permeate side against the natural direction of osmosis, while the salts are retained and concentrated on the feed side. Some salt passage through the membrane does occur as well; salt passage for the same membrane increases with the salt concentration. By rearranging Fick's law, equations for water flux J_w and salt flux J_s in RO can be obtained as presented in **Equations 2.2 and 2.3** [66–68].

$$J_w = A (\Delta P - \Delta\pi)$$

Equation 2.2: Water flux in RO membrane according to solution-diffusion model

$$J_s = B (C_{feed,S} - C_{permeate,S})$$

Equation 2.3: Salt flux in RO membrane according to solution-diffusion model

where A is the water permeability coefficient, B is the salt permeability coefficient, ΔP and $\Delta\pi$ are the transmembrane pressure and osmotic pressure difference between the feed solution and the permeate solution, respectively, and $C_{feed,S}$ and $C_{permeate,S}$ are the salt concentrations at the membrane surface on the feed solution side and the permeate solution side, respectively. The osmotic pressure depends on the salt concentration and the solution temperature and can be estimated by van't Hoff equation (**Equation 2.4**):

$$\pi = CRT$$

Equation 2.4: Van't Hoff equation

Where C is the molar concentration of ions, R is the ideal gas constant, and T is the operating temperature.

The salt rejection is practically measured to describe the ability of the membrane to separate solute (salt) from water (i.e. the membrane selectivity). It is defined according to **Equation 2.5**.

$$\text{Salt rejection} = \left(1 - \frac{C_p}{C_f}\right) \times 100\%$$

Equation 2.5: Calculation of salt rejection

where C_p and C_f are the salt concentrations in the permeate and feed solutions, respectively.

2.3.5.2 Factors contribute to transport

2.3.5.2.1 Salt properties and membrane surface charge

Most of PA TFC membranes surfaces are found to exhibit a negative charge due to presence of carboxylic groups which resulted from the hydrolysis of unreacted acid chloride [12,68]. When a typical feed solution containing cations (positively charged ions) and anions (negatively charged ions) are contacting with the negative charge membrane surface, the anions are found

to be more rejected than the cations due to the repulsion force among the similar charges. Consequently, the concentration of anions on the membrane surface is lower than that of the bulk, and at the same time, the concentration of cations in the membrane surface is greater than their concentration in the bulk.. This ion shift creates an electrical potential known as Donnan potential or Donnan effect [68,69]. The role of Donnan effect on the membrane separation represented in attracting the cations to the membrane while repelling the anions away. Because the salt rejection is strongly dependent on the rejection of anions [69], therefore, the higher Donnan potential, the higher overall salt rejection [70].

Both the feed salinity (feed concentration) and the feed composition (valence of salt ions) have a strong influence on Donnan potential. The Donnan potential is found to decrease as the feed salinity or concentration of the divalent ions in the feed solution increases. This is mainly because divalent cations can shield the membrane surface charge and decrease the repulsive force causing Donnan potential and increase the salt passage [66,69] as presented in **Figure 2.5**.

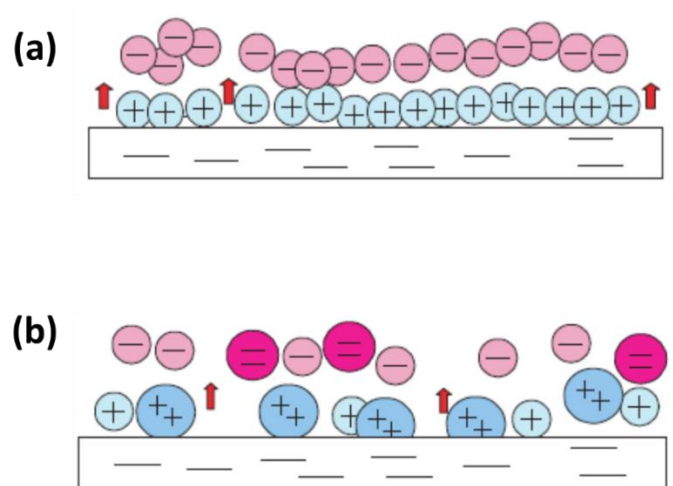


Figure 2.5: Schematic diagram illustrating the shielding of Donnan potential due to a) high feed salinity and b) divalent cations. The figure adapted from [71]

The increase of salt passage in case of high feed salinity can be caused by the increase in a gradient concentration between the feed and permeate which is the driving force of the salt separation according to SDM. The high feed salinity not only decreases the salt rejection but also decreases the water flux. This can be explained by increase the osmotic pressure which reduces the net driving force for water transport at a given operating pressure [69,71].

Moreover, the hydrated diameter of the ions may also affect the transport separation. As the size of cations radii increases, the diffusivity decreases because the bigger particle size, the more friction force during the diffusion inside the membrane matrix. As a result the

permeability decreases [66]. However, this friction force is found to be overcome by the strong interaction with membrane in case of divalent ions which resulted in slightly higher diffusivity [72,73].

2.3.5.2.2 *Operating conditions*

The separation performance of RO membranes is also influenced by the operating conditions such as the applied pressure, operating temperature and pH [34,71,74].

As assumed from SDM, the water flux is equal to zero when the applied pressure is the same as the osmotic pressure. By increase the applied pressure, the water flux increases and tends to decrease at the very high pressure due to the membrane compaction [66]. Whereas the salt rejection is found to increase quickly by increase the pressure until reaches a maximum value then becomes nearly constant [71].

The operating temperature is also considered an important parameter which should be taken into account for RO processes. It is observed that increase of operating temperature leads to increasing both water and salt transport across the RO, due to increasing the diffusion coefficient [34,75]. On the other hand, effect of operating pH might not be notably presented in SDM, nevertheless it affects the membrane performance. pH of the feed solution can alter the membrane surface charge. It is reported that most of PA TFC membranes carry negative charges at the normal operating pH (i.e. pH 6-7) because their isoelectric point (ISP) is at pH 3-4 [74,76]. As a result, the increase of pH can boost the negative charge on the membrane surface which improves the salt rejection.

2.3.5.2.3 *Membrane structure*

Because the manufacturing of RO membranes is based on polymer materials, the transport behavior will be strongly influenced by polymer properties such as presence of free volume, thickness and cross linking of the polymer. The free volume in PA matrix is the unoccupied spaces which exists among the polymer chains and form the pores of the PA barrier layer (cf **Figure 2.4**). These spaces are known as the free volume holes and it is thought to play an important role on water and solute transport [77,78].

The total thickness of the PA barrier layer is 200-300 nm as reported by many studies [79–81]. However, the morphology of this skin layer is not homogeneous [82], the back surface of this layer was found to be highly porous [80] as presented in **Figure 2.6 (a)**, whereas the top surface is dense. Therefore, the effective thickness of the PA layer is the thickness of the dense layer itself, which is in range of 20-30 nm [83]. In contrary, the top surface of the skin layer is

usually described as ridge and valley structure [12,14,84] (cf. **Figure 2.6 (b)**) and a hollow interior of crumpled nodules (also called protuberances) [80,85].

Several studies suggested that these protuberances and ridges have interconnecting cavities and tunnels through which the dense layer and the pores on the back surface are connected (**Figure 2.6 (c,d)**) which improves the transport of water during the RO filtration [78,80,85].

Furthermore, the crosslinking of the PA layer also affects the separation performance of the membranes. Due to the polar and relative hydrophilic nature of the PA, it can swell in water. This swelling increases the polymer chain mobility and consequently increasing water and salt fluxes. Therefore, the crosslinking between the polymer chains is highly desired and can be achieved usually by heat curing to control the degree of swelling and achieve high separation performance [66,81].

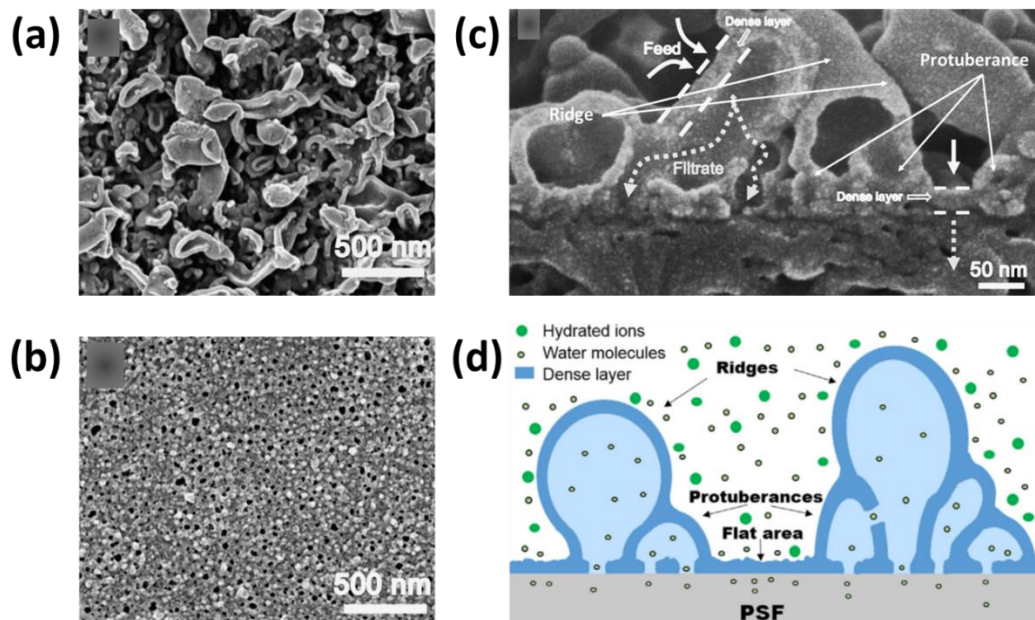


Figure 2.6: (a) SEM of the top PA surface, (b) the back side of the PA layer, (c) high magnification SEM image of the top PA surface and (d) schematic illustration for cross-sectional morphology of PA film [80]

2.3.5.2.4 Concentration polarization

While water molecules can transport through the PA films, most of salts are usually retained under the applied pressure. The retained salts accumulate at the membrane surface creating a concentration gradient between the higher salt concentration, close to the membrane surface, and the lower bulk concentration. This phenomenon is known as concentration polarization [34,86]. Concentration polarization has a strong impact on both water flux and salt rejection in RO processes. The feed solution is transported to the membrane surface by convection and the retained salts form a thin stationary boundary layer. This layer causes an increase in the osmotic

pressure. As a result, a pressure drop occurs producing a decline in water flux accompanied with an increase in salt transport through the membrane [34].

2.3.6 Challenges of TFC membranes

Despite the PA TFC membranes dominating the RO market, these membranes are suffering from three downsides which limiting their wide applications and long-term performance.

2.3.6.1 Trade-off relationship between permeance and salt rejection

The trade-off means that the relationship between the membrane permeability and selectivity is often inversely correlated [37], i.e. the material which are more permeable to water will naturally tend to have less ability to separate solutes from water and vice versa [41]. Therefore, to evaluate the strategies which aimed to improve the water permeance of RO membranes, the salt rejection should be retained. The potential strategy is the one which increases the permeability without sacrificing the selectivity.

2.3.6.2 Fouling

Fouling, particularly, scaling and biofouling, is a major limitation in membrane separation process. The fouling of TFC RO is believed to be related to the insufficient hydrophilicity, charge and high roughness of PA layer [88]. Membrane fouling can induce the concentration polarization and increase the pressure drop. The fouling layer resistance can cause decline in both water flux and salt rejection as well as reduce both permeate recovery and permeate quality [31]. This increases the operational cost due to the increased energy demand and the required chemical cleaning to resume the original flow rate [14,89].

2.3.6.3 Chlorination

Chlorine is widely used in water treatment or water desalination plants as a disinfectant for biofouling control [90,91]. PA TFC membranes are strongly susceptible to chlorine attack. The sharp deterioration of membrane performance occurs when exposed to even a few ppm of chlorine because it attacks the nitrogen-hydrogen bonds in the amide bond, that hold polyamide polymers together. This leads to degradation of the PA layer and opening holes which allow salts to pass through the membranes [3,54].

2.3.7 Strategies to improve membrane performance and antifouling properties

Due to the above limitation of PA TFC membranes, it was crucial to point out the most important reported strategies to improve the performance of this kind of membranes. These strategies include:

2.3.7.1 Optimization the preparation conditions

2.3.7.1.1 Effect of monomer type and concentration

The choice of monomers used in preparation of PA TFC membrane is necessary in order to tailor desired membrane structure and separation performance. In literature, the two diamine monomers which have been frequently used for preparation of PA TFC membrane are MPD or piperazine (PIP), along with TMC as acyl halide monomer [24]. The produced MPD- and PIP-based TFC membranes were found to exhibit completely different surface characteristics and separation performance due to the difference in the reactivity of the two diamine monomers [57,92].

However, several attempts have been conducted to employ new monomers which are usually containing more polar functional groups in order to produce surface with low roughness and high hydrophilicity to mitigate fouling and/or increase chlorine resistance [93]. For example, in a recent work [94], a novel semi-aromatic PA RO membrane was fabricated using a dendritic molecule of trimesoylamidoamine as a functional amine monomer to react with TMC through the IP technique. The produced PA membrane exhibited improved water permeability, antifouling and chlorine tolerant properties due to the dendritic structure which provided the membranes with more hydrophilic groups and smoother surface compared to the pristine MPD-TMC membrane [94]. Moreover, the monomer concentration plays an important role on membrane separation performance. Korshidi et al. [95] found out a direct relation between increasing the TMC concentration and formation of more permeable and lower salt rejection membrane and opposite properties achieved by increasing the MPD concentration.

2.3.7.1.2 Organic solvent selection

The rate and extent of IP reaction is strongly influenced by the diffusivity and solubility of the diamine (usually MPD) in the organic solvent [84]. Park et al. [56] reported that the high diffusion rate of MPD into the organic solvent showed dense and thinner layer of PA and consequently better PA TFC performance. Gosh et al. [81] found that the low viscosity and high surface tension of the organic solvent achieved high membrane performance.

2.3.7.1.3 Curing temperature and reaction time

Curing temperature and IP reaction time can also affect the characterization and performance of the synthesized PA TFC membrane [81]. Heat curing is aimed to accelerate the evaporation of the residual aqueous and organic phases to help termination of IP reaction [96]. The curing temperature is varied in the literature from room temperature to higher than the boiling point of both organic solvent and water [95,97]. The variation of curing temperature affects the surface morphology and consequently affects the separation performance. For example, it was reported that the curing at room temperature produced PA membrane with high salt rejection and low

permeance [95]. When the temperature increased to 55 °C, the water permeance increased with slight decrease in the salt rejection. This is most likely due to altering the surface morphology, and with further increase in temperature to exceed the boiling point of the organic solvent, the salt rejection improved with slight decrease in water permeance. This was attributed to the fast evaporation of the residual solvent and formation of a dense and cross-linked PA layer.

On the other hand, the prolonged time of the interfacial reaction time maximizes the film thickness which resists the water flow and improves the salt rejection [98]. Nevertheless, it was found in another study that increasing the reaction time has a negligible effect on both water flux and salt rejection. This is because the permeation is mainly controlled by the dense part of PA layer which was rapidly formed at the surface [95].

2.3.7.1.4 Additives

Presence of additives beside the monomers in aqueous and/or organic phases was found to have a remarkable influence on the membrane structure. The role of the additives has been reported to include controlling the aqueous and organic phases miscibility, monomer diffusivity, polymer crosslinking and control the rate of IP reaction by scavenging the formed byproduct or quenching the residual acyl-chloride group [57,63,81,87,99,100]. **Table 2.3** presents the influence of various additives on the membrane performance.

Table 2-3: Additives and their influence on PA TFC membrane performance

Additives	Example	Influence	Reference
Acid scavenger	Triethyl amine (TEA), NaOH, triphenyl phosphate	Increase permeability without observable rejection decline	[81,100]
Phase miscibility enhancer	Isopropyl alcohol (IPA), acetone, Dimethylsulfoxide (DMSO), Hexamethyl phosphoramide (HMPA),	Increase roughness, increase water flux	[63,87]
Amine absorption enhancer	Camphor sulfonic acid (CSA)	Increases water permeability	[81,100]
Crosslinking inhibitor	<i>N,N</i> -Dimethylformamide (DMF)	Increases permeability Increase the negative charge	[81]
Acyl-chloride quenching	Ammonium hydroxide	High permeability without decrease rejection	[99]

2.3.7.2 Optimization the support membrane

One of the major advantages of the TFC structure of PA membrane is the multilayer structure, which allows to modify each layer individually. It is always believed that the support

layer in the TFC structure is only required to provide the membrane with the required mechanical strength. However, it was found by several studies that the characteristic of the support are in a close relation to the membrane performance [57,84,87,101].

The hydrophilicity and pore size of the support (usually PSf or PES) have more practical implications for the IP reaction [101]. Gosh and Hoek found that more permeable, hydrophilic support produced smooth and low permeable PA layer, because large thickness of PA can be formed within the wetted pores. Contrarily, rough and more permeable PA layer was produced when using hydrophobic support [84]. The support pore size has a similar influence on wetting as the hydrophobicity. Pore size in range of 1 – 100 nm were revealed to offer stable interface for the IP reaction. Whereas, the sublayers of lower pore sizes are difficult to be pre-wetted, and the large pore sizes in μm range are suffering from liquid evaporation [84].

2.3.7.3 Surface modification

Surface modification had been also employed as a potential method to improve the performance of the PA TFC membranes and provide them with enhanced antifouling properties and chlorine resistance. It has been confirmed that the PA surface contains many negative charges of the carboxyl group due to the incomplete crosslinking of the polymer. The presence of these negative charges facilitates the binding of different surface coatings [102].

2.3.7.3.1 PEG-based hydrophilic coating

PEG is commonly employed as coating layer of PA membranes due to its high hydrophilicity, neutral charged nature and its ability to form hydrogen bond with water. The increase in the surface hydrophilicity reduces the interaction with foulants [14,103]. The fouling resistance of the coated surface increases with increasing the length of PEG chain [104]. However the superior antifouling properties of PEG, it has a disadvantage regarding its high degradation in presence of oxygen and transition metals [103,104].

2.3.7.3.2 Protein coating

Coating the membrane surface with a natural polymer such as sericin protein, is also reported by Yu et al. [105]. They coated the surface of commercial PA TFC membrane with sericin through dip coating followed by in situ crosslinking with glutaraldehyde. The obtained membrane showed lower water permeability due to additional hydraulic resistance, but both salt rejection and antifouling properties improved due to increasing the surface negative charge and hydrophilicity, in addition to the smoother surface morphology [105].

2.3.7.3.3 Zwitterionic based coating

Surface coating of PA TFC membrane with zwitterionic polymers have drawn a great attention for fabrication a membrane with superior antifouling properties. Zwitterionic compounds comprise both negative and positive charged units. This structure can create more stable and stronger bonds with water than the other neutral hydrophilic materials such as PEG [106]. Therefore the zwitterionic-based membrane surface which containing a sufficient density of the positive and negative units can remarkably improve the non-selective fouling resistance [107]. zwitterionic polymers can be coated over the PA membrane surface using several techniques such as surface-initiated atom transfer radical polymerization [108], redox-initiated graft polymerization [109] and chemically-initiated vapor deposition [110].

However, these techniques revealed some drawbacks such as reduction of water permeance due to the addition resistance of the coated layer and higher fabrication cost because the addition of post-modification step [96]. Recently, Duong et al. [107] have developed a novel PA TFC membrane by tethering modified zwitterionic copolymer via in situ IP, the fabricated membrane exhibited a tremendous increment in water permeance with comparable dye rejection and excellent antifouling properties.

2.3.7.3.4 Chlorine resistance coating

The strategy of fabrication of PA TFC membrane with a good chlorine resistance properties is based on deposition of a sacrificial layer which prevents PA layer from direct contact with chlorine, therefore it protects the membrane [14]. However, likewise, this additional layer could reduce the water flux. The same conclusion was reported by Ni et al. [54] who found a trade off between the membrane flux and the coating effects improving chlorine and fouling resistances of membranes.

2.3.7.4 Aquaporin based PA RO membranes

These membranes are also known as biomimetic membranes. Aquaporins (AQPs) are the biological water channels known for fast water transport with complete retention of ions and other solutes. The water transport rate for the single channel reaches $\sim 10^9$ water molecule per second [111]. Accordingly, these impressive characteristics of AQPs have attracted great attention in water desalination applications. The first successful attempt for fabrication of AQPs-based TFC RO membrane has been done by Zhao et al. [112] The resulted membrane exhibited 25% increase in water flux without compromising the NaCl rejection. Later, Li et al. [113] succeeded to fabricate AQPs-based hollow fiber membranes by embedding proteoliposome into the polyamide layer in the cavity of a hollow fiber substrate via IP reaction as presented in **Figure 2.7**. The resulted membrane exhibited water permeability reached ~ 8

$L/m^2.h.bar$ which was about twice the commercial BWRO or the AQPs- based flat sheet membranes.

Despite the superior separation performance of AQPs-based PA membranes, the membrane long-term stability, scalability and production cost shall be taken into consideration.

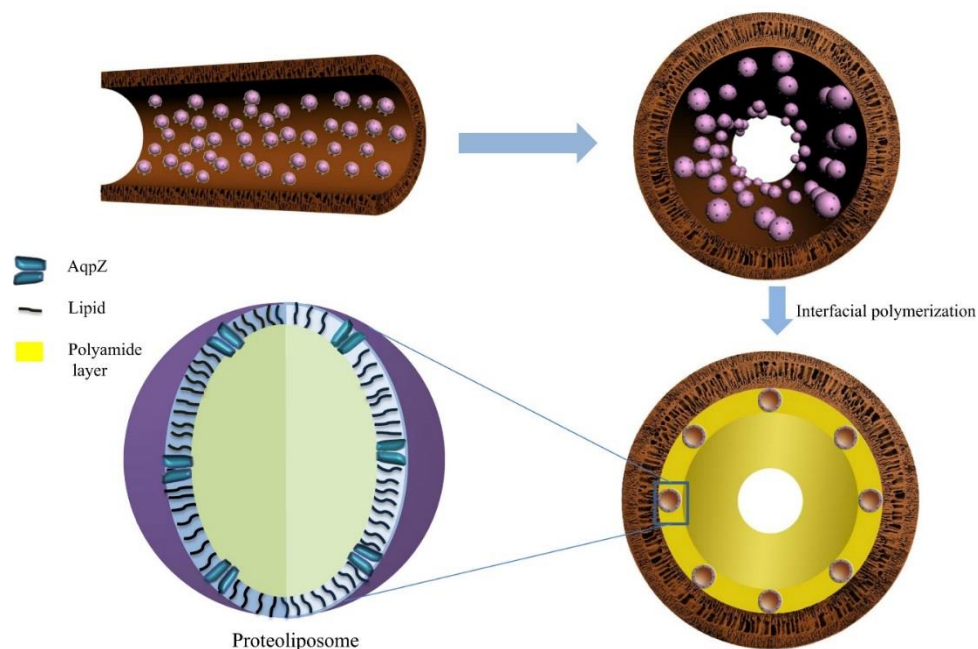


Figure 2.7: Schematic of preparation of AQP-based hollow fiber membrane [113]

2.4 Thin film nanocomposite (TFN) membranes

2.4.1 Overview of TFN membranes

In 2007, Hoek and coworkers [15] introduced for the first time the concept of TFN membranes by incorporation of nanosized fillers in the PA skin layer of the TFC membranes (**Figure 2.8**). Nevertheless, the nanofillers can be also incorporated in the support layer of TFC membranes [114]. The TFN membranes are similar to other classes of composite membranes known as mixed matrix membranes (MMMs) which is fabricated by one step phase inversion technique. However the TFN membranes have an advantage from MMMs of optimizing the skin and support layer of the membrane individually, which allows a more versatile membrane to be modified [115]. Addition of NPs provides more degrees of freedom to the properties and separation performance of TFC membranes to overcome their limitations [15].

As a result, TFN membranes have gained increasing attention on many applications such as RO, NF, FO, gas separation and organic solvent nanofiltration (OSN) [9,16,23,116].

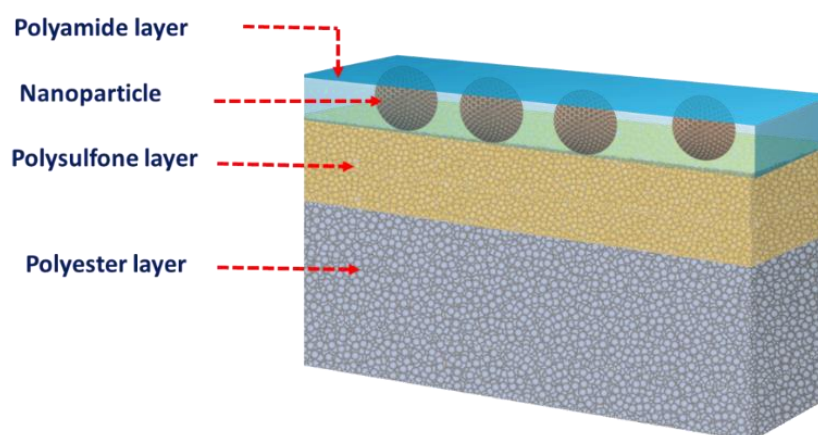


Figure 2.8: Scheme illustrating the structure of TFN membranes

Despite the fact that the feasibility of TFN membranes have been demonstrated at the lab-scale, there is only one commercial TFN membrane known in the RO market which was launched in 2011 by NanoH₂O (now LG Chem). It included nano-zeolites additives and exhibited two folds higher water flux than the standard commercial TFC membrane with NaCl rejection maintained at > 99.7% [16,27]. To date, there are several kinds of NPs that have been used as nanofillers for TFN membranes. Most of these NPs are porous nanofillers (**Table 2.4**) and some of them are nonporous such as Ag [117], TiO₂ [118] and SiO₂ [119].

Table 2-4: Overview of filler materials in TFN membranes and comparison of their performance with control TFC membranes; ↑, ↓ and ↔ indicate an increase, decrease, and remain same, respectively. All membranes were tested in NaCl (2000 ppm) except [131] in brackish water

Filler properties			Filler Loading	Dispersion phase	Permeability (L/m ² h.bar)	Rejection (%)	Compared to their TFC control membrane	
Type	Particle size (nm)	Pore size (nm)					Permeability	Rejection
Zeolite								
NaA [120]	100	0.42	0.3 wt%	Organic	1.9	97.9	44% ↑	0.5% ↑
NaY [121]	150	0.74	0.15 wt%	Organic	4.8	98.8	84% ↑	0.4% ↑
MOF								
ZIF-8 [122]	150	0.34	0.005 wt%	Organic	2.7	85	185% ↑	↔
MIL-101 (Cr) [97]	200	1.2	0.05 wt%	Aqueous	3.2	99	44% ↑	↔
MSN								
MCM-41 [123]	100	3	0.015 w/v	Organic	3	94.6	36.5 ↑	↔
MCM-48 [18]	125	2.3	0.014 w/v	Organic	2.5	95	67 % ↑	2% ↓
Graphene								
GO [124]	n/a	0.88	100 ppm	Aqueous	2	97.5	39% ↑	1% ↓
N-GOQD [125]	10	n/a	0.02 w/v	Aqueous	1.6	93	168% ↑	↔
CNTs								
CNTs [126]	n/a	3-4	0.37 wt%	Aqueous	3.3	98.5	32% ↑	↔

2.4.2 TFN membranes fabrication

Like PA TFC membranes, TFN membranes also are fabricated mainly via IP process. The addition of nanofillers inside the PA skin layer includes their dispersion with the organic phase [15,17,127] as well as with the aqueous phase [97,121,124] (cf. **Table 2.4**). It is generally known that most inorganic NPs are hydrophilic. Therefore, they can be better dispersed in the aqueous phase than in the organic phase. However, removing the excess aqueous solution during the IP process, most of NPs can be detached with the amine solution, which affects the obtained TFN membrane performance [16].

The fillers can also be deposited on the surface of PA TFC membrane by dip coating in the NPs solution as reported by [128], but the stability of this kind of membranes in RO application which needs a high operated pressure may be not guaranteed. On the other hand, addition of NPs to the organic solvent, allows them to be agglomerated inside the PA layer. As a result, nonselective voids are created among the NPs and the polymer matrix which declines the membrane performance [129]. Nevertheless, addition of nanofiller to the organic solvent was adopted in the literature.

In order to improve the compatibility of the hydrophilic NPs with the organic solvent, surface modification with a hydrophobic substance was reported [130–133]. For instance, Dong et al. [130] have fabricated PA TFN membranes containing surface modified NaA zeolite NPs with OTS. They found out that the dispersion of modified zeolite improved in the organic solvent during IP process. As a result, the integration of nanoparticles (NPs) inside the PA layer improved which led to enhanced water flux and salt rejection.

Despite the addition of nanofillers to the organic phase is more effective than their addition to the aqueous phase in terms of more trapping inside the formed PA film, losing some NPs during the membrane preparation and their random distribution inside the PA cannot be completely avoided. To solve this problem, Kong et al. [52] reported for the first time the “pre-seeding” approach for preparation TFN membranes (**Figure 2.9**). In this approach, instead of directly immersing the MPD-coating PSf support membrane into the TMC-hexane solution containing the nanofillers (Zeolite), the MPD-PSf membrane is firstly contacted with a certain amount of hexane solution containing zeolite, low concentration of TMC and ethanol to form the pre-seeded zeolite on the membrane surface. Then, the hexane solution of high TMC concentration is contacted with the membrane to complete the IP reaction. By this strategy, the nanofillers can disperse into the PA film very well without formation of the undesired voids [52].

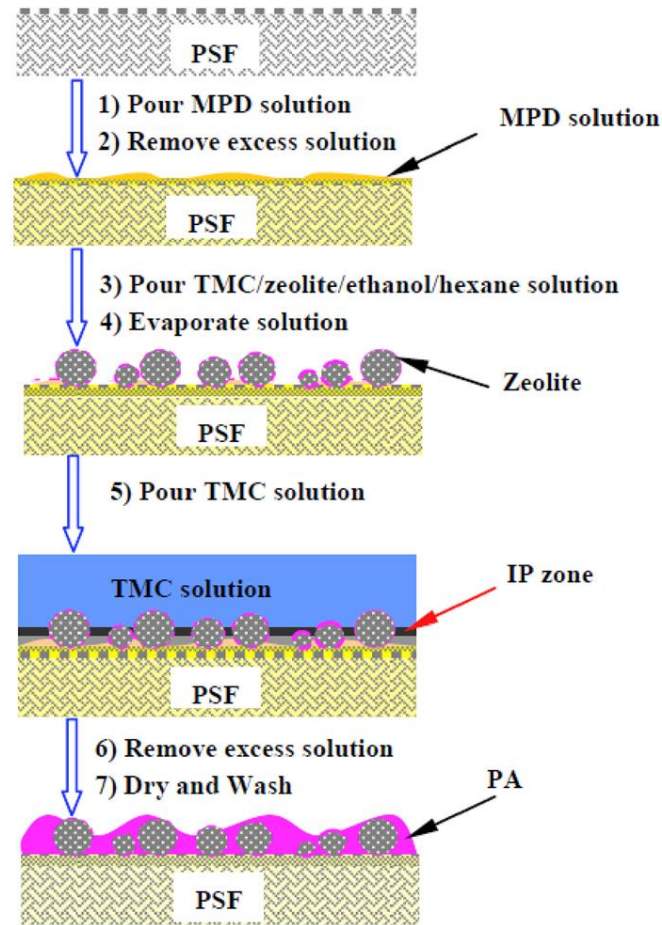


Figure 2.9: Schematic representation of preparation of TFN membranes by pre-seeding approach from [16]

Similar and more simple approach was reported by Van Goethem et al. [122]. In this approach, the nanofillers-hexane solution is contacted with the MPD-PSf membrane. Then the n. hexane is allowed to be completely evaporated under atmospheric conditions. Afterward, the IP reaction is completed by covering the TMC-hexane solution. This method is known as evaporation-controlled filler positioning (EFP) method (**Figure 2.10**). Both TFN membranes prepared according to [52] and [122] revealed superior water permeability without any significant loss in salt rejection compared to the control membrane prepared with the conventional method.

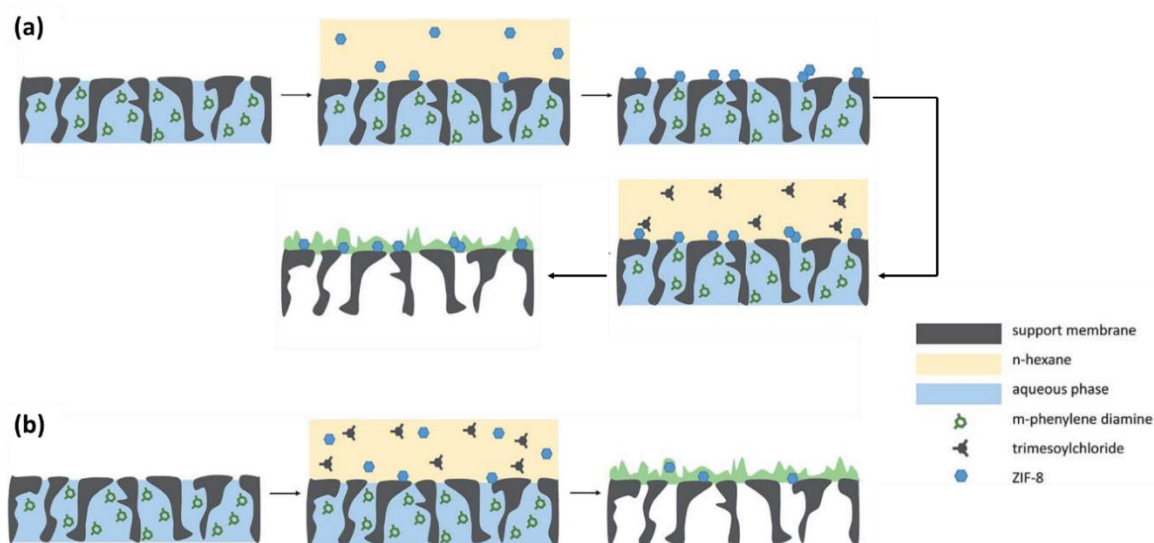


Figure 2.10: Schematic representation of (a) the evaporation-controlled filler positioning (EFP) and (b) the conventional TFN membrane preparation methods adapted from [122]

2.4.3 Chemical, mechanical and antifouling properties of TFN membranes

Presence of NPs inside the PA matrix in TFN membranes can provide the RO membranes with further resistance against chlorine attack, compaction and fouling in order to employ the membranes in industrial applications [16,134]. Zhao et al. [135] developed a TFN membrane with improved both chlorine resistance and antifouling properties by incorporating carboxyl-modified multi-walled carbon nanotubes (CNTs) into the PA skin layer. They attributed the improved performance of the TFN membrane to increase the surface hydrophilicity as well as increase the negatively surface charge which is necessary to decrease the fouling and increase the chlorine tolerance [135].

In addition, TFN membranes can provide better resistance to the compaction for RO applications. This can be concluded from the stable water permeation of the TFN membranes with time, which is usually attributed to the minimum influence of compaction under the applied pressure [136].

2.4.4 Separation mechanism of TFN membranes

Like PA TFC RO membranes, the separation of TFN membranes can also be explained by SDM. However, the addition of NPs into the PA skin layer affects strongly the membrane permeance and selectivity. This influence is due to combination of changes in the physicochemical properties of the PA film such as surface charge, hydrophilicity, thickness, crosslinking, porosity and creation of additional water channels [16,137].

In the first TFN membrane fabricated by Jeong et al. [15], the authors assumed that the mechanism for the improved water permeance includes: 1) Fast transport of water through the zeolite internal pores; 2) fast transport of water through the defects (voids) created between zeolite fillers and polymer matrix; and 3) the high hydrophilicity of the membrane surface due to the presence of the hydrophilic zeolite fillers [15]. Yin et al. [17] studied the separation performance of TFN membranes containing two different kinds of hydrophilic silica NPs; MCM-41 as porous fillers and solid silica as nonporous fillers. They found that water permeance in case of MCM-41 is much higher than that in case of nonporous silica. They concluded that the internal pores of MCM-41 act as a shortcut for water transport which played the major role on increase of water permeance.

Nevertheless, in different studies the nonporous fillers led to a significant increase in water permeance of their corresponding TFN membranes. For example, Jadav and Singeh [138] achieved increase up to 134% in water permeance of the TFN membranes compared to the reference TFC membrane by using nonporous silica nanofiller. According to the authors, the large increase in water permeance is owing to increasing the free volume because the silica NPs (3 nm) efficiently disrupted polymer chain packing which reduced the crosslinking and increased the water diffusion. Despite the difference in the fillers sizes between the work reported in [17] and [138], 100 nm and 3 nm respectively, the mechanism of water permeance enhancement is still unclear and needs further studies and detailed investigations.

The extent of water permeance enhancement is also influenced by the loading and the size of the inserted fillers. For example, Namvar-Mahboub et al. [139] have incorporated functionalized zeolite UZm-5 NPs into PA layer to improve the solvent resistance on NF membranes. They found out that the separation efficiency against oil molecules was negatively affected when the fillers loading exceeded 0.05 w/v%. According to the authors, the too much loading produced eminent agglomeration of NPS which distorted the structure of PA and reduced the degree of crosslinking. On the other hand, Lind et al. [140] investigated the influence of Zeolite 4 A crystal size on the properties of PA TFN membranes. They concluded that smaller zeolite size could be easily covered with the growing PA film and therefore, were beneficial for improving water permeance. Whereas, the bigger size may template film growth during the polymerization reaction leading to enlarging the thickness of PA layer in order to encapsulate big particles. Furthermore the exposure of NPs at the PA surface is highly possible in case of large particle sizes which ruins the separation performance [16].

Last but not least, the filler location inside the PA layer has also an important role on the separation efficiency of the TFN membranes. However, the tuning of the filler location is not an easy task, some useful attempts were done by Kong et al. [52] through the pre-seeding approach and by Van Goethem et al. [122] through the EFP method for fabrication of PA TFN membranes as explained in **Section 2.4.2**. Beside the fabrication method, the filler location is governed with the interaction of the fillers with the PA matrix. Fathizadeh et al. [141] suggested four types of interactions between the nanofiller (Zeolite NaX in that study) and PA as presented in **Figure 2.11**. According to the authors, the location of NPs in type 1 achieved the best separation performance because they were completely covered with PA without formation any voids defects. This case allows the solutes to be firstly rejected with the PA and then water molecules fast transported through the channels of zeolite. In case of the other interaction types, when some parts of NPs are exposed to the surface (type 2 and 3) or form defects due to agglomeration (type 4) the membrane revealed low separation efficiency.

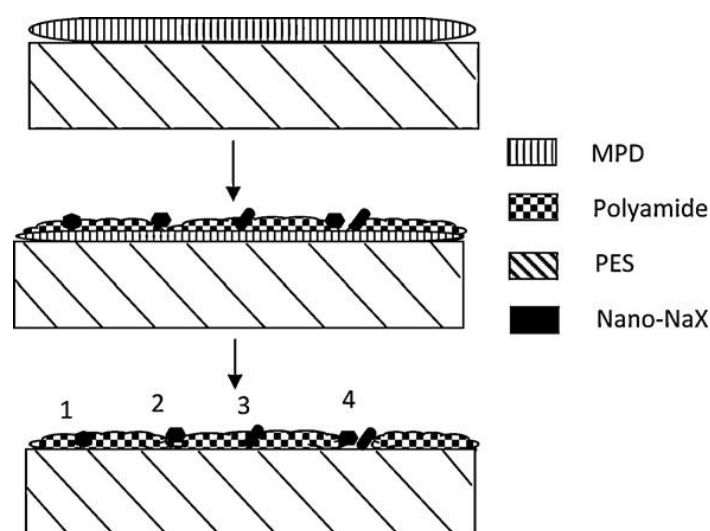


Figure 2.11: Schematic diagram for the types of interaction between the NPs and the PA matrix [141]

2.5 Mesoporous silica nanoparticles (MSN) as nanofiller

Mesoporous silica has attracted great deal of attention over the last years because of its uniform and tunable pore size, highly specific surface area, obvious surface hydrophilicity and easy surface functionalization [142]. All of these properties allow MSN to be adopted for several applications such as catalysis [143], adsorption [144] and drug delivery [145,146]. furthermore, MSNs were adopted to be used as nanofillers for TFN membranes preparation [18,127,147] which is the area of concern of this thesis.

2.5.1 Classification of porous materials

Silica (also known as silicon dioxide; SiO_2) is a thermally stable, chemically inert and inexpensive material [17]. It can be existed in several structures such as quartz which is a crystalline material or glass which is an amorphous material, and it can be porous or nonporous.

The pore size of the material, which is defined as the distance between the two opposite wall, was classified by the international union of pure and applied chemistry (IUPAC) to three main categories [142] (**Figure 2.12**):

- Microporous materials: the pore diameter is less than 2 nm.
- Mesoporous materials: the pore diameter is between 2-50 nm.
- Macroporous materials: the pore diameter is bigger than 50 nm.

Nevertheless, not only the pore width which describes the porous materials, but their adsorption behavior as well. The adsorption can be defined as a process in which a gas, or a liquid, accumulates on the outermost layer of a solid or a liquid phase leading to a relatively high concentration on the surface in comparison to the bulk [148].

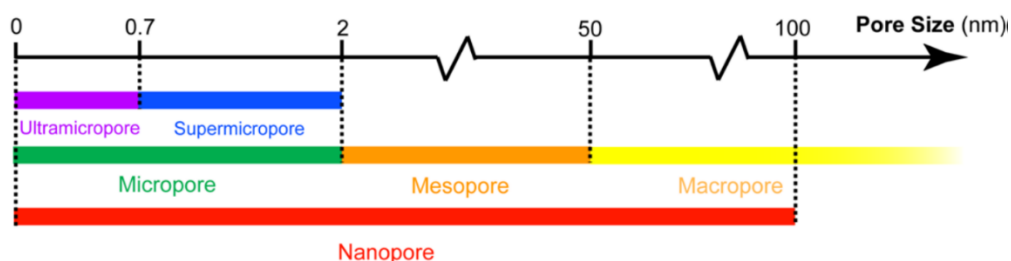


Figure 2.12: IUPAC classification of pores based on pore width [142]

As illustrated in **Figure 2.13**, the molecules adsorbed on the surface is known as adsorbate, while the molecules in the bulk are called adsorptive, and the substance on the surface where the adsorption occurs is known as adsorbent.

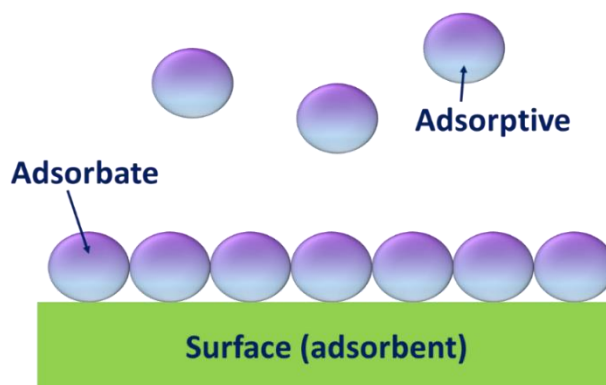


Figure 2.13: Schematic figure illustrating the definition of adsorbent, adsorbate and adsorptive

According to the interaction between adsorbent and adsorbate, the adsorption is classified to two categories [148] :

- (1) Physical adsorption or physisorption; in which the interaction between the adsorbent and adsorbate is weak and reversible,
- (2) Chemical adsorption or chemisorption; in which the interaction between the adsorbent and adsorbate is stronger and irreversible.

Adsorption of gas by a porous substance is a physisorption process and is described by the adsorption isotherm, which is a curve obtained by plotting the amount adsorbed as a function of relative pressure (P/P_0) at a constant temperature. IUPAC classified the different adsorption isotherms into six types which are grouped in **Figure 2.14** [149].

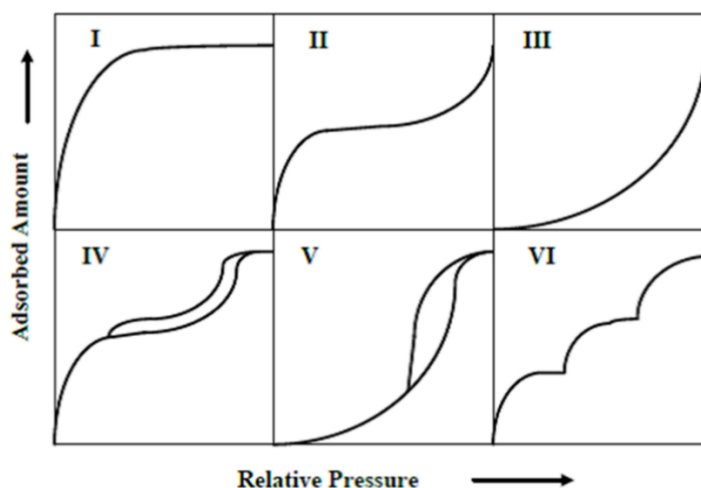


Figure 2.14: The six main types of adsorption isotherms according to IUPAC classification [149]

Type I isotherm: is typical for microporous materials, in which a very high adsorption occurs at low relative pressure ($P/P_0 < 0.01$). The plateau area at $P/P_0 > 0.01$ indicates for limiting uptake and depends on the cumulative accessible micropore volume in the sample.

Type II isotherm: is observed for macroporous or nonporous materials and represents unrestricted monolayer-multilayer adsorption. Therefore, the adsorption and desorption exactly follow the same path. At low relative pressure ($P/P_0 < 0.2$), the adsorption increases then shows linear area and finally increases again at higher relative pressure ($P/P_0 > 0.4$). The inflection point at which the linear area starts represents the completion of monolayer coverage and starts multilayer coverage. The amount adsorbed at this point is directly related to the surface area of the solid.

Type III isotherm: is similar to type II adsorption isotherm, however, it is not common because the interaction among the adsorbate molecules is stronger than the adsorbate-adsorbent interaction. Therefore, the uptake of gas molecules dominates the process until a sufficient coverage formed on the surface and the adsorption increases.

Type IV isotherm: is characteristic for mesoporous materials. At the low pressure is similar to type II isotherm indicating a monolayer-multilayer adsorption on the wall of mesopores. At higher relative pressure, the adsorbed gas condenses into a liquid-like state inside the pores at a pressure below the saturation pressure. This is known as capillary condensation. Therefore, the isotherm shows hysteresis in which the desorption curve doesn't retrace the adsorption curve leading to formation of a wide loop known as a hysteresis loop and corresponds to the capillary condensation, pore filling and the mechanism of the condensed liquid from the pore. The shape of the hysteresis loop is associated with the shape of the pores.

Type V isotherm: is also characteristic for the mesoporous materials, but different from the type IV because the weak adsorbate-adsorbent interaction. Therefore, at low pressure it is similar to type III, but at higher pressure, there is a hysteresis loop such as type IV isotherm.

Type VI isotherm: is due to layer by layer adsorption on a highly uniform surface. These stepped layers are formed by separate layer adsorption on each other.

2.5.2 Overview of MSN history

In 1992, the scientists of Mobil group synthesized for the first time a well ordered mesoporous silica by reaction of soluble silicate such as alkoxysilane in presence of a cationic surfactant such as alkyltrimethylammonium bromide (C_nTMA ; n: carbon number in the alkyl chain) [150]. This family of silica compounds is known as M41S materials and includes several mesoporous silica according to the shape of porous structure (**Figure 2.15**) such as hexagonally

cylindrical pore structure (MCM-41; Mobil composition of matter No. 41), cubic pore structure (MCM-48) and lamellar pore structure (MCM-50). Among the Mobil mesoporous silica types, MCM-41 demonstrates long range ordering which giving rise to mesoporous channels within the structure. Beside the regular mesostructure, the specific pore diameter (2-6 nm) of MCM-41, high surface area, and the large pore volume allowed it to be an excellent member as adsorption platform [151].

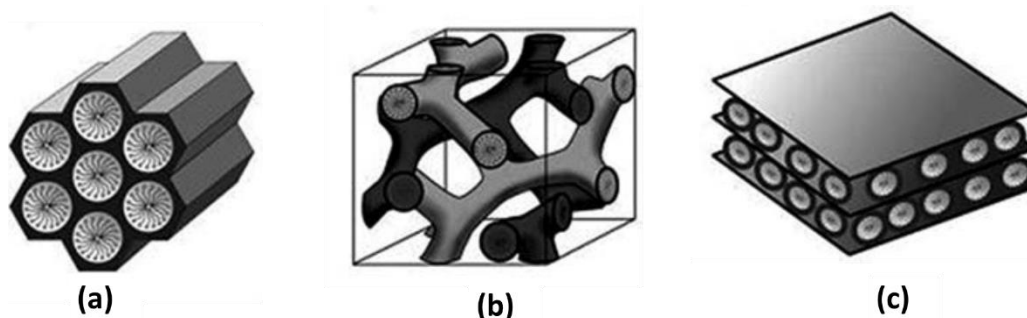


Figure 2.15: Structure of mesoporous M41S materials: (a) hexagonal MCM-41, (b) cubic MCM-48 and (c) lamellar MCM-50 [151]

However, the revolutionary potential of MSN in the drug delivery and release applications after the proposed MCM-41 by Mobil company, it was not the first attempt to synthesize mesoporous NPs. In 1971, Chiola et al. reported that low density silica can be obtained by hydrolysis and condensation of tetraethyl orthosilicate (TEOS) in presence of cationic surfactant [152]. Despite the authors used the same preparation approach which has been used later by Mobil scientists, they concerned only with the low bulk density silica formation and had no report concerning the mesoporous structure which was confirmed later after 28 years by Renzo et al.[153]. Furthermore, in 1990 Yanagisawa et al. [154] reported the first intentional preparation of mesoporous silica by using a complex of polysilicate kanemite with alkyltriethylammonium. However the poor distribution of the mesoporous structure limited the application of this product [155]. In 1998, Stucky and his coworkers [156] developed a similar kind of MSN, (namely Santa Barbara amorphous No. 15; SBA-15), but they replaced the cationic surfactant in case of MCM-41 with nonionic amphiphilic surfactant such as triblock copolymer.

Like MCM-41, SBA-15 has an ordered hexagonal symmetry but showed surface area and pore volume lower than MCM-41. Nevertheless, it has a larger pore diameter (4.5-30 nm) and a thicker pore wall that provide the material with higher mechanical, hydrothermal stability. Therefore SBA-15 also attracted much attention in the adsorption applications.

2.5.3 Synthesis of MSN

In general MCM-41 NPs are prepared by using modified Stober's method during sol-gel process in presence of cationic surfactant as a template or a structure directing agent [150,157]. The sol-gel chemistry is a widely investigated process for preparation of many inorganic oxides from an aqueous metal alkoxide solution [116,158].

There are other methods for the synthesise of silica NPs such as reverse microemulsion and flame synthesis [159] but sol-gel process can produce homogeneous and pure silica particles due to its ability to control particle size, pore size, pore size distribution and morphology through monitoring the reaction parameters [159]. The sol-gel reaction involves hydrolysis and condensation reactions of the metal alkoxide monomer in order to form the colloidal particles (sol) and convert them later to a polymer network (gel) [160] as presented in (**Reaction 2.1 to 2.3 in Figure 2.16**).

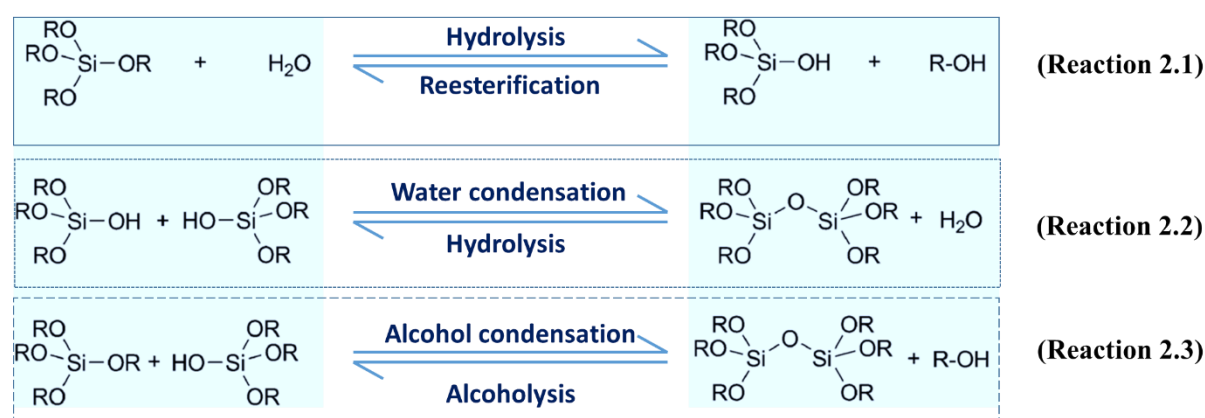


Figure 2.16: Scheme illustrating the sol-gel general reactions

Alkoxysilanes such as TEOS or tetramethyl orthosilicate (TMOS), are usually used for silica production [116]. the hydrolysis occurs according to **Reaction 2.1 in Figure 2.16** by addition of water to the alkoxysilane solution to generate a silanol group. Afterword, the silanol groups condense with each other (**Reaction 2.2 in Figure 2.16**) or with other alkoxysilane molecules (**Reaction 2.3 in Figure 2.16**) to form the siloxane particles seeds into the sol. Further condensation of silicate cluster leads to formation of the gel which contains the silicate network [161].

2.5.3.1 Factors affect the sol-gel reaction

The hydrolysis and condensation reactions are strongly influenced by several factors such as precursor properties, water/precursor ratio and pH of solution. The material to be used as precursor should be soluble in the reaction media and reactive enough in order to make the

hydrolysis and condensation reactions in order to form the polymer network [162]. The most common example of silica precursors is alkoxy silane such as TEOS. The water/TEOS molar ratio is also an important parameter that affects the sol-gel reaction. According to **Reaction 2.1** in **Figure 2.16**, at a fixed TEOS concentration, the increase in water quantity results in corresponding increase in the hydrolysis rate. Similarly on the basis of Le Chätelier principal, the water condensation step (**Reaction 2.2** in **Figure 2.16**) is expected to be hindered by increasing the water/TEOS ratio [160]. However, the condensation step was found to be accelerated with increasing the water/TEOS ratio which is contradictive with the theoretical expectations. This can be attributed to the increase in both silica solubility and the hydroxyl ion catalyst [160]. One more important factor is the influence of solution pH on the charge of silica. The charge state of the silica has strong impact on the rate of hydrolysis and condensation, which affects the mesostructure of obtained material [163]. The hydrolysis of Si-OR bond in TEOS is occurred at both high and low pH solutions. The rate of hydrolysis exhibits a minimum at pH = 7 and increases in both lower and higher pH [158].

On the other hand, the condensation rate has an opposite behavior which shows a maximum at pH around 7 and a minimum at pH around 2 as depicted in **Figure 2.17**. According to the figure, at low pH value (acidic catalysis), below the isoelectric point of silica (IEP ≈ 2), the silica species become positively charged. This hinders the assembly with the cationic surfactant and minimizes the condensation rate to be minimum at pH < 2 . Under alkaline conditions (pH > 7), the silicate with the negative charges can be assembled with the cationic surfactant due to the nucleophilic attack and the condensation rate reach maximum at pH 7-7.5. Then the condensation rate decreases at pH > 7.5 because the gradual instability of silicates at higher pH values [164]. Nevertheless, the synthesis of MSN such as MCM-41 is conducted at high pH (≈ 12) due to the strong interaction between the cationic surfactant (CTAB) and the silicate ions can stabilize the formed silica rather than silica dissolving [158,164].

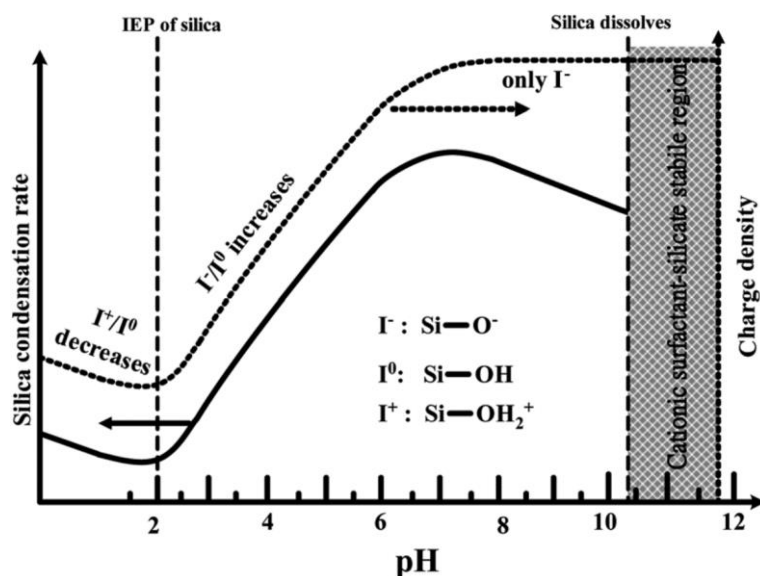


Figure 2.17: Effect of pH on the silica condensation rate, charge properties and charge density on the surface of the silica species [158]

2.5.3.2 Formation mechanism of MSN

Liquid crystal templating (LCT) mechanism was proposed by both Mobil and Santa Barbara scientists to explain the formation of the ordered mesoporous structure in MCM-41 and SBA-15, respectively [150,162]. A surfactant is the molecule which consists of a polar and hydrophilic part (called a head), and a nonpolar and hydrophobic part (called a tail) (**Figure 2.18a**). The hydrophilic component can interact with the charged precursor, whereas the hydrophobic component can solubilize the organic species.

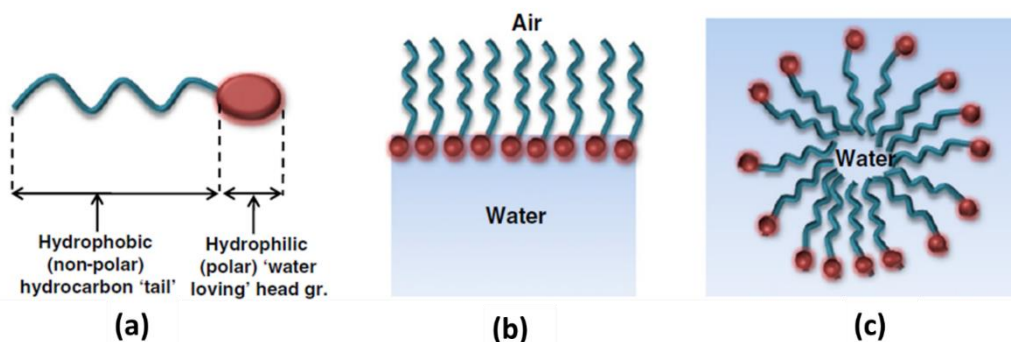


Figure 2.18: Surfactant molecule and its behavior in water [167]

In a simple surfactant/water system, the relation between the surfactant concentration and its activity in water is shown in **Figure 2.18**. At the low concentration of surfactant, the surfactant

molecules energetically exist as individual molecules and tend to arrange on the surface (**Figure 2.18b**). When the concentration increases, the surface becomes crowded and the molecules aggregate within a cluster in which the hydrophobic portions are oriented against water and the hydrophilic parts are exposed to water [165]. This formed cluster is called micelle (**Figure 2.18c**). The initial concentration threshold at which the single molecules aggregate and form the micelle, is called critical micelle concentration (CMC) [166]. Above the CMC, the self-assembled micelles form 2D cylindrical or 3D spherical arrays which helps in the pore generation [167].

The CMC depends on the chemical structure of the surfactant. For example, the higher the length of hydrophobic tail, the lower CMC. This can be explained because of the longer chain tend to bond together which minimizes the energy and form stable system. It is worth mentioning that surfactants can be classified according to the charge of the polar head to four main groups:

- Cationic surfactants: dissociate in water into an anionic head usually halide and an amphiphilic cationic tail. The tail is a long alkyl chain ended with a positive charge group such as amine salt or quaternary ammoniums. The common example is cetyltrimethylammonium bromide (CTAB).
- Anionic surfactant: dissociate in water into a cationic head usually an alkaline metal ion such as K^+ or Na^+ and an amphiphilic anionic tail. The tail is a long alkyl chain ended with a negative charge group such as alkylbenzene sulfonate or lauryl sulfate. The common example is sodium dodecyl sulphate (SDS)
- Nonionic surfactant: it does not dissociate in water. Nevertheless, this kind of surfactant can be dissolved in water due to presence of a covalently bonded oxygen-containing hydrophilic group which is bonded to a hydrophobic group. The most common example of the nonionic surfactant is the block copolymers such as pluronic P123 or F127.
- Zwitterionic surfactant: This is the last family of surfactants. They have two charges of different sign on their head group giving a neutral charge. The most common positive charge is produced by an ammonium group and the negative charge may vary, but most often carboxylate. The common example is lauryl betaine. The chemical structure of some surfactant examples is depicted in **Figure 2.19**.

In this thesis, we have been working basically with CTAB as a cationic surfactant which have been used for synthesis of MSN.

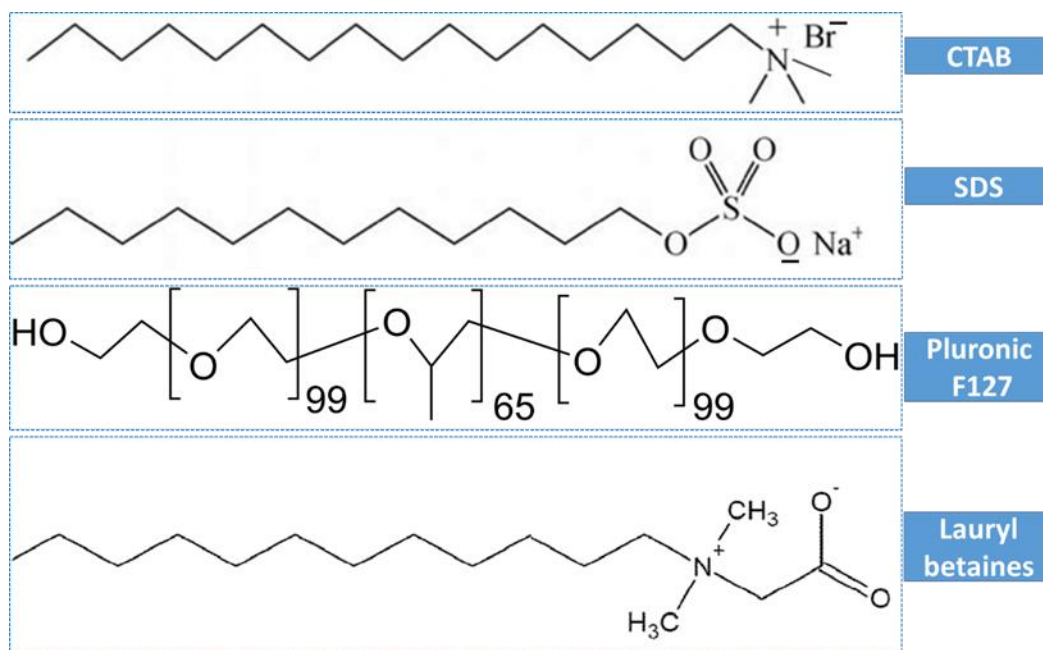


Figure 2.19: Chemical structure of some common surfactants

Since 1992, several researches and studies have been carried out in order to understand the formation mechanism of mesoporous structure [167–169]. The synthesis of MSN with the aid of surfactant can occur in two possible pathways according to the surfactant concentration:

(1) *The cooperative self-assembly (CSA) mechanism:*

In this pathway, the mesoporous materials are prepared at low concentration of surfactant [168,170]. Therefore, there is a concurrent aggregation of self-assembled surfactant micelles with the added silicate anions and the liquid crystal phase containing both micelles and precursor molecules can be established as presented in **Figure 2.20 (a)**.

(2) *The LCT mechanism:*

Here the concentration of surfactant is high enough to allow the micelles to form a true liquid crystal phase without requiring the presence of silicate precursor [167,168] (cf. **Figure 2.20 (b)**).

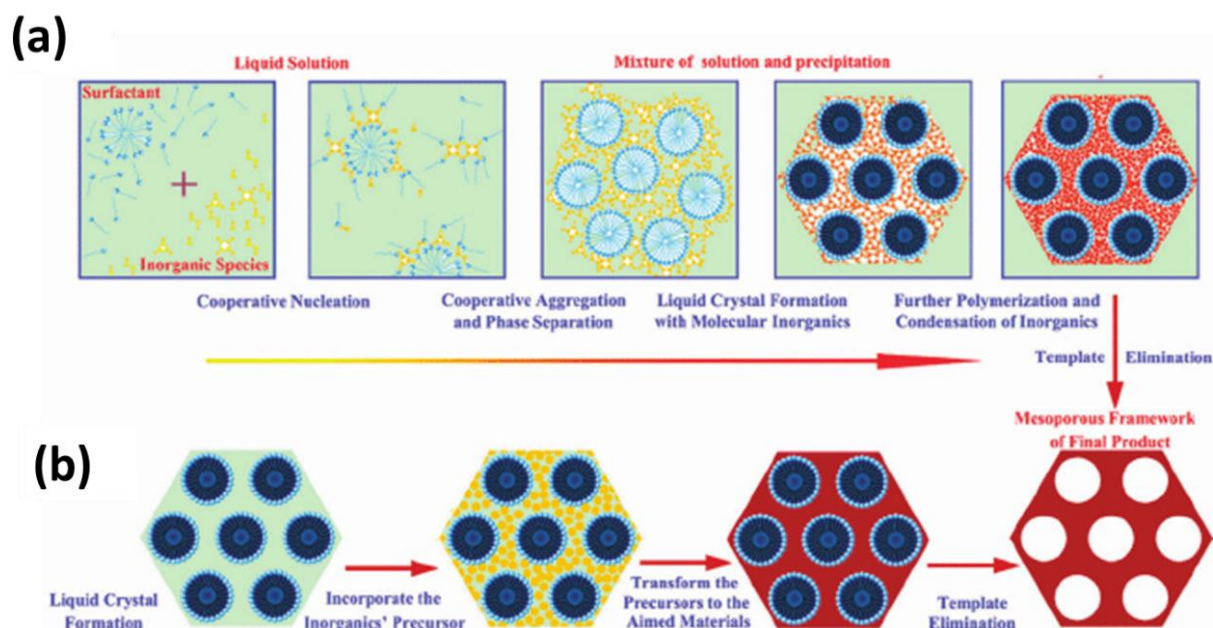


Figure 2.20: Formation of mesoporous structure: (a) cooperative self-assembly and (b) true liquid crystal templating process [168]

2.5.3.3 Control of characteristics of MSN

2.5.3.3.1 Control of particle size

Particle size is a very important property for the different applications of MSN. Several attempts have been made to get MSN with controlled particle size in the range of tens of nanometers to tens of micrometers. This can be achieved by changing some experimental parameters such as reaction temperature, stirring rate, adding suitable additives and optimizing the surfactant and precursor concentrations [158,171–173]. It was reported that low reaction temperature and rapid stirring rate may lead to formation of MSN with small particle diameter. This is because the low temperature and rapid mixing rate can reduce the concentration of silica-surfactant micelles and supports the particle growth [116,172]. However, optimizing the surfactant and precursor concentration considers the key factor to control the particle size [172].

Yamada et al. [171] reported that high surfactant/precursor molar ratio produced smaller particle diameter because the high surfactant concentration compared to precursor improved the dispersity of TEOS in water which increases its hydrolysis rate leading to increasing the nucleation as compared to the particle growth. The low surfactant/precursor molar ratio produced the opposite results.

2.5.3.3.2 Control of pore size and mesoporous structure

Optimizing both surfactant and precursor concentrations not only affect the particle size but can also affect the mesoporous structure of the particles. The higher concentrations of TEOS

were found to yield disordered mesoporous structure whereas lower TEOS concentration may not be enough to form mesoporous structure. Consequently, the TEOS concentration should be optimized to achieve the ordered mesoporous structure [174]. On the other hand, the low quantity of CTAB can be consumed rapidly by forming a composite with the hydrolyzed TEOS and therefore the formed mesoporous structure is not homogeneous. Moreover, when CTAB concentration is lower than CMC, the individual CTAB molecules can act as a flocculant causes aggregation of NPs [116,171]. Furthermore, the type of surfactant affects the pore size of MSN. It was found that the pore diameter can be minimized by using a surfactant with a short chain length and can be maximized by using longer chain length [116].

In some applications such as drug delivery, the larger pore size of MSN is a highly recommended. In a recent work, Cha et al. [175] synthesized extra-large pore diameter MSN (≈ 25 nm) in order to achieve a high loading capacity of large biomolecules. They employed a large amount of ethyl acetate as an organic additive in presence of CTAB as a pore expansion agent, which expanded emulsion in the templating CTAB micelles.

2.5.4 Challenges of MSN as nanofillers (agglomeration, dissolution and uncertainty of separation mechanism)

Despite that MSN were frequently used as nanofillers for TFN membranes, the desired improvement of membrane performance is limited. This limitation of MSN is attributed to their tendency to agglomeration and dissolution in aqueous solutions. Because of the abundance of hydroxyl groups attached on the MSN surface, the surface is hydrophilic. This hydrophilicity limits the dispersion of MSN in the organic solvent during the IP reaction. As a result, it may cause their agglomeration in PA films even at low concentration. Therefore, it influences strongly the performance of the formed PA layer. One more challenge which faces the MSN as good nanofillers for fabrication of MSN is their dissolution at aqueous solutions which impacts on altering their size and their porous structure. The dissolution of silica in water occurs according to **Reaction 2.4** and leads to silicic acid formation. The rate of dissolution increases with increasing pH of the solution. At high pH, silicic acid is ionized to form highly soluble H_3SiO_4^- and $\text{H}_2\text{SiO}_4^{2-}$ ions as can be seen in **Reactions 2.5** and **2.6** [176,177].



Pham et al. [21] studied the effect of dissolution of mesoporous silica (SBA-15) on the reactivity of silica-supported iron oxide catalysts. They found that the reactivity toward H_2O_2

composition decreased by increasing the degree of silica dissolution, due to the fact that the dissolved silica re-deposited on the surface of the catalyst and blocked its active sites responsible for the degradation of H₂O₂.

2.5.5 Modification of MSN

As mentioned before, MSN possess a very high surface area and their surface is covered with (Si-OH) groups which makes the functionalization of both external surface and internal pore surface adjustable. Functionalization of silica nanofillers was suggested in order to minimize their agglomeration and improve their integration within the PA film [16,128,132,178,179]. For instance, in a recent work, Pang and Zhang [132] have fabricated hydrophobic-fluorinated silica / PA TFN membranes. They found out that hydrophobic functionalization of silica NPs improved their dispersion in the organic solvent during IP process. As a result, the integration of NPs inside the PA layer was also enhanced which improved the salt rejection of the membrane, however the water permeability remained unchanged.

Moreover, functionalization of silica surface with organic substances has been considered as a good strategy to stabilize them against dissolution in aqueous media [180]. Barba et al. have found that functionalization of SBA-15 NPs by different organosilanes containing methyl, octyl and aminopropyl groups improved their stability and decreased the amount of dissolved silica, due to formation of an organic layer passivating the surface [181].

In general, there are two major methods to functionalize the surface of MSN with the organic functional group include, grafting (post-synthesize) method and co-condensation (one-pot synthesis) [144]. In the grafting method, the Si-OH groups on the surface act as the active site for organic functionalization. The pre-synthesized MSN are allowed to be modified by attachment of organic functional group to the surface, usually after surfactant removal [144,182], as illustrated in **Figure 2.21**. In co-condensation method, the silica precursor and the organic silane compound are condensed together during in one step during the silica synthesis (cf. **Figure 2.21**) [182].

Each of the two methods has certain advantages; the grafting method is usually used to integrate a wide range of the functional groups to the pre-synthesized MSN and it can maintain the original mesoporous structure. Moreover, the selective functionalization can be achieved by the grafting method [183,184]. On the other hand, the co-condensation method is proposed if a uniform surface coverage with functional groups is desired in a single step synthesis [185].

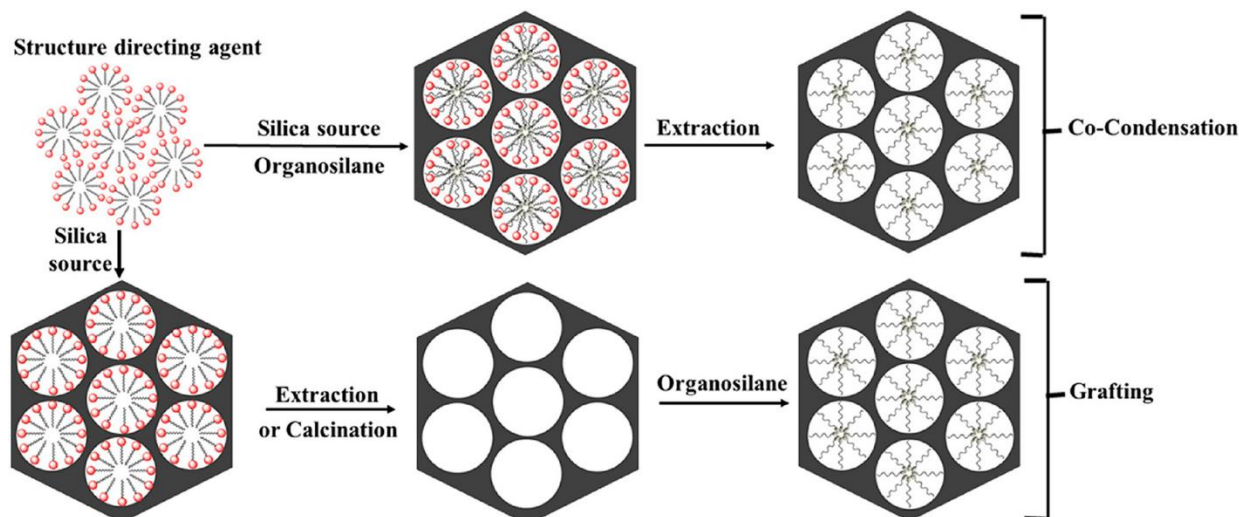


Figure 2.21: Formation of mesoporous structure: (a) cooperative self-assembly and (b) true liquid crystal templating process [144].

The grafting method is employed for selective functionalization of MSN. Surface functionalization with organic groups by grafting method is usually carried out via silanization reaction.

In the silanization reaction, the silane compound (using trichlorosilane as an example) willingly reacts with the hydroxyl groups present on the surface of MSN. Due to the highly reactive chloride - head groups ($R-SiCl_3$), the reaction can be conducted at room temperature with no need to catalyst or temperature as shown in **Figure 2.22**.

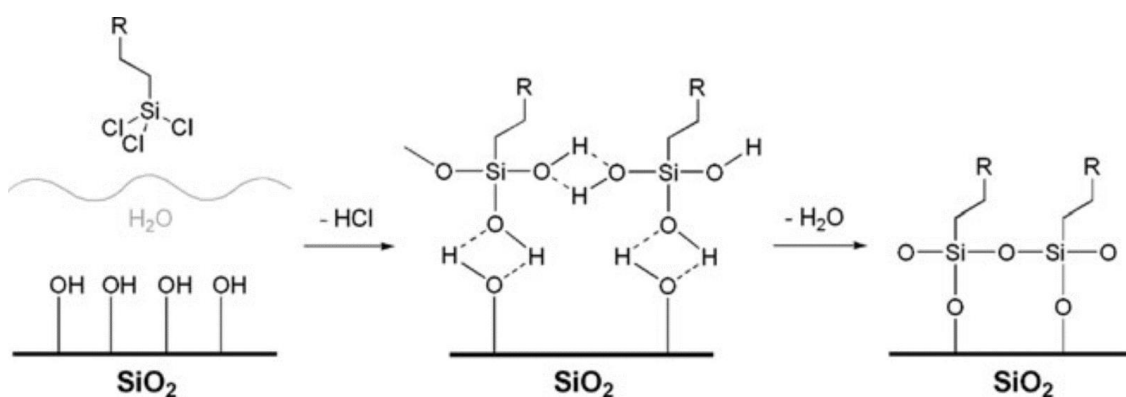


Figure 2.22: Schematic representation of the silanization reaction process using trichlorosilane molecules

It was assumed that the silane molecules are first hydrolyzed by a trace amount of water adsorbed on the surface of NPs or presented in the solvent. The hydrolyzed silane compound then can react with silanol group which are presented either on the silica surface or on adjacent silane molecules forming a network layer [186]. It is supposed that one silane molecule can

form three bonds with the surface in case of using trichlorosilane compound. Nevertheless, the alkyl chain length of the silane compound may cause steric hinderance and limit this assumption. Therefore, formation of one or two bonds is much desirable.

Mesoporous silica is well-known to exhibit two ‘different’ surfaces, the external surface and the surface of the internal mesopores. It was mentioned that functionalization of MSN by grafting method requires the reaction between silane compound and the pre-synthesized MSN after surfactant templet removal. However, the presence of surfactant in the mesopores can represent the key factor for selective functionalization.

De Juan and Ruitz-Hitzky [189] introduced the concept of selective functionalization of the external and internal surfaces of MCM-41. First, the grafting reaction was carried out by exposure the solution of trimethylsilyl chloride to the as-synthesized NPs whose pores were still filled with the surfactant. This led to functionalization of the external surface only due to the steric hinderance with the surfactant inside the meso-channels. The surfactant was then extracted, and the internal pores were then functionalized with phenylpropyldimethyl chlorosilane [187] (**Figure 2.23**). Different approach was proposed by Shephard et al. [188] for selective functionalization of the calcined MCM-41. They first modified the NPs with dichlorodiphenylsilane to passivate the external surface and minimize its involving in the reaction, then modified the internal pores with different substance. They relied to passivate the external surface on it is being more accessible and is functionalized predominantly over the internal mesopore surface [188,189] (cf. **Figure 2.23**).

Similar approach was suggested by Bouchoucha et al. [190] to functionalize only the external surface of MCM-48 with PEG-silane. However, to achieve this goal, the authors selected PEG-silane compound with a size much bigger than the size of internal mesopores to ensure the functionalization of the external surface only.

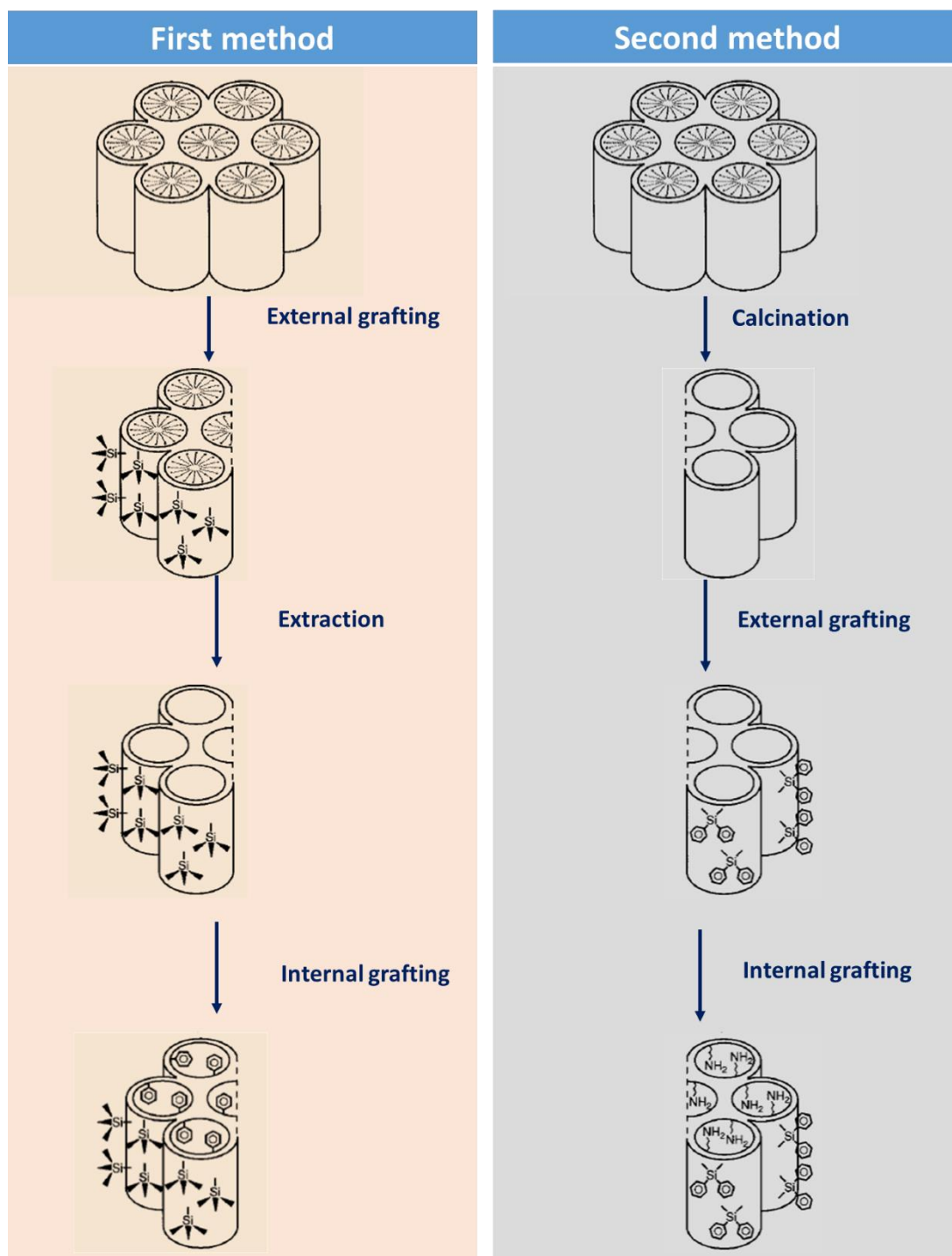


Figure 2.23: Methods of selective grafting on external and internal surfaces of MSN; the first method proposed by De Juan and Ruitz-Hitzky and the second method proposed by Shephard et al. [189]

Chapter 3

3. Materials and methods

3.1 Materials

3.1.1 Materials for MSN

For preparation, functionalization, and determination of dissolved concentration of MSN, the chemicals listed in **Table 3.1** were used.

Table 3-1: Materials and chemicals used for preparation, functionalization, and determination of dissolved concentration of MSN

Materials and Chemicals	CAS-NO	Source
Cetyltrimethylammonium bromide (CTAB; ≥98%).	57-09-0	Sigma-Aldrich
Tetraethyl orthosilicate (TEOS; 98%)	78-10-4	Sigma-Aldrich
Octadecyltrichlorosilane (OTS; ≥90%)	112-04-9	Sigma-Aldrich
Methyltrichlorosilane (MTS;98%)	75-97-6	Sigma-Aldrich
sodium hydroxide (NaOH)		
Toluene	108-88-3	Fisher
Methanol (HPLC; 99.9 %)	67-56-1	Fisher Chemical
Molecular sieve 4 Å (0,4 nm; type 514; pearls)	1318-02-1	Carl ROTH GmbH + Co. KG
Ammonium molybdate tetrahydrate (99.98%)	12054-85-2	Fluka Analytical
Sodium metasilicate nonahydrate (≥98%)	13517-24-3	Sigma-Aldrich
oxalic acid	144-62-7	Sigma-Aldrich
hydrochloric acid (HCL)		Bernd Kraft
Sodium hydroxide (NaOH)		Bernd Kraft
Water (Milli-Q; ultrapure; 18.1 MΩ cm-1)		Millipore

3.1.2 Materials for membranes

For preparation and characterization of the support PES membrane, as well as TFC and TFN membranes, the chemicals listed in **Table 3.2** were used.

Table 3-2: Materials and chemicals used for preparation, characterization, and performance evaluation of the membranes

Materials and chemicals	CAS number	Source
Polyethersulfone (PES; Ultrason E6020P)	25608-63-3	BASF
Polyvinylpyrrolidone (PVP; K 30)	-	Serva Feinbiochemica GmbH & Co.
N-methyl-2-pyrrolidone (NMP; EMPLURA®; 99 %)	872-50-4	Merck
Triethylene glycol (TEG; 99 %)	112-27-6	Acros
m-phenylenediamine (MPD; ≥99%)	108-45-2	Sigma-Aldrich
1,3,5-benzenetricarbonyl trichloride (trimesoylchloride, TMC; 98%)	4422-95-1	Acros
n-Hexane (for analysis; 95 %)	110-54-3	Acros
Dextran 4 kDa		Serva Feinbiochemica
Dextran 35 kDa		Serva Feinbiochemica
Dextran 100 kDa		Serva Feinbiochemica
Dextran 200 kDa		Serva Feinbiochemica
Dextran 2000 kDa		Serva Feinbiochemica
Sodium hydroxide (NaOH)	-	Bernd Kraft
Potassium chloride (KCl, 1M)	-	Bernd Kraft
Potassium hydroxide (KOH, 1M)	-	Bernd Kraft
Hydrochloric acid (HCl, 1M)	-	Bernd Kraft
Sodium chloride (NaCl; AnalaR NORMAPUR; 99.9%)	7647-14-5	VWR
Ethanol absolute	64-17-5	Fisher chemicals
Water (Milli-Q; ultrapure; 18.1 MΩ cm-1)		Millipore

3.2 Preparation and characterization of MSN nanofillers

3.2.1 Preparation of MSN

MSN preparation was conducted by the sol–gel method as reported in [191] using different CTAB/TEOS ratios. 0.09 – 0.9 g (0.25–2.5 mmol) of CTAB was first dissolved in 240 ml of DI water. Aqueous NaOH solution (2.00 M, 1.75 ml) was then added and the solution temperature raised to 80 °C. Thereafter, 2.8 g (13.5 mmol) of TEOS were added to the solution, followed by refluxing at 80 °C for 2 h under vigorous stirring. The solid product (as-synthesized

MSN) was filtered, washed with deionized water and methanol, and dried in a vacuum oven at 45 °C for 12 h. Two methods were employed to remove the surfactant template (CTAB), i.e. calcination at high temperature (600 °C) for 6 h [192] or extraction process [193] in which the collected precipitate was resuspended in methanol and hydrochloric acid (V(MeOH) / V (HCl) =18) and the solution was allowed to reflux for 24 h at 90 °C. The template-removed product was filtrated and dried overnight in a vacuum oven at 60 °C to yield MSN as a white powder

3.2.2 Controlled functionalization of MSN

Two methods were employed to control the extent and localization of OTS functionalization of MSN.

3.2.2.1 External pore surface functionalization (LMSN)

The as-synthesized MSN was initially activated under vacuum at 100 °C for 12 h to remove the adsorbed water and to facilitate the reaction of silanol groups with the functionalization agent. The activated NPs (MSN; 1.0 g) were dispersed in 30 ml of dry toluene, under argon atmosphere and allowed to react with 0.5 – 5 g of OTS (1.28 – 12.8 mmol OTS/g of MSN) at 90 °C under reflux for 20 min. The suspension was cooled to room temperature, filtrated and the obtained particles were collected. The non-reacted organosilane was removed by washing the particles thoroughly with toluene and methanol; then the particles were dried under vacuum at 60 °C overnight. The surfactant was finally removed using the extraction method (cf. **Section 3.2.1**). It was anticipated that the presence of CTAB restricts grafting of the interior pores and allows functionalizing the external pore surface only.

3.2.2.2 Internal and external pore surfaces functionalization (HMSN)

The surfactant was firstly removed (cf. **Section 3.2.1**). Thereafter, the extracted MSN were functionalized as described before (cf. **Section 3.2.1.1**), but at prolonged reaction time (up to 6 h) to ensure that the functionalization extended inside all pores. Functionalization of MSN using methyltrichlorosilane (MTS) was conducted using the same way as in OTS. The preparation and functionalization of MSN are presented in **Figure 3.1**.

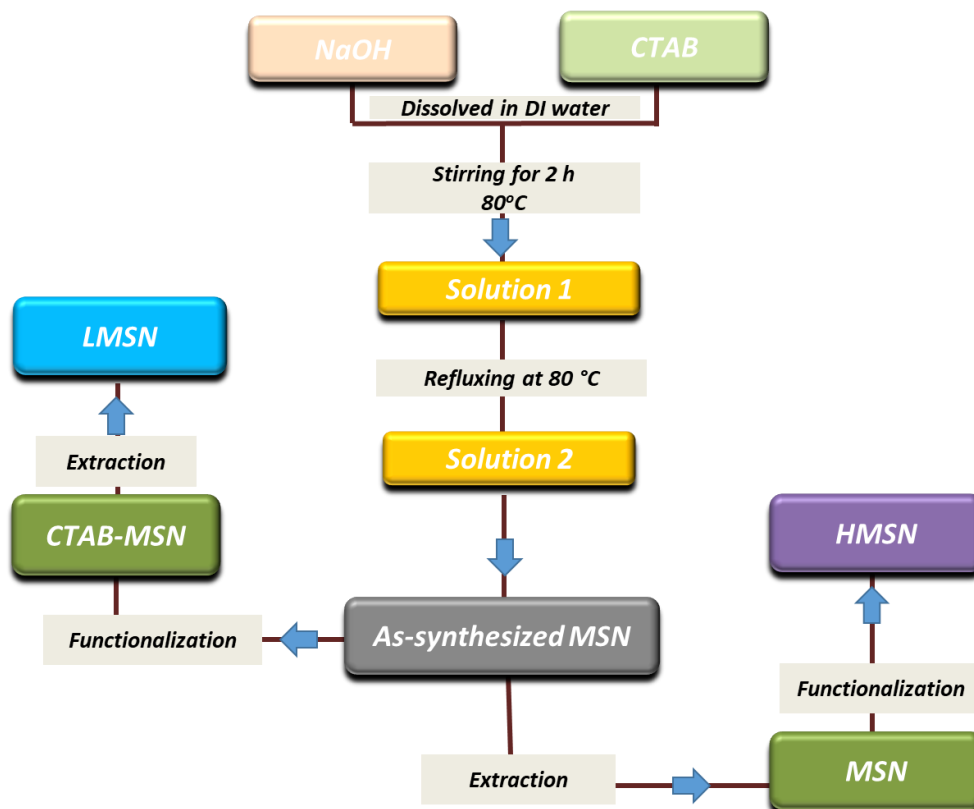


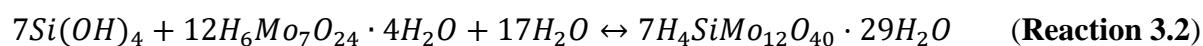
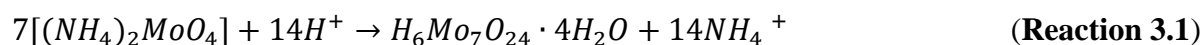
Figure 3.1: Schematic diagram illustrating preparation and functionalization of MSN

3.2.3 Dissolution of MSN

All dissolution experiments were carried out in a 250 ml polyethylene flask at room temperature. Each kind of silica (MSN, LMSN and HMSN) was dispersed in Milli-Q water (2 g/L). Due to the hydrophobic character of LMSN and HMSN, they were first wetted with a few drops of ethanol before dispersing in water. The dispersion was vigorously stirred. The initial pH of 200 ml of the silica solution was adjusted by HCl (1 M) and NaOH (1 M) to be 5 and 9, respectively. All samples were analyzed twice at each pH value, and the experiment was continued for 170 h. 5 ml of the aliquot for each sample were collected periodically and filtered through a 0.2 μm nylon filter before analysis of dissolved silica.

3.2.3.1 Determination of dissolved silica concentration:

Dissolved silica concentration was determined using molybdsilicate method [194]. The silica reacts with ammonium molybdate reagent and produces molybdsilicic acid according to the **Reactions 3.1 and 3.2**) [195]:



The molybdosilicic acid has a yellow color and can be detected using the spectrophotometer at wavelength 410 nm.

The used reagents:

Four reagents were used during this method:

- a. Hydrochloric acid (HCl), 1 + 1, one volume of concentrated HCl was mixed with one volume of milli-Q water.
- b. Ammonium molybdate reagent (75 mg/L); 10 g Ammonium molybdate tetrahydrate were dissolved in water, with stirring and gentle warming, and were diluted to 100 mL. then the solution pH was adjusted using NaOH or NH₄OH to be 7 to 8 and stored in a polyethylene bottle.
- c. Oxalic acid solution (75 g/L); 7.5 g oxalic acid dehydrate were dissolved in water and diluted to 100 mL. The oxalic acid was added to destroy the molybdophosphoric acid, which results from the reaction of ammonium molybdate with any phosphate may present with silica [196].
- d. Standard silica solution (1 mL=10 µg SiO₂); 0.473 g of sodium metasilicate nonahydrate were dissolved in water and diluted to 1 litre and Stored in a tightly stoppered plastic bottle.

Photometric measurement

At least four standards covering the desired concentration range were prepared by proper dilution of the standard silica solution (0-1000 µg). Then 50 mL aliquots of the standards were transferred to a plastic 100 mL-flask and 1 mL of HCl (1 + 1) and 2 mL of the ammonium molybdate solution were added quickly and were allowed to be mixed together for at least five minutes. 2 mL of oxalic acid were added with well mixing and left for at least 2 min then the absorbance was measured against Milli-Q water at 410 nm using the spectrophotometer. The reagent blank was prepared with the same method using all previous reagent except the standard silica solution and its absorbance against water was also measured. The calibration curve produced from this method is presented in **Figure 3.1** with $R^2 = 0.99$. 2 ml of the aliquot were diluted to 50 mL with milli-Q water and were analyzed as before. It was necessary to filtrate the aliquot taken from the initial sample through a 0.2 µm filter before performing the analysis to remove the turbidity. The produced dissolved silica concentration was then calculated by **Equation 3.1**

$$mg\ SiO_2/L = \frac{\mu g\ SiO_2\ (in\ 55\ mL\ final\ volume)}{mL\ Sample}$$

Equation 3.1: Calculation of dissolved silica concentration

3.2.4 Characterization of MSN

3.2.4.1 Hydrodynamic particle size analysis

The hydrodynamic particle size and particle size distribution of MSN was determined using dynamic light scattering (DLS) method using Particle Metrix Stabisizer at a laser wavelength of 500 nm and a power of 6 mW. Each sample was measured three times over a period of 60 s for each run to get the number average diameter, and the result is the average of the three measurements

3.2.4.2 Analysis of solid state structure

The solid-state structure of the native and partially dissolved MSN was analyzed using a Panalytical Empyrean X-ray powder diffractometer (XRD) with CuK α radiation source ($\lambda = 1.54 \text{ \AA}$; 40 kV and 40 mA). The samples were scanned from 1 to 15 $^\circ$ (2θ) with a step size of 0.007 $^\circ$.

3.2.4.3 Nitrogen adsorption measurements

Nitrogen adsorption measurements of the native and partially dissolved nanofillers were performed at 77 K using a BELSORP-max instrument. Before adsorption measurements, all MSN samples were degassed under vacuum at 200 $^\circ\text{C}$ for 6 hours. The specific surface area was calculated by Brunauer–Emmett–Teller (BET) method and the pore size distribution obtained from the nitrogen adsorption was calculated using density functional theory (DFT) model, by generating a model isotherm (quantity adsorbed versus pressure) while accounting for solid and gas interactions along with geometrical configuration of the pores.

3.2.4.4 Determination of MSN density

MSN density was determined by mercury intrusion porosimetry (Pascal 140/440, Porotec). Pressures ranging from 0.01 MPa to 400 MPa were used during the test.

3.2.4.5 Characterization of Nanofillers morphology

The morphology and size of the native and partially dissolved nanofillers were analyzed by scanning electron microscopy (SEM) using an ESEM Quanta 400 FEG instrument operating in a high vacuum. All samples were sputtered by a few nanometer gold film for better image resolution. Moreover, transmission electron microscopy (TEM) images were obtained using a Jeol JEM-2200FS system at an acceleration voltage of 200 kV.

3.2.4.6 Surface chemistry of the nanofillers

The functional groups characteristic for unfunctionalized and OTS functionalized MSN were detected using attenuated total reflection Fourier transform infrared (ATR-FTIR) spectroscopy. A Nicolet 4700 (Thermo Electron Corporation) system with a multi-reflection smart performer

ATR accessory was employed. The spectra were measured from 500 to 4000 cm^{-1} with 64 scans at a 2.0 cm^{-1} resolution.

3.2.4.7 Thermogravimetric analysis

The organic content (OC) after functionalization was determined by thermogravimetric analysis (TGA) using a STA 449 F1 (NETZSCH). The samples were heated at 3°C/min in oxygen up to 1000 °C. Number of the alkyl group of OTS molecules (N_{OTS}) per square nanometer was calculated with respect to the surface area of the unfunctionalized MSN (after CTAB removal) in case of HMSN and as-synthesized MSN (before CTAB removal) in case of LMSN, considering the respective size of groups using **Equation 3.2**.

$$N_{OTS} = \frac{n_A \times N_A}{S}$$

Equation 3.2: Calculation of number of grafted OTS molecules per nm^2

Where N_A is Avogadro's constant, S is the corresponding surface area of the used quantity of silica in TGA measurement per nm^2 and n_A is the number of OTS moles which can be calculated according to **Equation 3.3**.

$$n_A = \frac{OC\% \times m_{200}}{M_{CH}}$$

Equation 3.3: Calculation of number of OTS moles

where M_{CH} is the molecular weight of C18 chain of OTS; 255 g/mol, and OC% is the weight loss which is calculated from 200 to 600 °C that characterizes the amount of OTS grafted on the silica surface which can be calculated from **Equation 3.4**

$$OC\% = \frac{m_{200} - m_{600}}{m_{200}} \times 100$$

Equation 3.4: Calculation of weight loss %

where m_{200} and m_{600} were the residual weight of the sample at 200 °C and 600 °C in the TGA analysis, respectively.

The surface area (S) (nm^2) can be given by **Equation 3.5**:

$$S = m_{SiO_2} \times S_{BET-SiO_2} \times 10^{18}$$

Equation 3.5: Calculation of surface area

m_{SiO_2} is the mass of SiO_2 in LMSN or HMSN samples and can be calculated from **Equation 3.6**.

$$m_{SiO_2} = m_{200} - (n_A \times M_{OTS})$$

Equation 3.6: Calculation of the mass of SiO_2

Where, M_{OTS} is the group molecular weight of grafted OTS on the silica surface. It was calculated for monodentate, bidentate, and tridentate structure to be 317, 300, 283 g/mol,

respectively. Monodentate, bidentate, tridentate structure means that the hydrolyzed OTS can react with silica via one, two or three OH groups respectively. To simplify the calculation, bidentate structure was taken. The number of molecules/nm² in case of MTS was calculated by applying the previous equations for OTS

3.3 Membrane preparation and characterization

3.3.1 Preparation of PES support membrane

The flat sheet PES support membrane was prepared by vapor induced phase separation (VIPS) process, using the same procedure as reported in the casting solution was prepared by mixing 32 wt% NMP and 43.5 wt% TEG; then 12 wt% PVP was dissolved in this mixture. Thereafter 12.5 wt% PES was added to the solution. It was kept under continuous stirring (60 r.p.m) at room temperature until a clear and homogeneous solution was obtained. The solution was then cast using the casting machine (**Figure 3.2**) with a casting knife with 300 μm gap width and a casting speed of 5 mm/s. The cast film was directly moved to a controlled humid air chamber (relative humidity RH \approx 80% at about 23 °C) for 3 minutes. The semi-coagulated film was then moved to DI water coagulation bath (cf. **Figure 3.2**) and completely immersed for 12 h to completely removing the solvents.

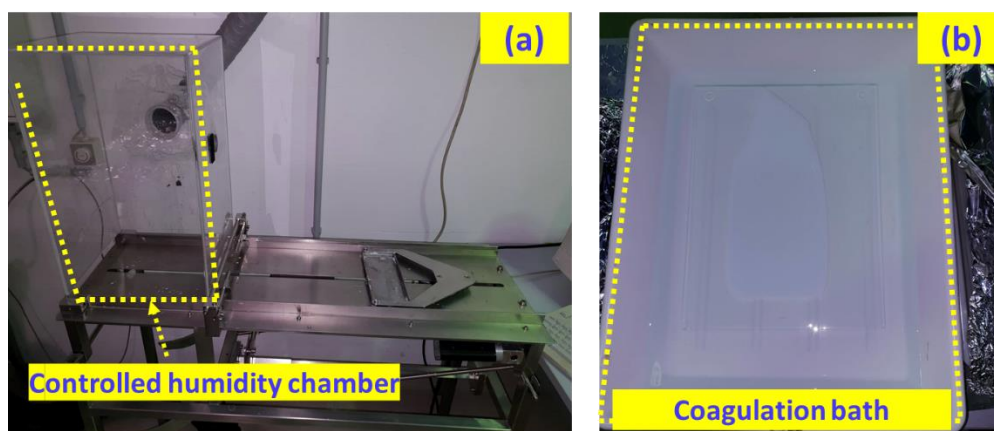


Figure 3.2: Image of (a) computer-controlled casting machine, and (b) coagulation bath

3.3.2 Preparation of TFC and TFN membranes

Both aromatic PA TFC and TFN membranes were prepared via IP of MPD and TMC on the surface of the support PES membrane, which prepared as described in (**Section 3.3.1**). The MPD and TMC concentrations were selected based on many literature [81,95,197] In case of TFN membranes, an additional step to deposit the NPs on the monomer-soaked support membrane prior to the IP reaction had been proposed, and this was also used here. The detailed preparation procedures are presented in **Figure 3.3**.

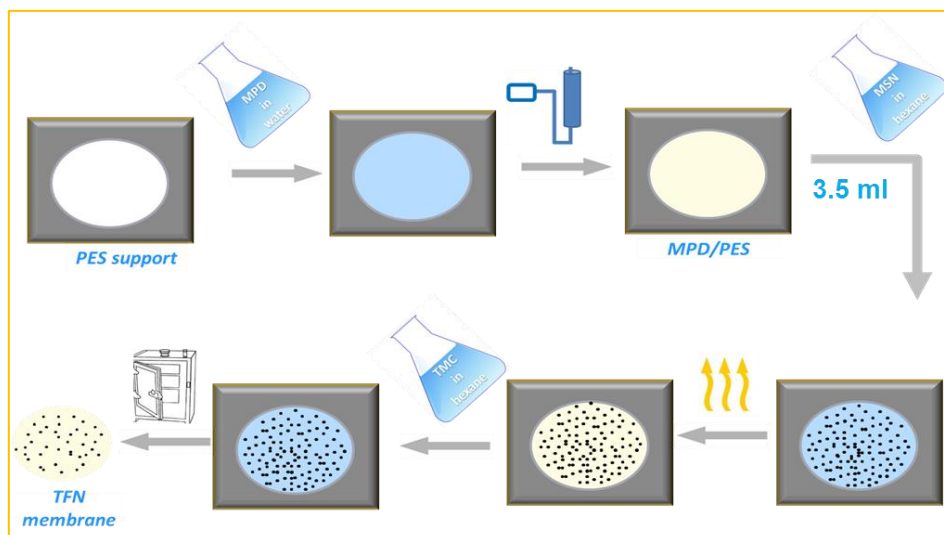


Figure 3.3: Schematic diagram for PA TFN membrane preparation

A circular shaped PES membrane (50 mm diameter) was cut from the big flat sheet. The PES membrane was immersed in DI water overnight, then removed and positioned on a glass plate. Another glass plate containing a hole with a diameter of 48 mm was placed on top of the membrane (**Figure 3.4**). Between the two glass plates, a Teflon sheet (1 mm thickness) with a hole diameter of 46 mm was used to fix the membrane. The membrane-glass plate-Teflon sandwich was hold together using two binder clips. 10 ml of 2 w/v% aqueous MPD solution were poured into the hole and allowed to contact the membrane for 10 min before draining the excess MPD solution. This time is essential to saturate the PES surface and near-surface pores with MPD solution. The excess MPD solution on the top surface of PES membrane was removed by rolling a rubber roller (cf. **Figure 3.4**) across the membrane surface for one time. Afterwards, 3.5 ml of MSN dispersed in n-hexane with different concentration ranging from 0.003 to 0.05 w/v % was added. The n-hexane solution was left to completely evaporate without any external effect; that needed about 30 min. Subsequently 10 ml of 0.1 w/v% TMC in n-hexane solution were gently added to contact with the membrane surface for 1 min. The excess solution was poured off. The obtained membranes were rinsed with n-hexane and allowed to dry at ambient conditions for 10 minutes before curing in the oven at 110 °C for 3 min [97]. Finally, the resulting membranes were immersed in DI water and kept in the fridge until use. TFC membranes were prepared using the same procedures used in preparation of TFN membranes just without addition of NPs.

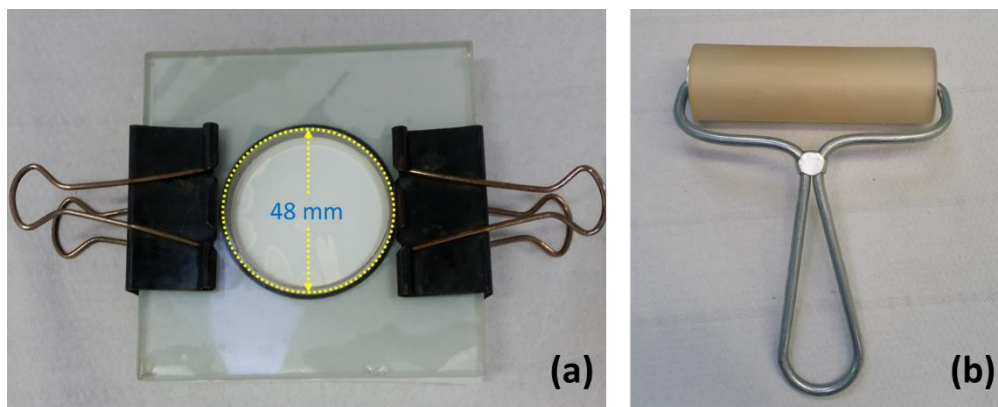


Figure 3.4: Illustration of (a) the glass module, and (b) the rubber roller used in PA preparation

3.3.3 Characterization of membranes

3.3.3.1 The membrane surface chemistry

The surface chemistry of TFC and TFN membranes was characterized using ATR-FTIR spectroscopy (cf. **Section 3.2.4**).

3.3.3.2 The membrane surface charge

In order to measure the surface charge of TFC and TFN membranes, zeta potential of the membranes was measured using SurPASS electro-kinetic analyzer (Anton-Paar). An adjustable gap cell, set at 100 μm , was used, and the measurements were conducted in a 1 mM KCl solution in Milli-Q water. 0.1 M HCl and 0.1 M NaOH solutions were used to adjust the pH values for potentiometric titrations. Prior to measurement, the membrane sample was rinsed twice with Milli-Q water for 480 s at pressure of 400 mbar, followed by rinsing in 1 mM KCl. Afterward, the streaming current was measured. The measurements started at around pH 10 and then the pH was decreased step-wise by the addition of HCl solution. The zeta potential data at different pH values were calculated according to Helmholtz–Smoluchowski equation (**Equation 3.7**) [198].

$$\zeta = \frac{dl}{dp} \times \frac{\eta}{\epsilon_0 \times \epsilon} \times \frac{L}{A}$$

Equation 3.7: Helmholtz-Smoluchowski equation

Where, ζ is zeta potential, dl/dp is slope of streaming current vs. differential pressure, η is the electrolyte viscosity, ϵ_0 is electrical permittivity vacuum, ϵ is dielectric coefficient of the electrolyte, also known as “relative permittivity”, L is length of the streaming channel, and A is the cross section of the streaming channel.

3.3.3.3 The membrane surface hydrophilicity

The hydrophilicity/hydrophobicity of the membranes was evaluated by measuring the contact angle (CA) of water using an optical goniometer (OCA 15 Plus; Dataphysics). The CA was measured by sessile drop method. The Milli-Q water drop volume was 5 μL and the Young-Laplace fitting was used. The measurements were repeated at least six times at different sites of the membrane, and the average and standard deviation were taken to obtain the CA for each membrane sample. CA data were obtained for all membranes by extrapolating to time zero and for selected membranes the change of contact angle with time was recorded over longer time periods.

3.3.3.4 The membrane surface and cross section morphology

The membranes' top surface and cross section morphologies were scanned using SEM (cf. **Section 3.2.4**). For cross section analysis, the membranes were broken in liquid nitrogen and both membranes' outer surface and cross section were coated with platinum at 20 mA for 1 min using a sputter coater (K-550, Emitech Ltd., Kent, UK).

3.4 Evaluation of membrane performance

3.4.1 Evaluation of pure water and pure ethanol permeabilities

The pure water permeability of all TFC and TFN membranes was determined using the dead-end nanofiltration stainless steel cell (**Figure 3.5**). A circular membrane (48 mm) was put on the cell and the cell reservoir (100 ml) was filled with Milli-Q water and allowed to be filtrated through the membrane at an operating pressure of 12-15 bar and at room temperature. The permeate water was then collected and the pure water permeability was calculated according to **Equation 3.8**.

$$\text{Pure liquid permeability} = \frac{m}{\rho t A \Delta P}$$

Equation 3.8: Pure liquid permeability

Where, m is the permeate weight (g), ρ is the liquid density (g/L), A is the membrane area (m^2), t is the filtration time (h), ΔP is the applied pressure difference across the membrane. The calculated data represent the average of three measurements from three different samples for the same membrane type.

Pure ethanol permeability was measured also using the same dead-end filtration system. But first the membranes were immersed in ethanol for about 5 minutes then moved to the filtration cell and the pure ethanol permeability was measured at the same operation pressure.



Figure 3.5: Dead-end filtration cell

3.4.2 Evaluation of initial separation performance

The initial separation performance of all membranes was assessed in terms of water permeance and salt rejection using the same dead-end filtration cell described in the **Section 3.4.1**. For that purpose, 2000 mg/L NaCl in Milli-Q water was used as feed solution that fill the cell and also tested under the operation pressure (12- 15 bar) at ambient temperature and stirring rate of 700 rpm.

The solution permeability was measured and expressed as permeance according to **Equation 3.9**:

$$\text{Permeance} = \frac{m}{\rho t A (\Delta P - \Delta \pi)}$$

Equation 3.9: Calculation of permeance under RO conditions

Where, ΔP is the applied pressure difference across the membrane and $\Delta \pi$ is the osmotic pressure difference across the membrane (bar). The osmotic pressure for a salt solution at moderate concentrations is described by the Van't Hoff's equation according to **Equation 2.4** (cf. **Section 2.3.5.1**). The salt rejection was calculated by measuring the conductivity of permeate and feed samples by using a conductometer (856 Conductivity Module, Metrohm) according to **Equation 2.5** (cf. **Section 2.3.5.1**)

3.4.3 Evaluation of long-term membrane stability

The stability of desalination performance of all TFC and TFN membranes was evaluated via a long-term filtration experiment using a cross-flow lab-scale membrane testing unit (P-28; FOLEX AG, Seewen, Switzerland (**Figure 3.6**)). The effective membrane area was 28 cm². All membranes were first compacted with DI water for at least 5 h at 20 bars until they reached a

stable water permeance. The system was then operated with 2000 ppm NaCl feed solution at natural pH, and the initial permeance and salt rejection were checked under an applied pressure of 16 bars and the temperature of the feed was controlled at 25 °C. In order to study the influence of nanofillers dissolution on the membrane stability, the filtration was carried out at two different pH values, pH 5 and pH 9 using HCl and NaOH, respectively. First, the feed tank of the filtration cell was filled with feed solution at pH 5 and the filtration started. After 20 minutes, a specific volume of the permeate was collected for analysis in terms of permeance and salt rejection. The filtration was continued until collecting about 450 ml of permeate and the rest of feed solution was disposed of to avoid the filtration of the too high salty water. Then the filtration cell was cleaned with Milli-Q water adjusted at the same pH before recharging the feed tank again with the next 500 ml feed solution. The filtration at pH 5 was carried out over 120 h, then the filtration of the feed solution at pH 9 was carried out for additional 120 h as described before.



Figure 3.6: Cross-flow filtration cell

3.4.4 Evaluation of barrier layer durability of the pre-tested membranes

To evaluate the influence of nanofillers dissolution on the durability of the membrane barrier layer, five different dextran (4 kDa, 35 kDa, 100 kDa, 200 kDa and 2000 kDa) solutions (1 g/L for each) were allowed to be filtrated through the membrane after the desalination experiment for 240 h. The filtration was started with the solution of dextran (4 kDa), then larger dextran solutions were filtrated next. Both feed and permeate were analyzed using total organic carbon analyzer (TOC-V CPH/CPN) and the rejection was determined using **Equation 2.5**.

Chapter 4

4. Results and discussion

4.1 Development of MSN nanofillers

Optimizing the properties of the nanofillers has a great influence on the separation performance of the TFN membranes which specifies the application of the membrane. The downside of MSN nanofillers for preparation of TFN membranes is their tendency to aggregation in the organic solvent during membrane preparation (cf. **Section 2.5.4.**).

In this section preparation of MSN with controlled particle diameter and controlled functionalization will be presented.

4.1.1 Preparation of the base MSN

The schematic representation for the preparation of MSN is provided in **Figure 4.1**. The CTAB surfactant, which forms micelles under the synthesis conditions was used as a template during the preparation of MSN via a sol-gel process with the TEOS as a silica source.

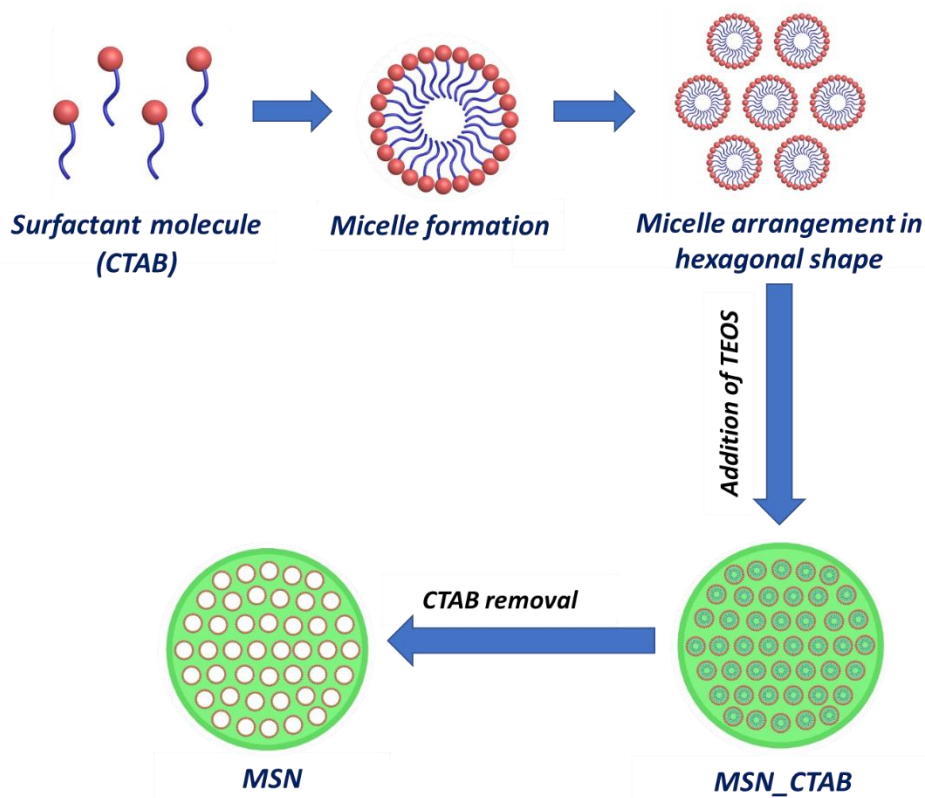


Figure 4.1: Schematic preparation of MSN via sol-gel process

4.1.1.1 Control of MSN particle size

The particle size of MSN was controlled by optimizing the molar ratio (R) of surfactant and silica precursor (CTAB/TEOS) during the particles formation. The CTAB/TEOS molar ratio

was adjusted by selecting different concentrations of surfactant, ~ 1 mM to ~ 10 mM, and a fixed concentration of TEOS (~ 28 mM).

The SEM micrographs (**Figure 4.2**) show agglomeration of irregular shape particles which were synthesized at low molar ratio ($R = 0.018$), and the particles take spherical shapes with increasing the molar ratio ($R = 0.035 - 0.18$). Furthermore, a clear trend toward smaller particle size at higher CTAB/TEOS ratio is observed. The agglomeration of the particles at the low CTAB/TEOS molar ratio was also confirmed by TEM at **Figure 4.3**. As shown in the figure, hexagonal and ordered mesoporous structure of the synthesized NPs, which is distinctive for MSN, was clearly detected.

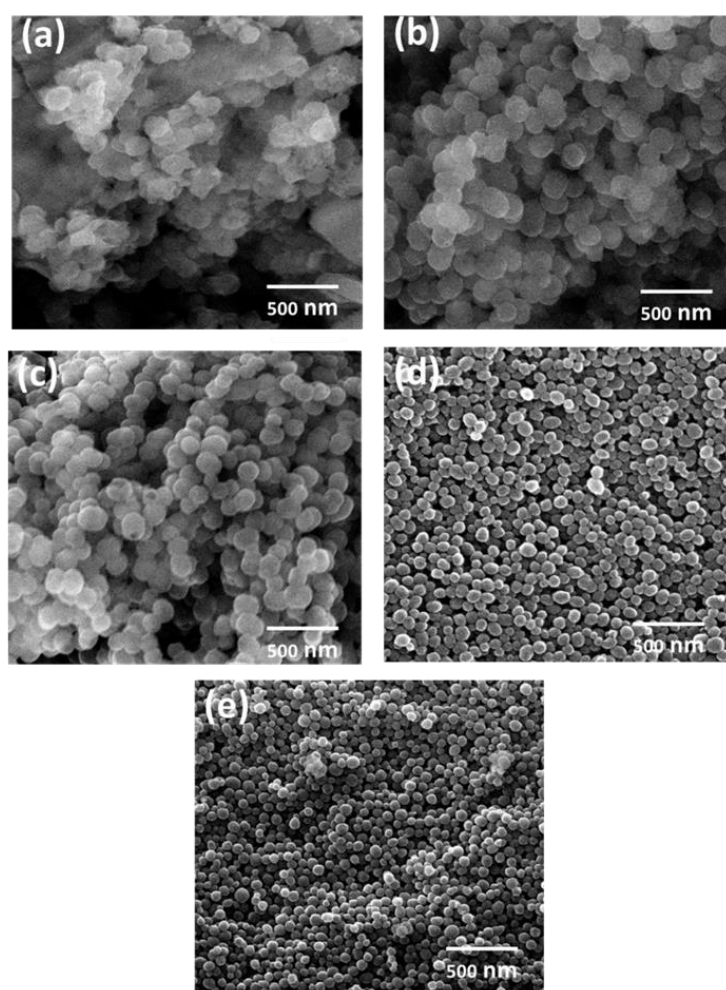


Figure 4.2: SEM images of MSN obtained at different CTAB/TEOS molar ratios: a) 0.018, b) 0.035, c) 0.054, d) 0.1 and e) 0.18.

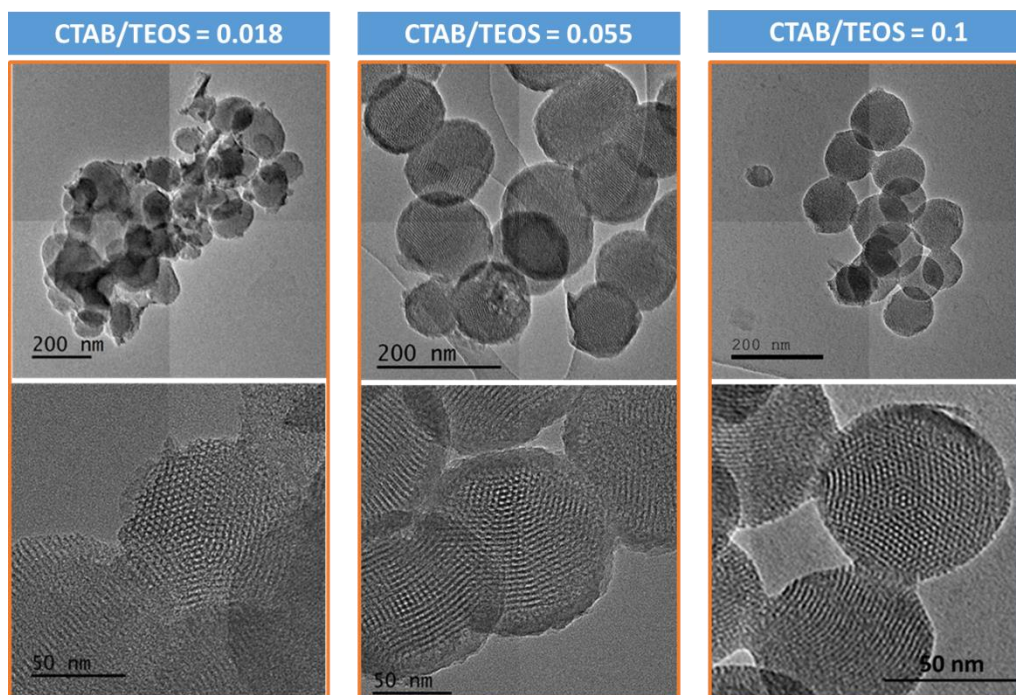


Figure 4.3: TEM micrograph of MSN prepared with different CTAB/TEOS molar ratio

At low molar ratio of CTAB to TEOS, some of positively charged surfactant molecules interact with the high negative charge silicate ions formed after hydrolysis of TEOS, thus producing nuclei of the mesostructured material. However, because CTAB exists only in low quantity, it was consumed rapidly so that the mesoporous structure was formed, but the excess of TEOS could form nonporous silica on the surface of the resulting particles. This is because the surfactant concentration was very near to the critical micelle concentration (CMC) of CTAB in water which was reported to be 0.7 to 0.94 mM according to [199]. On the other hand, with increasing the CTAB concentration, ($R = 0.035 - 0.18$), the micelles concentration also increased which improved the dispersity of TEOS in the water. As a result, the hydrolysis of TEOS proceeded more rapidly leading to increasing nucleation rate. Therefore, the particle diameter of the obtained MSN decreased [171].

The results of DLS measurements of MSN dispersions (**Table 4.1**) showed that the particle diameters of the different MSN samples were always larger than diameters calculated from SEM, due to the hydrated layer in aqueous solution. The MSN sample obtained at highest CTAB/TEOS molar ratio ($R = 0.18$) revealed the lowest particle diameter according to the previous explanations. However, the polydispersity index (PDI) measured by DLS is quite high indicating a wider particle size distribution, especially if compared with the sample obtained at $R = 0.1$. Consequently, according to both SEM and DLS results and with view on the intended

integration of as nanofiller in polyamide layers of about 100 nm thickness, MSN with $R = 0.1$ with a diameter of about 80 nm were considered to be best suited for all further experiments.

Table 4-1: Particle size of synthesized MSN from analysis of SEM images and DLS measurements of aqueous dispersions depending on the molar ratio of CTAB to TEOS

No	CTAB/TEOS molar ratio (R)	SEM	DLS	
			d (nm)	PDI
1	0.018	-	267 ± 123	0.58
2	0.035	152 ± 18	350 ± 70	0.33
3	0.055	109 ± 16	155 ± 35	0.42
4	0.1	80 ± 14	116 ± 20	0.24
5	0.18	66 ± 16	107 ± 35	0.73

The small-angle XRD patterns obtained for these spherical NPs are presented in **Figure 4.4 (a)**. The XRD data revealed four characteristic peaks at 2θ of 2.2° , 3.8° , 4.3° and 5.7° representing the (100), (110), (200) and (210) planes, respectively. This structure is consistent with the hexagonal lattice symmetry of MCM-41 [200,201]. The d-spacing at the reflection plane 100 appearing at $2\theta = 2.2^\circ$ was calculated using Bragg's equation (**Equation 4.1**):

$$\lambda = 2d \sin\theta$$

Equation 4.1: Bragg's equation

where λ is the wavelength of CuK α radiation ($\lambda = 1.54 \text{ \AA}$). Therefore, d_{100} was estimated to be 4.0 nm. The unit cell (a_0) which is the repeat distance between two pore centres in MSN was calculated from **Equation 4.2**.

$$a_0 = (2/\sqrt{3}) d_{100}$$

Equation 4.2: Calculation of the unit cell

It was estimated to be 4.6 nm. Finally, the pore diameter was then calculated by subtracting the thickness of pore wall (ca. 1 nm as discussed in [191]) from a_0 and yielded a value of 3.6 nm.

The nitrogen adsorption isotherm at 77 K and the corresponding DFT pore size distribution of MSN are shown in **Figure 4.4 (b)**. The observed adsorption data for MSN displayed a typical "type IV" isotherm with a sharp capillary condensation step in the medium range of the relative pressure. The obtained isotherm is characteristic for mesoporous materials with uniform pore size distribution. Overall, the produced MSN had an average pore diameter of 3.3 nm (estimated by DFT as presented in **Figure 4.4 (b) inset**), a pore volume of $0.87 \text{ cm}^3 \text{ g}^{-1}$ (up to relative pressure of 0.99) and a specific surface area of $920 \text{ m}^2 \text{ g}^{-1}$ (BET).

The results for MSN pore size using the two different methods are in a good agreement, and close to published data in literature (pore diameter calculated from XRD data was 3.85 nm [17] and the pore size estimated from nitrogen adsorption and DFT was 3.5 nm [202]).

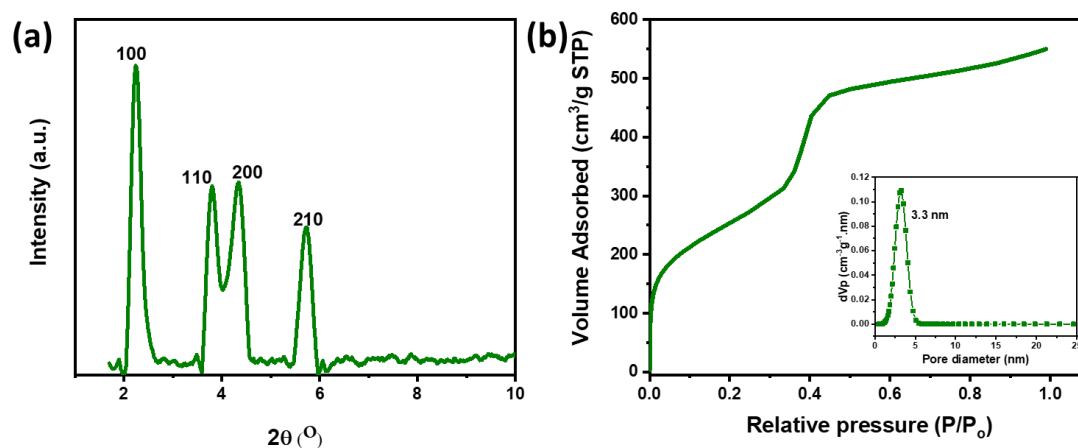


Figure 4.4: (a) small angle XRD for MSN and (b) nitrogen adsorption isotherm at standard temperature and pressure (STP) as well as estimated pore size distribution (inset) of MSN.

4.1.1.2 Surfactant removal

The surfactant was removed by two methods, i.e. calcination at high temperature or extraction in a mixture of methanol and hydrochloric acid (HCl). FTIR spectroscopy (**Figure 4.5 (a)**) was used to confirm the complete removal of surfactant from the as-synthesized MSN. The results revealed that the peaks at 2922 cm^{-1} and 2854 cm^{-1} , which are attributed to aliphatic C-H group stretching mode of CTAB [203], completely disappeared in case of calcination at $600\text{ }^{\circ}\text{C}$. In case of solvent extracted MSN, on the other hand, small peaks were still observed in this region of the spectrum. This was probably due to the presence of some traces of surfactant molecules that were not removed by solvent extraction. This was also supported by TGA analysis, where the weight loss was measured in the range of $25\text{ }^{\circ}\text{C}$ – $1000\text{ }^{\circ}\text{C}$ (**Figure 4.5 (b)**). The weight loss before $200\text{ }^{\circ}\text{C}$ was attributed to the removal of adsorbed water and any remaining organic solvents may exist on silica surface. The weight loss from $200\text{ }^{\circ}\text{C}$ to $600\text{ }^{\circ}\text{C}$ could be related to the decomposition of CTAB. Consequently, the residual amount of surfactant for both calcinated and solvent extracted prepared MSN could be estimated, which was found to be $\approx 4\%$ and 1% , respectively (according to TGA, as synthesized MSN contained 46.5% CTAB). Above $600\text{ }^{\circ}\text{C}$, there was $\approx 1\%$ weight loss for both solvent extracted and calcinated MSN which could be due to the water loss as a result of condensation of silanol groups to form siloxane bonds [204]. Accordingly, because only a very minor CTAB residual

was left and the procedure was easier to perform, solvent extraction was employed to remove the surfactant instead of calcination in high temperature to control the OTS functionalization.

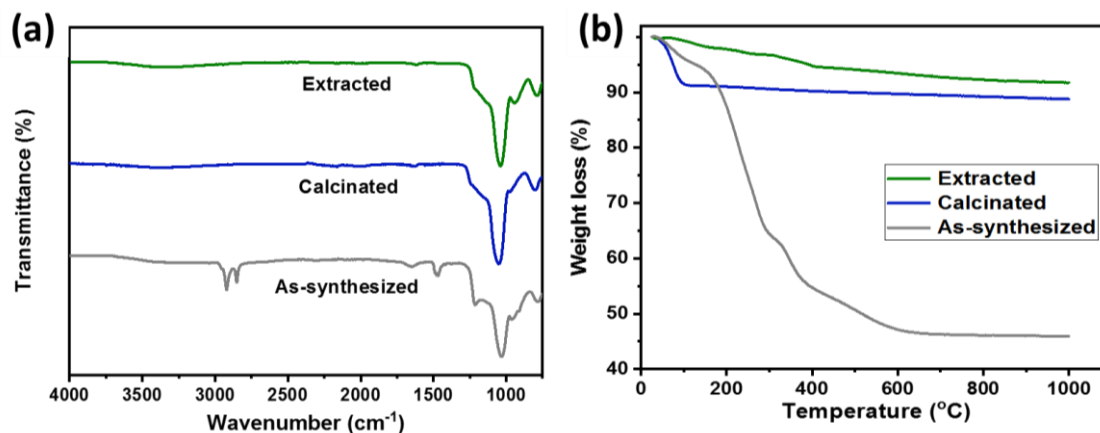


Figure 4.5: (a) FTIR spectra and (b) TGA of as-synthesized, calcinated and solvent-extracted MSN

4.1.2 Surface functionalization of MSN

Due to the hydrophilic nature of the silanol (Si-OH) terminated MSN, achieving a good dispersion of these NPs in organic solvents (such as n-hexane) during the membrane preparation is challenging. Accordingly, the functionalization process of the prepared MSN particles was necessary. OTS-functionalized MSN were found to show better dispersion in n-hexane than the unfunctionalized MSN even without any sonication as can be seen in **Figure 4.6**.

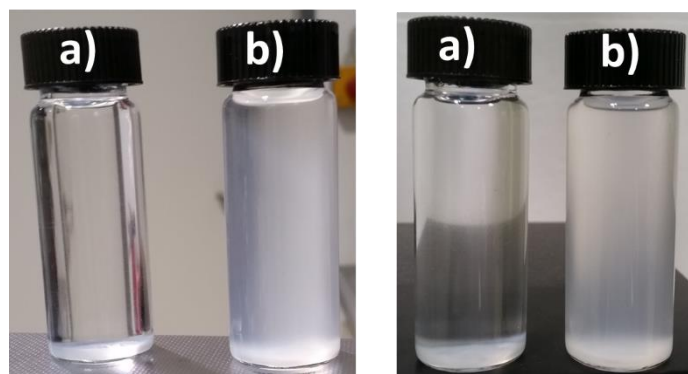


Figure 4.6: Dispersibility of (a) unfunctionalized MSN and (b) OTS-functionalized MSN in n-hexane; left: Image just after shaking the bottles; right: image after 30 minutes of sonication

4.1.2.1 Controlled OTS-functionalization of MSN

Unlike nonporous silica, MSN have two different surfaces, the external surface and the internal pores surface. Lim and Stein reported that the external surface is more accessible and easy to be functionalized compared to the internal mesopores surface [189]. Nevertheless, the internal surface of the pores can also be functionalized due to the high chemical reactivity of

the trichloro silane. In addition, considering the MSN pore size (3.3 nm), such relatively large pore space could allow to be grafted with the linear aliphatic molecule OTS, as can be seen in the schematic illustration in **Figure 4.7**.

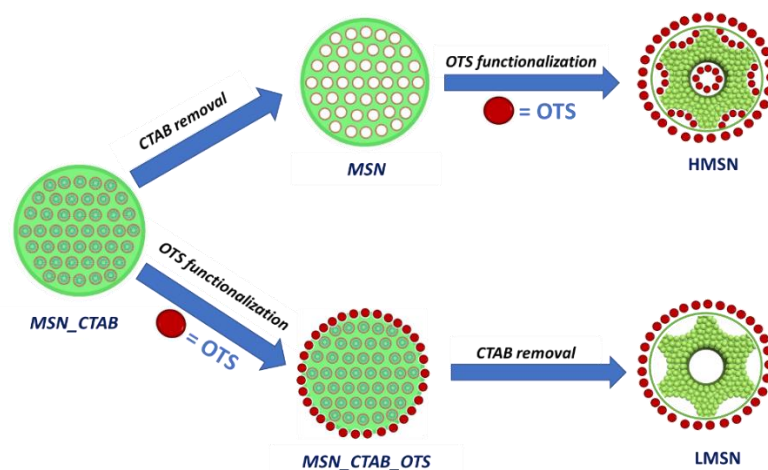


Figure 4.7: Schematic representation for the surface functionalization of MSN (OTS grafting inside the pores leads to their water “hating” character: HMSN; preventing OTS grafting inside the pores leads to water “loving” character: LMSN)

4.1.2.2 Characterization of the functionalized NPs

The FTIR spectra of both LMSN and HMSN (**Figure 4.8**) showed two peaks at 2920 and 2852 cm^{-1} , which are assigned to the stretching vibration of C-H group. Since OTS is an organosilane coupling agent with a C18 chain, the C-H group stretching bands are reasonably due to the CH_2 groups of the long alkyl chain. The results provide an evidence to support the successful OTS functionalization on the MSN surface. The intensity of the peaks in FTIR spectra is largely influenced by the grafted OTS amount on the NPs. First of all, in both series an influence of OTS concentration was observed, significantly lower intensities were observed after using an OTS/MSN ratio of 0.5 (w/w) compared to data for OTS/MSN ratio of 1 (w/w) or higher. In case of HMSN, both external and internal pores surfaces were prone to the OTS functionalization, therefore larger amounts of OTS could be grafted. On the other hand, in case of LMSN, the OTS functionalization occurred almost only on the external surface of the NPs because the pores of MSN were filled with surfactant during functionalization step which could restrict the incorporation of OTS inside the pores surface. As a result, the peak intensity observed after identical functionalization conditions is much lower in case of LMSN than HMSN.

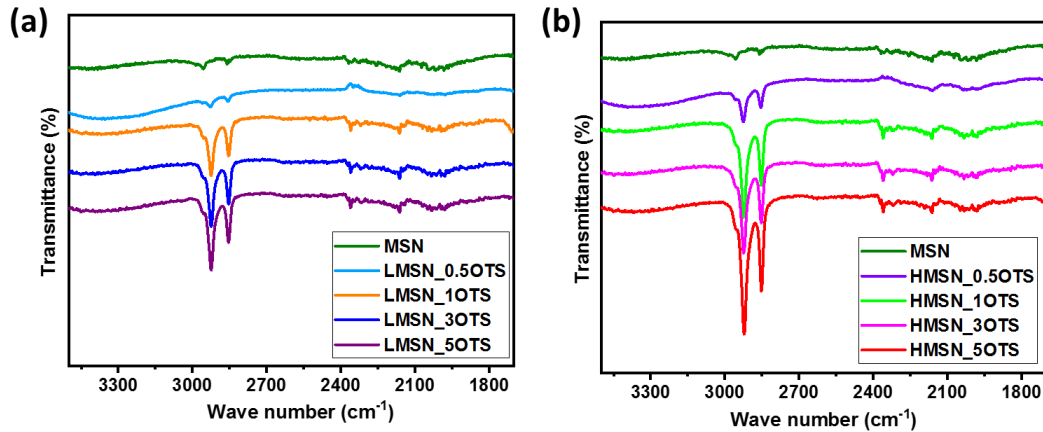


Figure 4.8: FTIR spectra for a) LMSN, b) HMSN, each obtained at different concentration of OTS (OTS/MSN ratio = 0.5 - 5 w/w) during the functionalization

Thermogravimetric analysis was additionally used to evaluate the thermal stability of the functionalized MSN and to estimate the amount of OTS grafted to MSN. As can be noticed in **Figure 4.9**, the weight loss for LMSN was always lower than the weight loss for HMSN, confirming that LMSN consumed lower quantity of OTS because the functionalization occurred only on the external surface and was not extended to the interior pores surfaces like for HMSN.

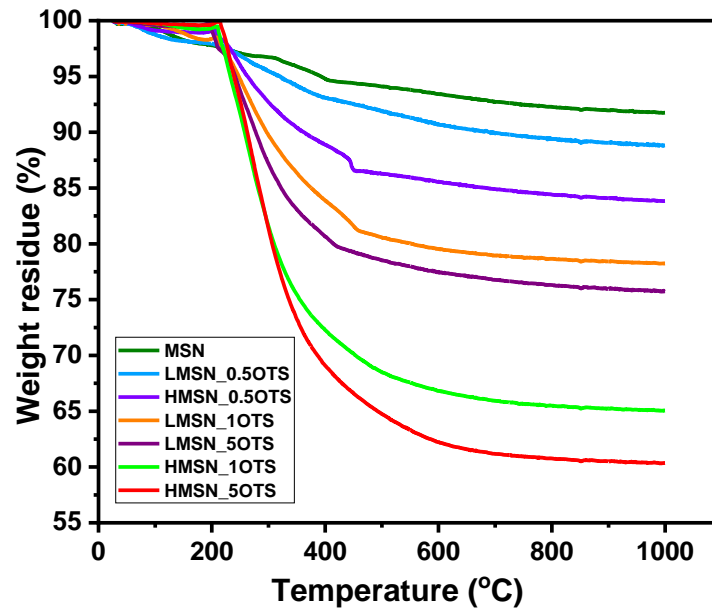


Figure 4.9: Thermogravimetric analysis of unfunctionalized MSN and functionalized LMSN and HMSN with different OTS content

The weight loss between 200 and 1000 °C was utilized to calculate the number of OTS molecules grafted on the surface per square nanometers (N) which can be estimated from TGA measurement according to the **Equation 3.2** in **Section 3.2.4.7** and the results are presented in **Table 4.2**.

As one can see, in case of LMSN, N_{OTS} was higher than in case of HMSN, under the assumption that grafting for LMSN is only possible on the outer particle surface while for HMSN the entire specific surface area is accessible. Tidswell et al. [205] reported that the area per one molecule is 0.22 nm^2 for OTS in a well-ordered monolayer on a flat SiO_2 surface; N_{OTS} can be estimated accordingly to be $4.5 \text{ molecules/nm}^2$. In case of LMSN, the calculated N_{OTS} after using higher OTS concentrations, i.e. 1 and 5 w/w, was $3.8 \text{ molecules/nm}^2$ and $4.5 \text{ molecules/nm}^2$, respectively, suggesting the formation of well-ordered monolayers on the outer particle surface. The value of $N_{OTS} = 1.45 \text{ molecules/nm}^2$ for 0.5 (w/w) OTS indicated an incomplete, deformed monolayer on the silica surface. On the other hand, in case of HMSN, the data for N_{OTS} were all below the value for a monolayer on both the external and the internal pore surface for all OTS concentrations. This can be explained by the fact that the MSN pore diameter of 3.3 nm imposed major hindrance for the formation of a well-ordered monolayer inside the pores because such layer (on a planar surface) has a thickness of 2.4 nm [205]. Nevertheless, all data clearly indicate that also the interior of the pores is modified by OTS, but in a disordered fashion leading to a much thinner hydrophobic organic layer.

Table 4-2: Organic content and estimated surface density of OTS for LMSN and HMSN

Sample	OTS concentration [#] (w/w)	OC (wt%)	N_{OTS} (molecules / nm^2)
LMSN [*]	0.5	8.3	1.45
	1	19.0	3.8
	5	21.5	4.5
HMSN [§]	0.5	13.4	0.4
	1	32.5	1.35
	5	37.5	1.7

[#] OTS/MSN ratio used for functionalization

^{*} The surface area which had been used to calculate N_{OTS} of LMSN is the surface area of as-synthesized MSN (before removing CTAB) = $149.5 \text{ m}^2/\text{g}$.

[§] The surface area which had been used to calculate N_{OTS} of HMSN is the surface area of MSN (after removing CTAB) = $920 \text{ m}^2/\text{g}$.

Nitrogen physisorption was employed to study the influence of OTS functionalization on the BET specific surface area, pore volume and pore size distribution of the MSN. Overall, OTS functionalization drastically affected the nitrogen adsorption isotherms (**Figure 4.10 (a)**).

According to the results summarized in **Table 4.3**, the specific surface area, pore volume and pore diameter of both LMSN and HMSN decreased with increasing of the grafted OTS amount, (cf. **Table 4.2**). In case of HMSN, both internal surface of the mesopores and external surface of the particle were accessible to be grafted with OTS molecules. The adsorbed nitrogen volume for HMSN decreased strongly with increasing OTS/MSN ratio during the functionalization, as shown in **Figure 4.10 (b)**; except for “HMSN_0.5OTS” the adsorption isotherm followed “type II” which is characteristic for nonporous materials. The change of isotherm from “type IV” to “type II” (more clearly seen in the “zoom in” part provided in **Figure 4.10 (c)**) could be due to the loss of mesoporous structure of MSN. Most likely a fraction of internal pores was blocked by the long alkyl chain OTS at the high concentration. The pore blocking explains the sharp decrease of BET surface area, pore diameter and total pore volume for MSN samples grafted with 1, 3 and 5 w/w OTS. This behavior is not as clear in case of MSN grafted with 0.5 w/w OTS; the resulting materials still have high BET surface area, pore diameter and total pore volume. Probably, the OTS/MSN ratio was insufficient to block the pores. It should be noted that irrespective of the large efforts to prevent such side reaction by controlling the reaction solutions and conditions, traces of water present during functionalization could lead to polysiloxane condensation in parallel to the intended grafting and as a result block the mesopores more effectively than end-on grafted C18 chains.

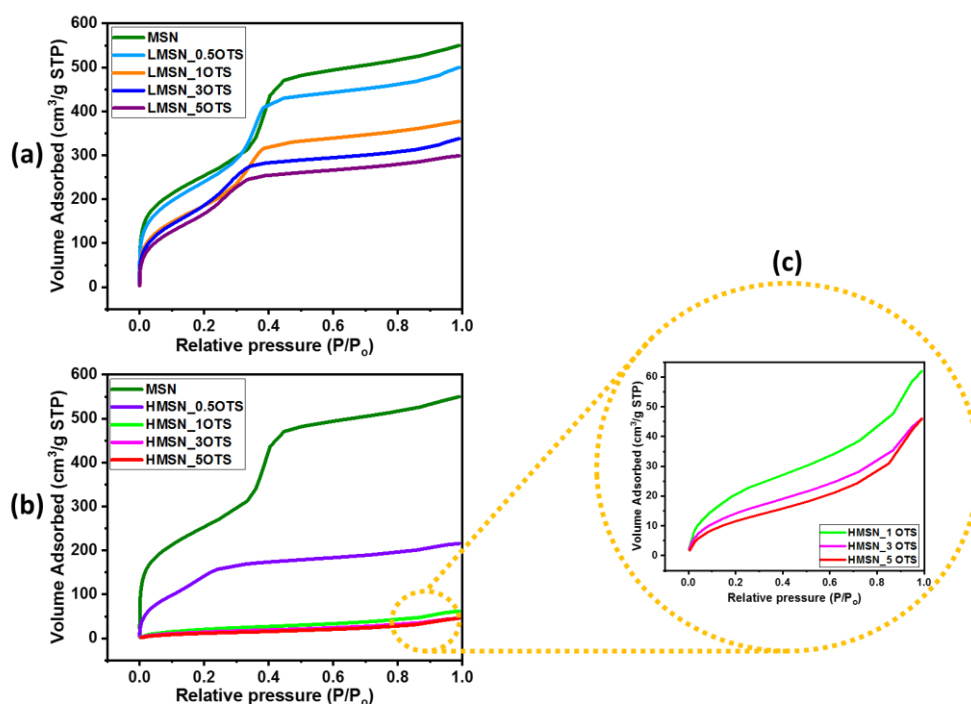


Figure 4.10: Nitrogen adsorption isotherms of (a) LMSN, (b) HMSN, obtained by using different OTS concentration, along with the data for unmodified MSN, and (c) Detailed view on nitrogen adsorption isotherms for HMSN

On the other hand, the adsorption data for all LMSN samples were identified as “type IV” isotherms, even at high concentration of OTS, suggesting that the external surface functionalization retains the mesoporous structure. However the slight decrease of BET surface area, pore diameter and total pore volume by increasing the efficiency of OTS functionalization (as presented in **Table 4.3**) could be interpreted by partially dissolving the surfactant (CTAB) in the organic solvent (toluene), thus allowing the OTS to enter mesopores and bind to the inner surface of MSN [206], but to a much lower extent than in case of HMSN preparation.

There are two suggested scenarios to explain the way of pore blocking in case of HMSN during the silanization reaction according to the schematic description in **Figure 4.11**. The first scenario is that the OTS molecules can truly enter the interior pores and fill them completely. Whereas the second scenario is that the OTS molecules can partially fill the internal pores and close the pore entrance by formation of a self assembled monolayer on the particle surface. According to **Table 4.3**, the BET C constant, which is related to the solid-adsorbate affinity [207], could be employed to account for the effects of OTS grafting inside the pores. The C constant decreased from 94 for the hydrophilic unfunctionalized MSN, that means high affinity for N₂ physisorption, to be in range of 44 - 55 for LMSN samples and 23 - 33 for HMSN samples. This decrease in the affinity toward N₂ physisorption by converting the surface from

hydrophilic to hydrophobic, may imply that the self assembled monolayer of OTS is formed on the external surface of both LMSN and HMSN. It means that this layer might block the pore entrance before completing the internal pore grafting thus acting as a pore mask during the nitrogen adsorption experiment (cf. **Figure 4.11**). This could explain the produced type II isotherm. Moreover, due to the long alkyl OTS chain, the complete grafting of the internal pores surface could also be complicated due to the strong steric hindrance. Therefore, the second scenario of pore blocking could be more valid than the first one.

Table 4-3: Overview on data for pore structure characterization for LMSN and HMSN obtained after functionalization at different OTS concentrations

OTS concentration (w/w)	BET surface area (m ² /g)		BET C constant		Pore diameter (nm)		Total pore volume (cm ³ /g)	
	LMSN	HMSN	LMSN	HMSN	LMSN	HMSN	LMSN	HMSN
0	920		95		3.3		0.837	
0.5	895	490	56.5	33	2.85	2.4	0.758	0.33
1	695	74	49	33	2.85	3.8	0.575	0.09
3	680	57	44	25.5	2.65	0.73	0.51	0.067
5	600	47	46	23.5	2.6	0.72	0.457	0.065

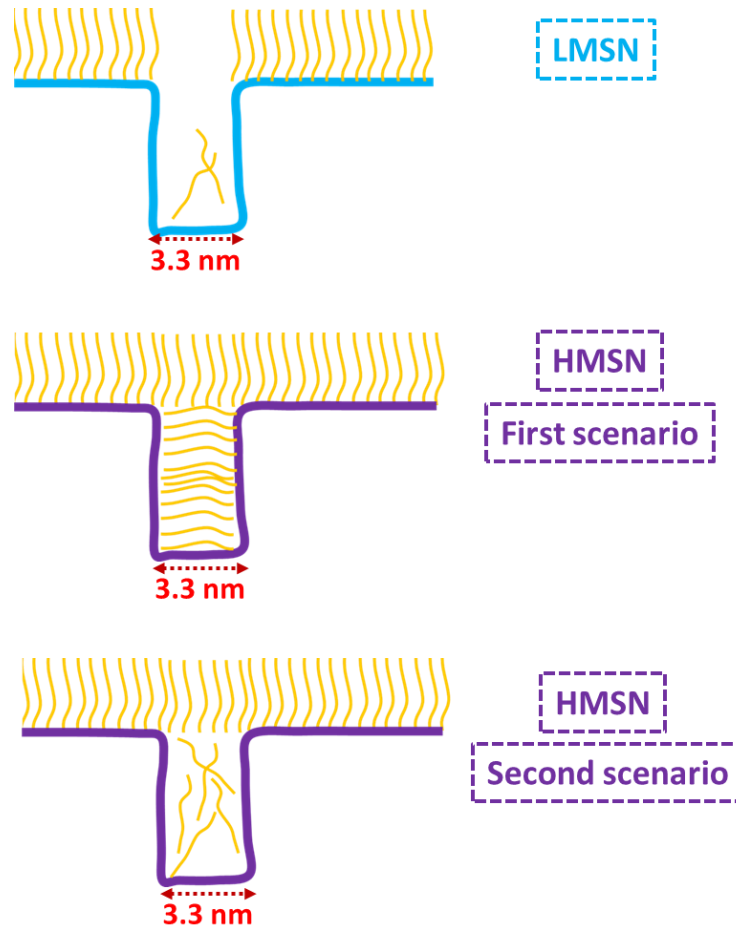


Figure 4.11: Scheme illustrating the two scenarios of pore blocking in HMSN in comparison with the opened pores in LMSN

It was important to measure the density of the functionalized and unfunctionalized samples. For that purpose, mercury intrusion porosimetry was employed. The measured density was 1.1 and 1.2 g/cm³ for LMSN and HMSN using 0.5 w/w OTS concentration, respectively, compared to 0.7 g/cm³ for the base MSN. The low density of all mesoporous silica samples, compared to the density of the amorphous silica (2.2 g/cm³), indicates to the high porosity because of the mesoporous structure which exceeded 68% for MSN. This value decreased after OTS functionalization to 50% for LMSN and 45% for HMSN, respectively. The small difference between the measured density of LMSN and HMSN is attributed to the low OTS concentration which was used for functionalization of the measured samples. The knowledge about the density was required not only for better understanding the influence of functionalization on the structure of MSN but also for estimating the deposited amount of the nanofillers onto the barrier layer of the TFN membranes as will be shown in **Section 4.2.3**.

4.2 TFN membrane preparation, characterization and initial performance evaluation

TFN membranes were prepared as described in **Section 3.3.2**, using a method where the NPs had been individually dispersed in n-hexane and deposited on the PES support membrane which before had been impregnated with the aqueous MPD solution; after evaporation of n-hexane, the TMC solution in n-hexane had been applied to start the IP reaction. The evaluation had first focussed on the characterization of the nanofillers incorporation into the membrane matrix (**Section 4.2.1**), then the effects of the kind of MSN functionalization on the separation performance (**Section 4.2.2**), thereafter –with the most promising MSN nanofillers– the effect of particles loading had been investigated (**Section 4.2.3**).

4.2.1 Characterization of TFN membranes

The impact of LMSN loading on the TFN membranes surface chemistry was studied by ATR FT-IR spectroscopy (**Figure 4.12**). In the spectra, several characteristic signatures were observed such as the bands at 1660 cm^{-1} characteristic of amide I (C=O stretching), 1540 cm^{-1} assigned to amide II (C-N stretching and N-H bending) and the vibrational band at 1610 cm^{-1} assigned to N-H stretching. These bands clearly proved that the polymerization had occurred [208,209]. The FTIR spectra not only revealed the bands ascribed to polyamide, but also those which are characteristic to the PES support membrane, because in the ATR mode the IR beam penetration depth (about $2\text{ }\mu\text{m}$) exceeds the thickness of the polyamide layer [138]. The typical bands which are characteristic for PES were clearly shown such as the vibrational bands at 1240 cm^{-1} and 1485 cm^{-1} assigned to (C-O) stretching and (CH₃-C-CH₃) stretching, respectively. The incorporation of MSN into the polyamide layer was also confirmed by the ATR FT-IR spectra. The characteristic bands of MSN are located at 1070 cm^{-1} attributed to Si-O-Si stretching, while vibration band of the Si-O-Si bond appeared at 455 cm^{-1} . Because LMSN with relatively low degree of OTS functionalization had been used (3.0 wt% organic content; cf. **Table 4.2**); the intensity of the characteristic bands for CH₂ had been too low for identification within the membrane (cf. **Figure 4.8 (a)**). However, both of above mentioned MSN signatures became stronger due to increase of NPs loading in the polyamide layer [210].

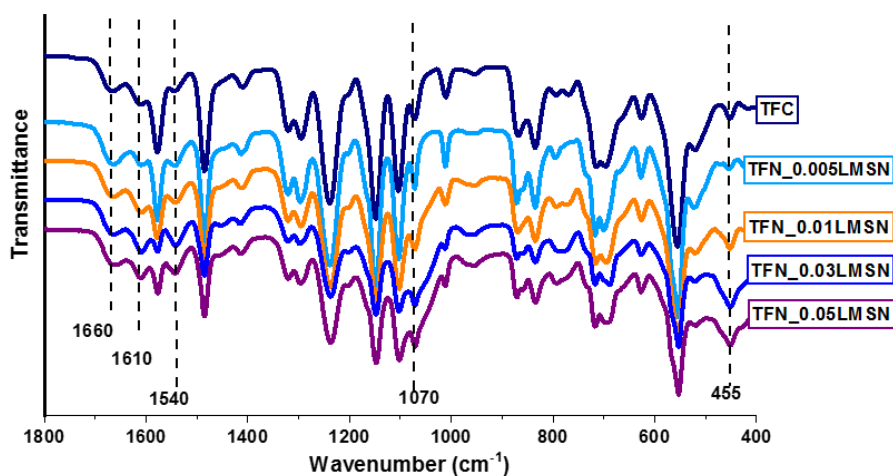


Figure 4.12: ATR FT-IR spectra of TFC and TFN membranes at different LMSN loading (functionalized with 0.5 w/w OTS)

Water contact angle measurements of TFC and TFN membranes obtained with LMSN or HMSN with different degree of OTS functionalization at the same NPs loading (0.01 w/v% filler concentration) revealed only minor differences (**Figure 4.13**). It could have been expected that increasing the OTS concentration during the functionalization may increase the membrane hydrophobicity. However, according to the obtained results, all TFN membranes with either LMSN or HMSN at the same nanoparticle loading revealed only a slight increase of contact angle (between 67° and 79°) compared to the reference TFC membrane (68°). This indicates that the OTS-based layer on the MSN surface has only a small effect on the wetting (surface energy) of the membranes. Therefore, it may conclude that most of the NPs are well covered with the polyamide layer; as the contact angle of TFN membranes was dominated by the surface properties of the polyamide.

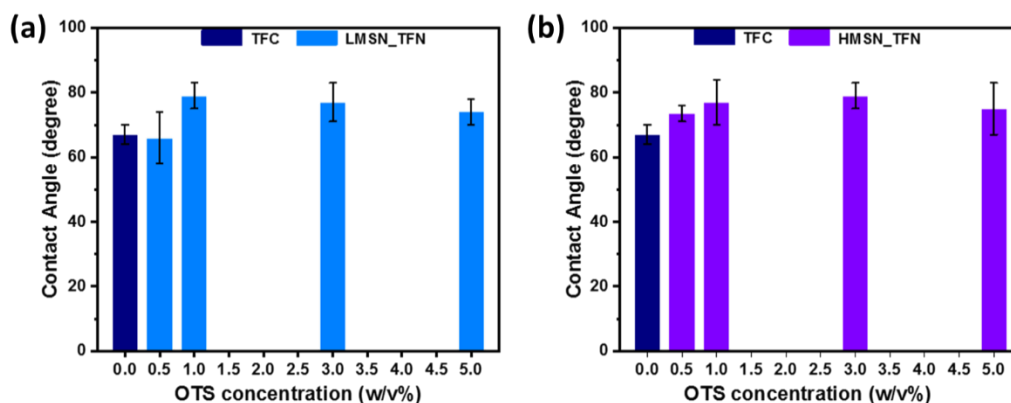


Figure 4.13: Effect of OTS concentration during MSN functionalization on the water contact angle of TFN membranes: a) with LMSN and b) with HMSN. The NPs loading in TFN membranes is 0.01 w/v%

The membrane surface charge for all TFC and LMSN_TFN and HMSN_TFN membranes functionalized with different amount of OTS are presented in **Figure 4.14**. In general all membranes revealed a negative charge due to presence of unreacted carboxylic groups on the surface of PA layer [12,68]. The nanofillers could affect the charge of PA layer if they are exposing the surface and not well covered with the PA, or they can reduce the degree of the polymer crosslinking which provide the membrane with the negative carboxylic groups and increase the overall surface negative charge. The NPs loading (0.01 w/V%), which was used for preparation of the characterized TFN membranes, produced PA layer containing well integrated nanofillers inside (as will be explained in **Section 4.2.3**). Therefore, the slight decrease in the isoelectric point of the TFN membranes (cf. **Figure 4.14**) could be attributed to the formation of low crosslinked PA layer because the insertion of the nanofillers. On the other hand, there is no significant change on the surface charge among the LMSN or HMSN functionalized with different OTS concentration.

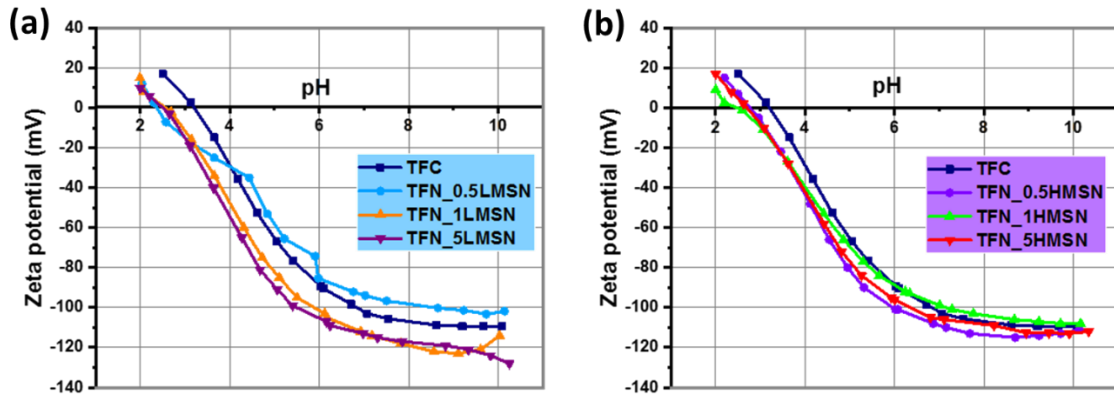


Figure 4.14: Effect of OTS concentration during MSN functionalization on the zeta potential of TFN membranes: a) with LMSN and b) with HMSN. The NPs loading in TFN membranes is 0.01 w/v%

4.2.2 Influence of OTS functionalization on the initial membrane performance

The separation performance of TFN membranes containing LMSN and HMSN at fixed NPs loading (0.01 w/v% filler concentration used in deposition step) is shown in **Figure 4.15**. The NaCl rejection of all membranes was higher than 93 %, which reflects the good incorporation of the NPs into the polyamide matrix. This can be attributed to the functionalization of the outer particle surface with the organic OTS-based layer enabling a very good dispersion in the organic phase (cf. **Section 4.1.2**). On the other hand, the permeance was influenced by the type of nanofiller. For lower degree of OTS functionalization, permeance was significantly increased while further increase led to a systematic decrease of the permeance. A permeability-rejection trade-off was not observed with the increase of the OTS concentration. Therefore, any change in the permeability was attributed to the impact of OTS concentration in both LMSN and HMSN nanofillers.

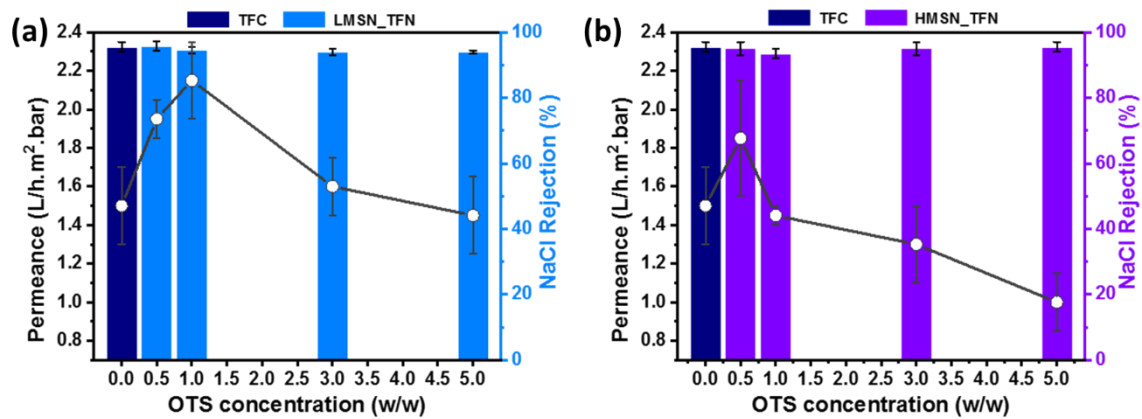


Figure 4.15: Effect of OTS concentration during MSN functionalization on the permeability and NaCl rejection of TFN membranes prepared at NPs loading of 0.01 w/v%: a) LMSN and b) HMSN

There are two scenarios with respect to the role of porous NPs to enhance TFN membrane permeability. Firstly, entrenching the NPs could alter the cross-linking of the polyamide layer thus producing larger aggregate pores in the barrier layer and, consequently, the permeability will increase [84]. Secondly, the internal pores of NPs could enhance the permeability by creating additional channels for water to pass through the barrier layer [127]. Both scenarios could also occur simultaneously. In both cases, it is assumed that no (additional) non-selective defects, i.e. pathways spanning through the entire polyamide barrier, are created by the addition of the NPs and salt rejection would not be compromised. No reduction in salt rejection was observed in this study. This would be in line with the conclusion from water contact angle data that most of the NPs were well covered with the polyamide layer (cf. **Section 4.2.1**). Alternatively, particles may also be covered by polyamide on the support side of the barrier layer. According to the results of this study, it is suggested that the second scenario is much more effective, because it is reasonable to expect that the formation of larger aggregate pores in the polyamide is not influenced by blockage the internal pores of the nanofiller. Instead, the results imply that the permeability was significantly reduced due to blocking the internal pores of the nanofiller with the hydrophobic OTS reagent. This emphasizes the most important role of the internal pores of MSN on improving the water transport during the water desalination process.

In order to further investigate the contribution of the mesoporous structure of MSN in improving the membrane permeability, the pure water and ethanol permeabilities were evaluated for TFC membranes with both, LMSN or HMSN as functional nanofillers. As depicted in **Figure 4.16 (a)**, the pure water permeability for TFN membranes containing LMSN

is always higher than that of the membranes with HMSN. In LMSN, the pores are rich with hydroxyl groups attached on the wall surfaces making them hydrophilic; therefore, the water can pass through effectively. In contrast, the functionalization with hydrophobic OTS in case of HMSN hinders water passage through these pores. It can be noted that the increase of permeance for the best TFN compared with the reference TFC membrane is up to 56 % in case of water and much higher for ethanol (up to 220 %). It was found that the ethanol permeability even in case of HMSN, was kept at higher values (**Figure 4.16 (b)**) which could be because the OTS molecules were insufficient to form a packed monolayer inside the internal pores even at the highest OTS concentration (as mentioned in **Section 4.1.2.1**). Therefore, the high affinity of ethanol toward the hydrophobic surface and its lower viscosity might allow ethanol to transport through the deformed OTS layer inside the pores producing a higher ethanol flux than water at the same pressure difference.

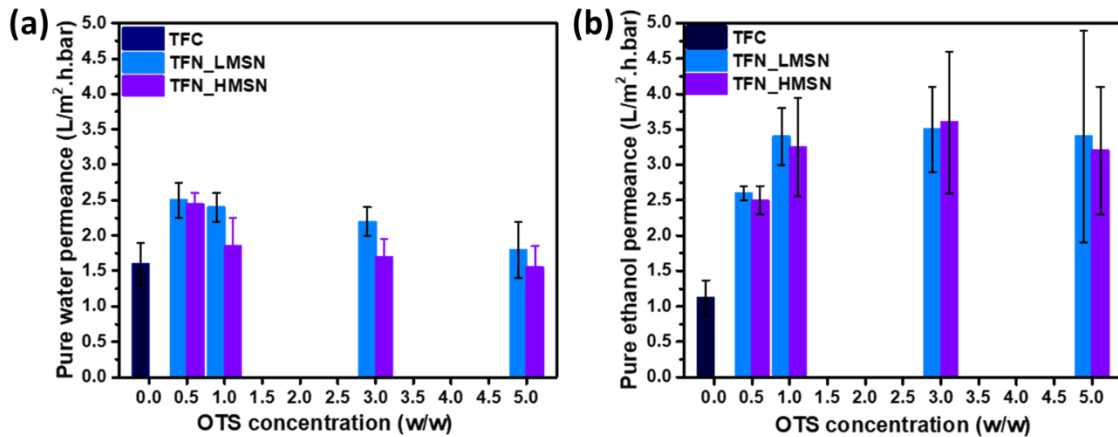


Figure 4.16: Effect of OTS concentration during MSN functionalization on: a) pure water permeability; b) pure ethanol permeability; for TFN membranes prepared at fixed NP loading (0.01 w/v%); data for TFC membranes prepared under identical conditions for comparison

To further quantify the wetting of the TFC and TFN membranes with LMSN or HMSN, the water contact angle was measured as a function of time (**Figure 4.17**). All data extrapolated to time zero are very similar (around 70°; cf. **Figure 4.13**). The data for the reference TFC membrane indicate that the hydration of the polyamide upon contact with the liquid water probe changes its wetting properties; in parallel, water is also penetrating into the membrane. It is obvious that the TFN membrane containing LMSN can be wetted much faster than the one containing HMSN and faster than the reference membrane. Qualitatively, this illustrates the additional influence of porosity on the barrier layer introduced by the nanofiller (for LMSN)

and the large influence of less effective pore wetting by water due to intra-porous OTS functionalization of the nanofiller (for HMSN).

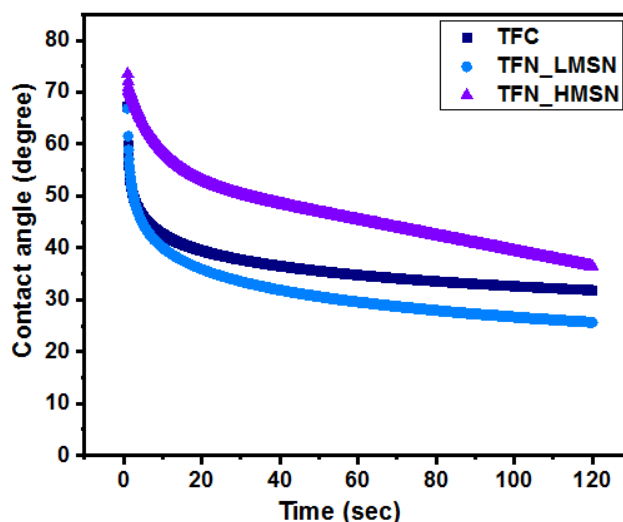


Figure 4.17: Effect of MSN pores hydrophilicity on the rate of membrane wettability change; TFN membranes prepared using either LMSN or HMSN at fixed NP loading (0.01 w/v%), OTS concentration during MSN functionalization was 0.5 w/w

According to all results presented in this section, it is elucidated that the TFN membrane containing LMSN functionalized with 0.5 w/w OTS revealed the best results in terms of water permeability and hydrophilicity, at the same salt rejection compared to the reference TFC membrane. This can be attributed to the fact that this quantity of OTS can effectively functionalize the external surface and cause defect-free integration into the polyamide-based barrier layer, which preserves the hydrophilicity of the internal pores. Therefore, the additional benefit with respect to enhancing the transport of water (or liquid in general) can be best utilized. Consequently, LMSN functionalized with 0.5 w/w OTS was used for all further experiments.

4.2.3 Influence of MSN loading on membrane performance

The loading of nanofillers had been varied by using different MSN concentrations dispersed in n-hexane under identical conditions for membrane preparation by IP method. Differences with respect to the relative fraction of OTS-functionalized MSN in the polyamide layer could be observed in ATR FTIR spectra (see **Figure 4.12**).

The zeta potential data of TFC and of TFN membranes with different LMSN loading are presented in **Figure 4.18 (a)**. In general, all membranes revealed high negative surface charge density, because of the carboxyl groups which formed by the hydrolysis of acyl chloride groups [12]. It is reported that the isoelectric point (IEP) of MSN is at $\text{pH } 3.7 \pm 0.2$ [211]. This is about the same value as reported for the IEP of polyamide obtained from MPD and TMC [212]. The

results demonstrate that there is no observed change in the IEP and only slight reduction in absolute zeta potential of TFC membrane by increasing fraction of OTS-functionalized silica. It is not expected that the functionalization of MSN with OTS would alter the IEP because only the fixed charge density will be decreased by covering the silica surface with neutral organic groups of OTS. The latter effect can explain the reduction in absolute zeta potential at high LMSN loading. Overall, the addition of LMSN has almost no influence on the membrane surface charge, and the net surface charge of the membranes is dominated by the properties of the polyamide layer.

The water contact angle of TFC and TFN membranes at different LMSN loading is presented in **Figure 4.18 (b)**. The contact angle of TFC membrane was ($67^\circ \pm 3$); contact angle for TFN membranes increased from ($68^\circ \pm 4$) to ($84^\circ \pm 4$) with increasing NPs loading from 0.003 to 0.05 w/v%, respectively, demonstrating that the surface of TFN membranes becomes more hydrophobic with increase of the NPs loading. The incorporation of NPs into the polyamide thin layer depends upon their loading through the IP process. The contact angle increased only weakly in the range of low NPs loading and increased strongly with the higher NPs loading. This could be because at low loading, most of NPs are completely covered with the polyamide layer while at high loading, more and more NPs became exposed to the outer surface, increasing the water contact angle because of the very hydrophobic properties of OTS-based surface layer. This would also be in line with the observed reduction in surface charge density (cf. **Figure 4.18 (a)**) due to the evoked dilution of carboxyl-containing polyamide for higher MSN loading (cf. above). This scenario is different from reports of many researches which used unfunctionalized hydrophilic inorganic NPs [18,141] or NPs functionalized with hydrophilic materials [178,213]. All observed that the contact angle of membrane surface decreased with increasing the NPs loading and attributed this to the hydrophilic property of the fillers. The difference in this study is that it had been attempted successfully to render the particle surface more hydrophobic.

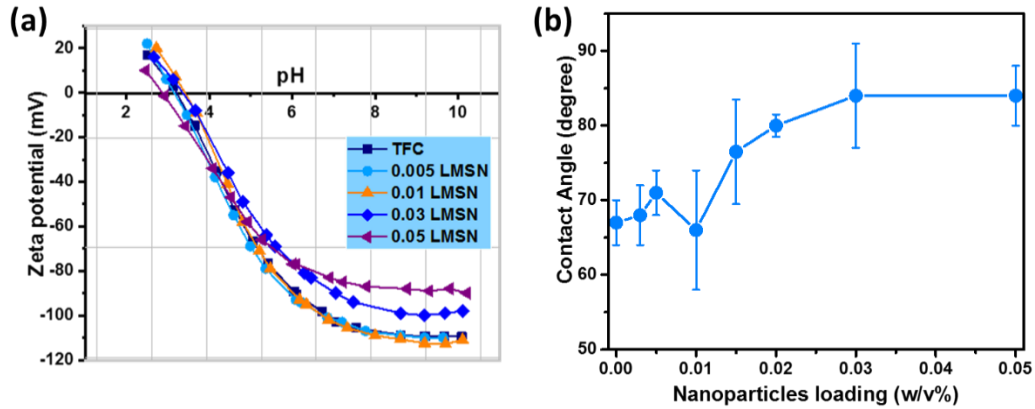


Figure 4.18: Effect of LMSN (OTS concentration during MSN functionalization 0.5 w/w) loading in TFN membranes on: a) zeta potential as a function of pH; b) water contact angle

The influence of NPs loading on permeability and salt rejection was also studied (**Figure 4.19**). Improvement of flux at same salt rejection was observed for 0.003 and 0.005 w/v%. Using deposition from 0.005 w/v% LMSN dispersion (0.175 mg in 3.5 ml hexane on a membrane area of $\sim 1660 \text{ mm}^2$) resulted in $\approx 63\%$ enhancement in the membranes' water permeability compared to the control TFC membrane. Improvement of water permeability in this range is most likely attributed to the internal pores of MSN which provide short flow paths for water. The water permeability was again reduced by further increasing the LMSN loading beyond 0.005 w/v%. However, only at 0.015 w/v% the salt rejection started to decrease; this is exactly the concentration where contact angle started to increase (cf. **Figure 4.18 (b)**). Further increase of NPs loading, further increased membrane surface hydrophobicity, and both water flux and salt passage also increased to reach the highest values at the highest loading (0.05 w/v%). This negative scenario with respect to separation performance beyond a critical NPs loading is most probably because of a too thick NPs layer deposited before IP reaction, leading to aggregation of the nanofiller and its exposure at the outer membrane surface along with increasing density of defects in the polyamide barrier layer.

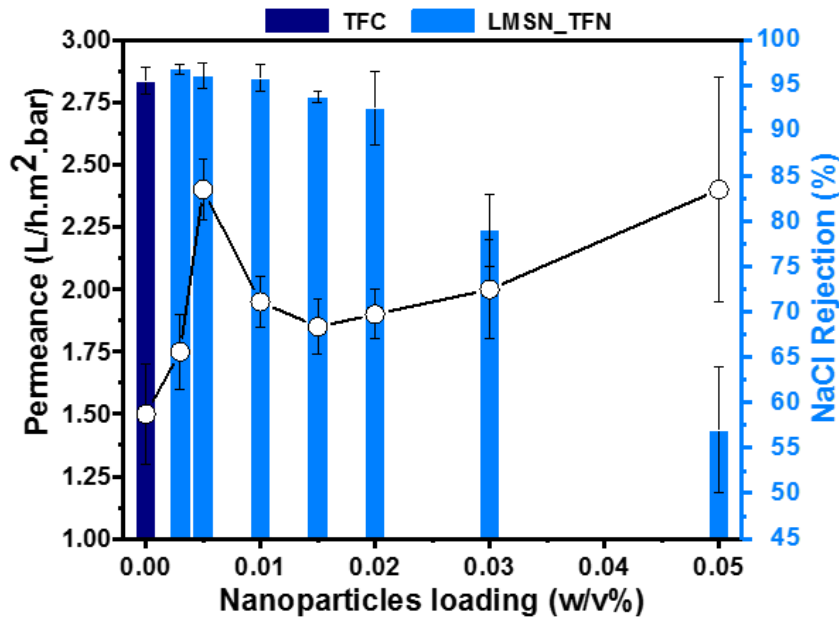


Figure 4.19: Effect of LMSN (OTS concentration during MSN functionalization 0.5 w/w) loading in TFN membranes on permeability and NaCl rejection during desalination

The effect of LMSN incorporation on membrane surface morphology was also investigated by SEM (**Figure 4.20**). The typical wrinkled morphology with nodular and leaf-like structure was observed for all membranes. The TFC membrane without NPs had a dense morphology with well distributed nodules throughout the membrane as a common structure for polyamide thin layer [84]. After the insertion of NPs, the surface morphology had less nodules and bigger leaf-like features. In the range of particle loading where a significant improvement of separation performance had been observed (0.003 and 0.005 w/v%), the overall surface topography was very regular. At higher NPs loadings (≥ 0.01 w/v%), the bigger heterogenous features which tentatively could be ascribed to nanofiller aggregates exposed on the outer surface became larger and more and more dominating. Therefore, a disconnected layer of polyamide might have been formed. Consequently, these membranes revealed an overall lower separation performance. Overall, these observations support qualitatively the argumentation based on complementary surface analysis (zeta potential and contact angle) and observed membrane performance (cf. above).

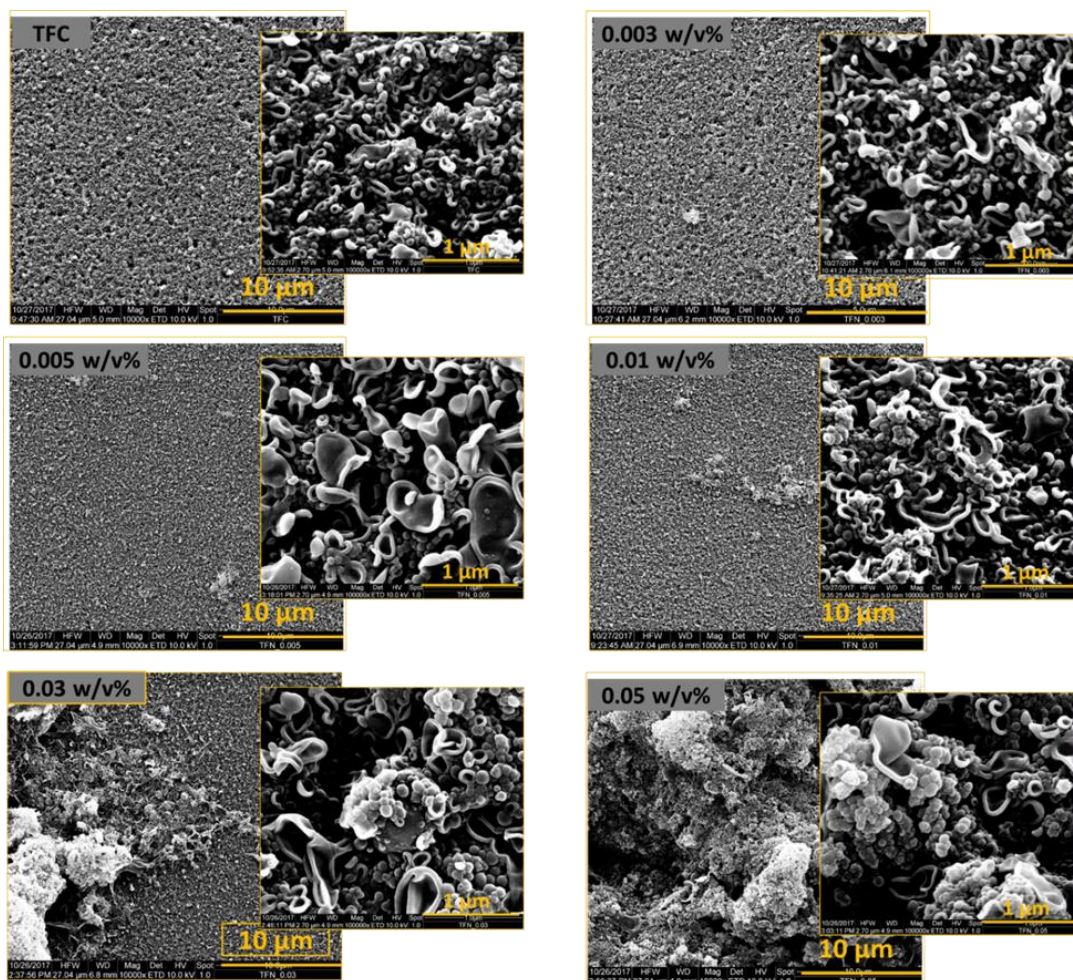


Figure 4.20: Top surface SEM images at different magnifications of TFC and TFN membranes with different LMSN loading (OTS concentration during functionalization 0.5 w/w)

As it was previously mentioned, the NPs were impregnated into the polyamide film in a separate step between MPD soaking of the porous support and TMC addition during the IP process (cf. **Section 3.3.2**). Hence, it is expected that after solvent evaporation a layer of NPs might be formed on the surface of the support membrane which is filled with the aqueous MPD solution. The thickness of this layer was estimated using the effective nanoparticle density which has been measured using mercury intrusion porosimetry (cf. **Section 4.1.2**).

The average thickness of deposited silica layer depends on the NPs loading; 0.003, 0.005, 0.01, 0.03 and 0.05 w/v% LMSN loading should yield a layer with a thickness of 56, 94, 188, 564 and 940 nm respectively (**Table 4.4**). Of course, this is only an estimation; the thickness utilized for integration into the PA layer may be significantly lower when NPs will be re-dispersed from the support membrane surface upon addition of the TMC solution in hexane. Nevertheless, this scenario is more likely for thicker layers.

Table 4-4: Maximum thickness of LMSN layer deposited on base PES membrane before IP, estimated from effective density of NPs powder measured by mercury porosimetry as well as concentration and volume of nanoparticle dispersion applied to the membrane sample area

LMSN loading (w/v%)	Thickness of LMSN layer (nm)
0.003	56
0.005	94
0.01	188
0.03	564
0.05	940

In the low NPs loading range (0.003 and 0.005 w/v%), the average thickness corresponds to less than or about a monolayer of NPs (diameter 80 nm) and less than the apparent thickness of the reference TFC membrane (140 ± 28 nm; estimated from the SEM image; **Figure 4.21**). The thickness of the PA layer of the TFN membranes obtained with these loadings is roughly similar to the thickness of the reference TFC membranes. For the higher loadings, the thick layer of silica produced a loose polyamide layer which surround the particles. It seems that the large thickness of silica prevented formation of robust polyamide layer which is obvious from SEM cross-section images (cf. **Figure 4.21**).

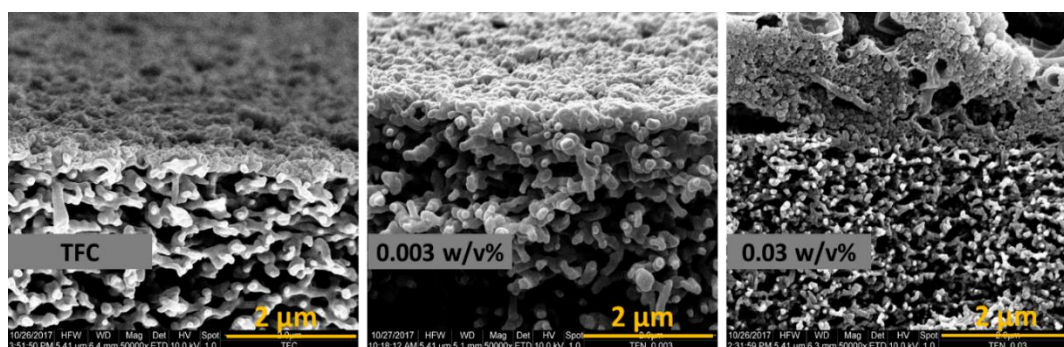


Figure 4.21: SEM cross-section images of TFC and TFN membranes with different loading of LMSN (OTS concentration during MSN functionalization 0.5 w/v%)

At the end of this section, to investigate the role of OTS functionalization, the filtration performance of the LMSN and HMSN based membranes should be compared to the TFN membranes containing the same loading of the native hydrophilic MSN. As can be observed in **Figure 4.22**, incorporation of the unfunctionalized MSN into the PA layer led to an increase of the permeability but significantly reduced the salt rejection.

This result was expected due to the hydrophilic nature of the native MSN which led to a poor integration within the PA layer. SEM was employed to study the surface morphology of this membranes as depicted in **Figure 4.23**. It is very clear that the unfunctionalized MSN can be agglomerated; therefore a poor distribution inside the PA layer can be clearly observed. The resulted agglomeration of MSN caused uneven distribution inside the PA layer leading to a looser PA structure or defects, and therefore it impaired the overall separation performance as indicated by the lower salt rejection (cf. **Figure 4.22**).

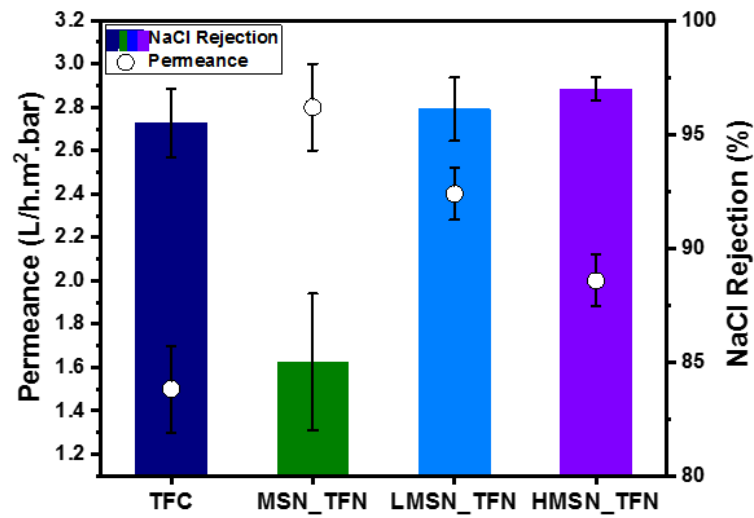


Figure 4.22: Permeance and NaCl rejection during RO experiments (2 g/L NaCl in water as feed) of TFC and TFN membranes. The NP loading for TFN membranes is 0.005 w/v%

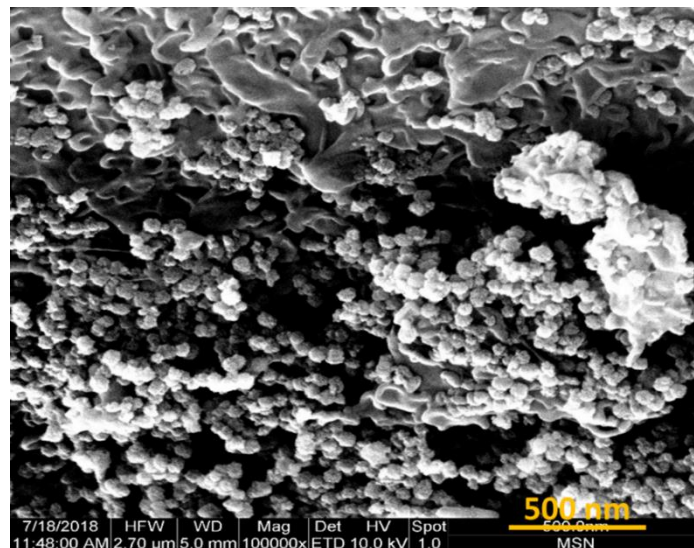


Figure 4.23: SEM of the top surface of MSN_TFN membrane at 0.005 w/v% loading

It is meaningful to compare the performance of membranes prepared in this study with those TFN membranes with mesoporous silica NPs reported in the literature [17,18,123,127]. When considering that there is no loss of NPs used during the membrane formation, the quantity of

NPs in the unit area of membrane which achieved the optimal performance in this study is 0.18 g/m². As can be presented in **Table 4.5**, this quantity is the lowest among all literature data which used MSN as inorganic fillers for TFN membranes.

Table 4.5: A performance comparison of TFN membranes in the literatures to this work

Optimal loading Wt/v%	MSN	Water permeance (L.h.m ² .bar ⁻¹)	NaCl rejection (%)	Reference
0.005		2.45	96	This work
0.1		2.3	98	[17]
0.1		3.5	96	[127]
0.14		2.6	95	[18]
0.015		3	95	[123]

4.3 Stability of MSN

In this section we study the stability of the native and the OTS functionalized MSN at different pH values. The chemical stability of the nanofiller should affect the membrane performance during the filtration experiments. the higher the nanofiller stability, the higher also the membrane performance stability.

4.3.1 Dissolution of MSN

The dissolution of the different silica NPs was investigated through well-mixed dispersion containing initially 2 g/L solid at two different pH values, pH 5 and pH 9, for 170 hours. The dissolved silica concentration was spectrophotometrically determined using molybdosilicate method and the results are presented in **Figure 4.24**.

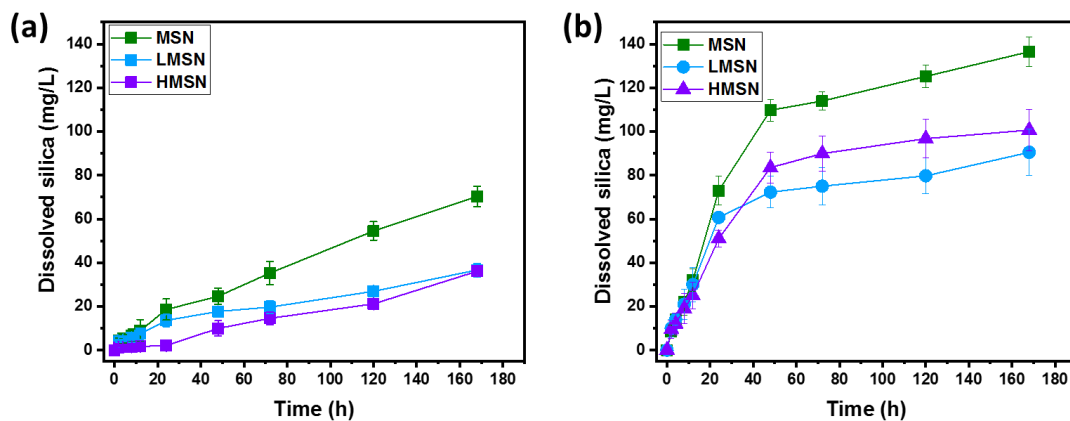


Figure 4.24: Dissolution of MSN, LMSN and HMSN at (a) pH 5 and (b) pH 9. The initial solid concentration was 2 g/L and the initial pH was adjusted using HCl and NaOH to pH 5 and pH 9, respectively

In general, the dissolved silica concentration in basic solution (pH 9) is much higher than in acidic solution (pH 5). The amounts of dissolved silica released in the first 24 hours in case of

pH 9 are similar to the amounts released along the whole 170 hours in case of pH 5. The dissolution curve of the samples in pH 9 (cf. **Figure 4.24**) is characterized by relatively fast rate up to 48 hours followed by much slower rate until the end of experiment. This behavior could be interpreted by the decrease of pH as a result of formation of silicic acid (pH decreased from 9 to 8 after 170 h), and in addition to reaching the saturation level (120 mg/L) for amorphous silica [21,214].

In order to attain deeper knowledge about the impact of pH on the dissolution reaction kinetics, the initial rate, expressed as the initial rate constant, was determined in the first 12 hours, in which the dissolved silica concentration increases linearly with time. The silica dissolution showed first-order rate law, and the rate constant was calculated according to **Equation 4.3** [215]:

$$\ln\left(\frac{(C_o - C_t)}{C_o}\right) = -kt$$

Equation 4.3: First-order rate constant equation

Where C_o is the initial silica concentration and C_t is the concentration of dissolved silica measured at time (t).

The rate constant (k) was determined using the slope of $\ln\left(\frac{(C_o - C_t)}{C_o}\right)$ vs. time as presented in **Figure 4.25**. The obtained rate constants for both native and OTS-functionalized MSN at pH 5 and pH 9 are presented in **Figure 4.26**. According to the results, at pH 9, the silica dissolved at a rate that was approximately 10 times faster than that at pH 5. The faster dissolution at the high pH could be explained by the more efficient deprotonation of silicic acid (H_4SiO_4) to $H_3SiO_4^-$ and $H_2SiO_4^{2-}$ in the alkali solutions (cf. **Reactions 2.5** and **2.6**). These results are in a general agreement with other reports [176,216]. Moreover, it can be observed that MSN dissolved at a rate which is moderately faster than LMSN or HMSN (cf. **Figure 4.26**). Because of the hydrophilic surface of MSN, it can be easily contacted with water and can be easily dissolved. The less efficient dissolution observed for functionalized samples is most likely because of the coverage by an organic layer due to OTS functionalization. This would diminish the efficiency of the water attack to the siloxane (Si-O) bonds.

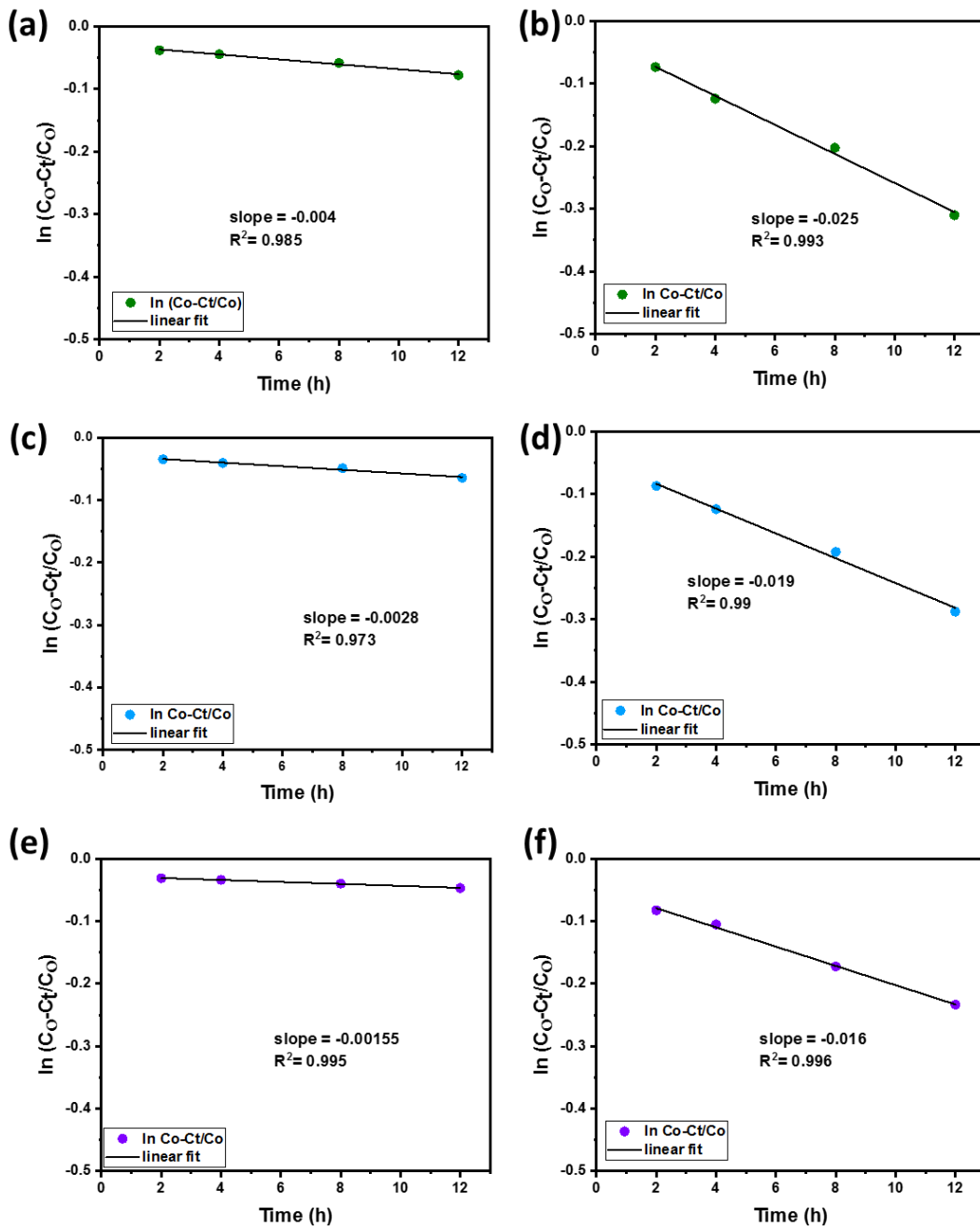


Figure 4.25: Plots of $\ln(C_o - C_t/C_o)$ vs. time to calculate the dissolution rate constant of MSN (a,b), LMSN (c,d) and HMSN (e,f) at pH 5 and pH 9, respectively

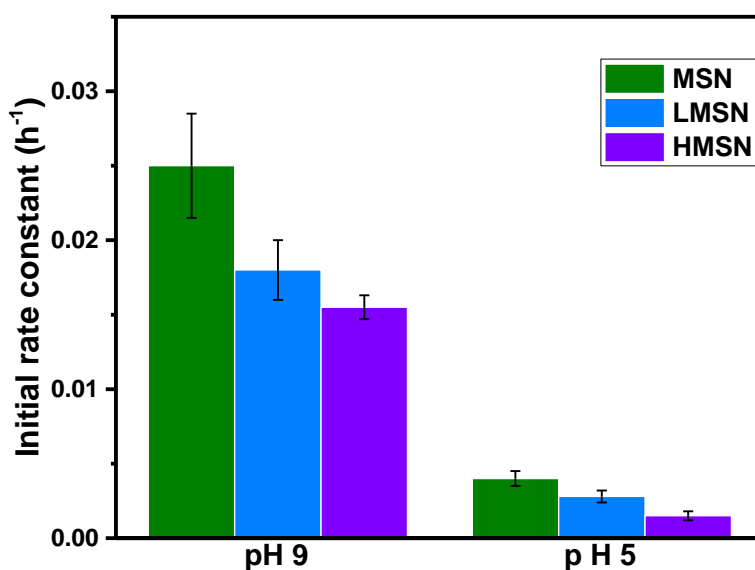


Figure 4.26: Rate constant of dissolution of MSN, LMSN and HMSN during the first 12 hours of the experiments at pH 5 and pH 9

4.3.2 Influence of the dissolution on the NPs structure

The structure of unfunctionalized and OTS-functionalized MSN before and after partial dissolution has been investigated using small angle XRD, SEM and TEM.

The XRD data for the native MSN, LMSN and HMSN, before and after dissolution experiment, are presented in **Figure 4.27**. The obtained patterns of the native MSN revealed four characteristic peaks at 2θ of 2.2° , 3.8° , 4.3° and 5.7° representing the (100), (110), (200) and (210) planes, respectively. This structure is consistent with the hexagonal lattice symmetry of MCM-41. The XRD patterns of both LMSN and HMSN showed a decrease in overall intensities of XRD reflections compared to the base MSN. This is probably due to the difference of scattering power between the silica wall and the organic moieties (OTS), which are located outside or inside the MSN pores [217,218]. On the other hand, the XRD results showed an intensity decrease in the main peak (100) and complete disappearance of the other peaks (110, 200 and 210) for all partially dissolved samples. These results indicate that the mesoporous structure was strongly influenced by partial dissolution. Nevertheless, the presence of the peak (100) in the XRD pattern indicated that the mesoporous structure was not completely destroyed [219].

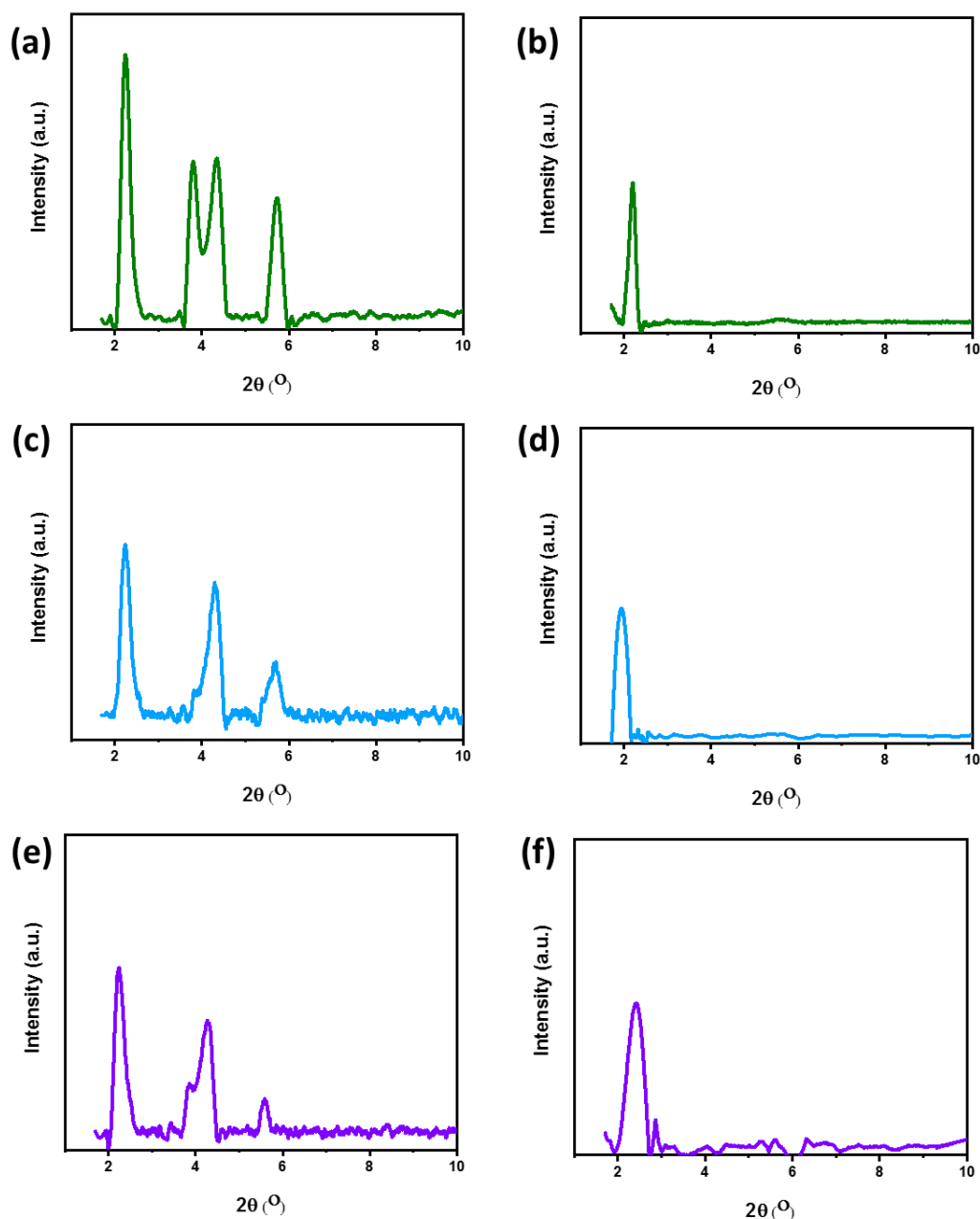


Figure 4.27_ Small angle XRD of the native MSN (a, b), LMSN (c,d) and HMSN (e,f) before and after the partially dissolved in water at pH 9 after 170 hours, respectively

The porous structure and morphology of LMSN and HMSN before and after partial dissolution were also investigated by TEM and SEM, and the results also indicated that an improved stability compared to the native MSN could be achieved due to OTS functionalization. As can be seen in **Figure 4.28**, all SEM micrographs showed no significant change in the morphologies before and after partial dissolution. All revealed spherical particles. However, according to **Table 4.6**, the particle size estimated from SEM (**Figure 4.28**) and TEM (**Figure 4.29**) micrographs decreased after partial dissolution. The particles seem to be degraded (cf. **Figure 4.29**) which causes the reduction of the particle size. This decay is quite

obvious for the native hydrophilic MSN which is more prone to be dissolved in alkaline aqueous solution than the hydrophobic species. The later were more stable but revealed also somewhat decrease in the particle size which is most likely because the complete surface coverage was not achieved at the used OTS concentration during the silanization. The OTS-free sites on the surface can allow degradation of the particle's walls [20].

Table 4.6: Particle size analysis of the different silica NPs before and after partial dissolution in aqueous solution at pH 9

Sample	Particle size from TEM (nm)		Particle size from SEM (nm)	
	Before dissolution	After dissolution	Before dissolution	After dissolution
MSN	85±7	66.5±6	79 ± 9	70 ± 16
LMSN	75±6	70±6	70± 10	71± 12
HMSN	83±10	79±9	71± 8	66± 11

Moreover, the hexagonal array of the mesoporous structure of all samples is clearly displayed for the native samples. In contrast, the ordered structure of the NPs after the dissolution experiment was less obvious, in particular for MSN compared to the functionalized NPs (LMSN and HMSN) as can be seen if **Figure 4.29 inset**.

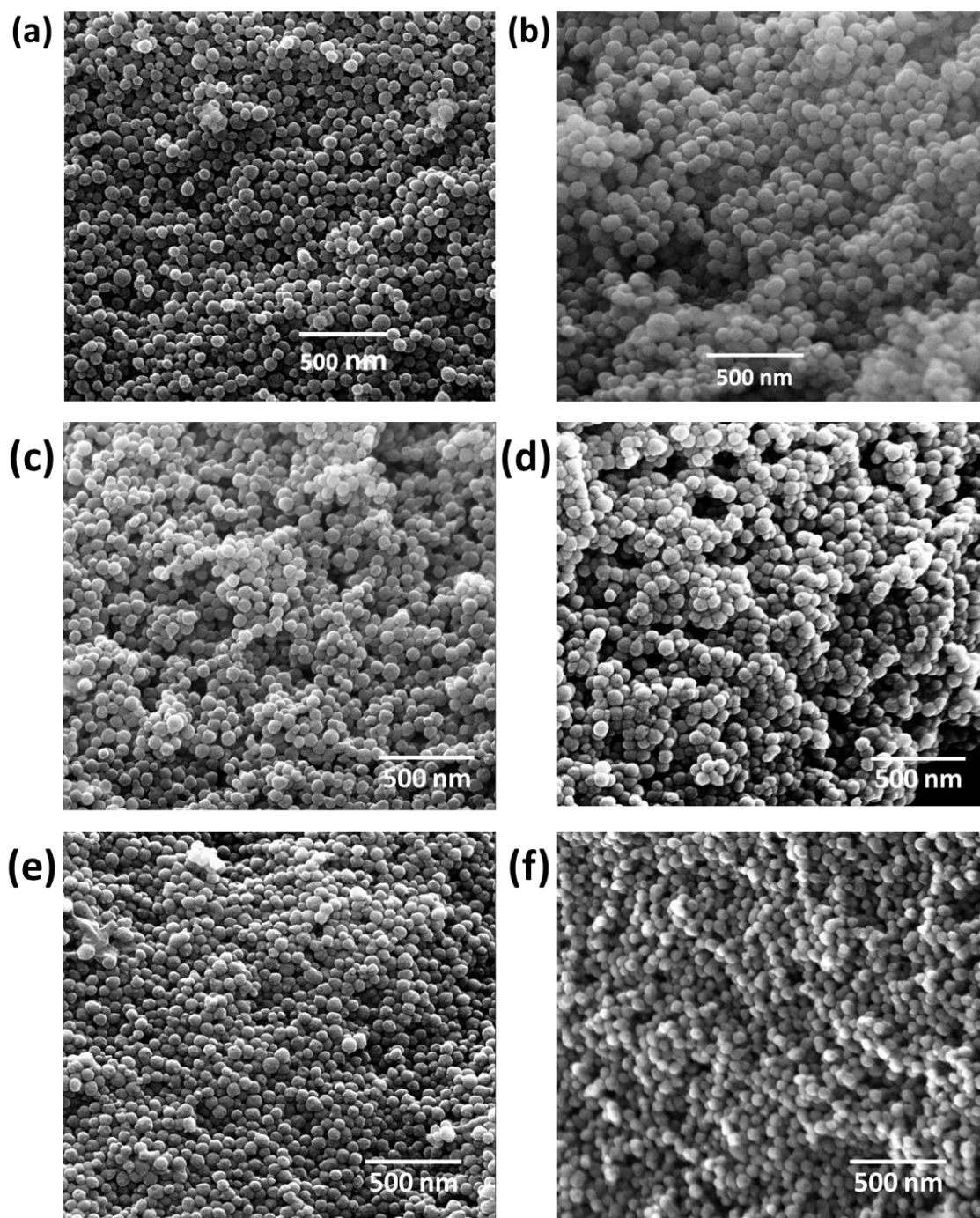


Figure 4.28: SEM micrograph of the native MSN (a, b), LMSN (c,d) and HMSN (e,f) before and after the partial dissolution in water at pH 9 after 170 hours, respectively

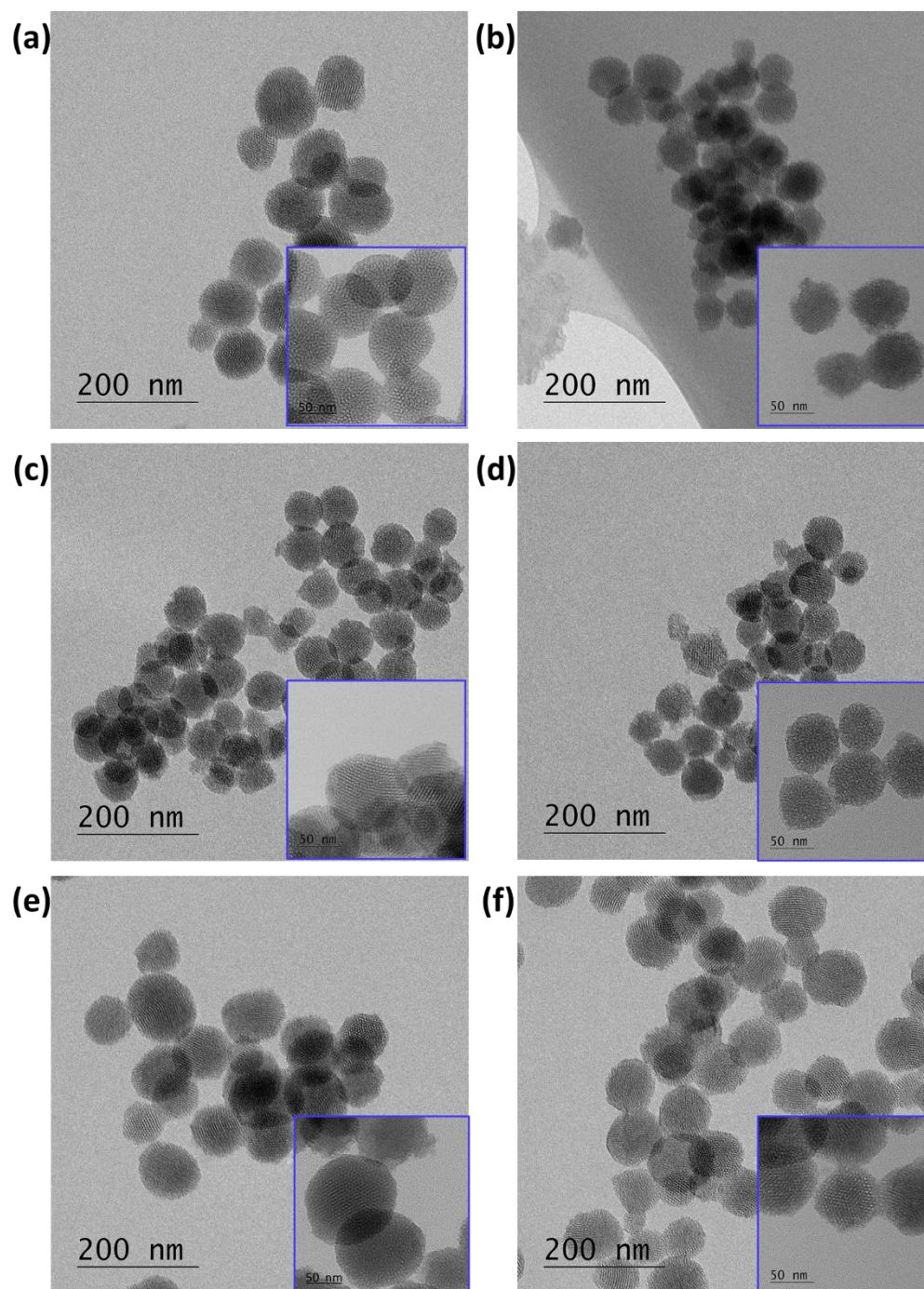


Figure 4.29: SEM micrograph of the native MSN (a, b), LMSN (c,d) and HMSN (e,f) before and after the partial dissolution in water at pH 9 after 170 hours, respectively

The nitrogen adsorption isotherms of all materials before and after partial dissolution can be described by “type IV”, as can be seen in **Figure 4.30 (a, c and e)**. This was found even for the MSN with a strong dissolution tendency, indicating that the porous structure has not been completely decomposed. The main characteristic properties of MSN and OTS-functionalized MSN which can be derived from the nitrogen adsorption measurements are summarized in **Table 4.7**. After the partial dissolution at pH 9 for 170 hours, the specific surface area (S_{BET})

of the unfunctionalized MSN decreased from 920 m²/g to 650 m²/g (\approx 30% loss). Moreover, the average pore diameter (d_p) (**Figure 4.30 (b, d and f)**) decreased from 3.3 nm to 2.9 nm, and the pore volume (V_p) also decreased from 0.83 cm³/g to 0.64 cm³/g. These findings agree with the observations from both XRD and TEM in **Figure 4.27** and **Figure 4.29**, respectively. The relationship between the partial loss of the hexagonal order of MSN and the reduction of both d_p and V_p was explained by Gouze et al. [220]. They attributed this result to the dissolution of silica walls and to the recondensation of hydrolyzed silica on the pore surface, leading to a partial pore clogging which could be the reason of reduction of d_p from 3.3 to 2.9 nm and V_p from 0.84 to 0.63 cm³/g. The reduction of V_p is also in the line with the lower S_{BET} .

In contrast, LMSN and HMSN exhibited less pronounced decreases in S_{BET} , d_p and V_p than the unfunctionalized MSN. The lower drop in S_{BET} , d_p and V_p for LMSN and HMSN is most likely due to the fact that the mesoporous structure was better conserved, which is attributed to the hydrophobicity of the OTS layer on the particles surface which creates a resistance toward water and therefore higher resistance to the dissolution effect. These results are similar to the results in literature [180,221], which also reported the stabilization of mesoporous silica NPs by surface modification with organic layers.

Table 4.7: Characteristic porosity data of unfunctionalized and OTS-functionalized MSN before and after 170 h exposure at room temperature in water at pH 9, obtained from nitrogen adsorption measurement

Sample	Before dissolution			After partial dissolution		
	S_{BET} (m ² /g)	d_p (nm)	V_p (cm ³ /g)	S_{BET} (m ² /g)	d_p (nm)	V_p (cm ³ /g)
MSN	920	3.3	0.84	650	2.9	0.63
LMSN	895	2.8	0.75	750	2.7	0.68
HMSN	490	2.4	0.33	450	2.5	0.30

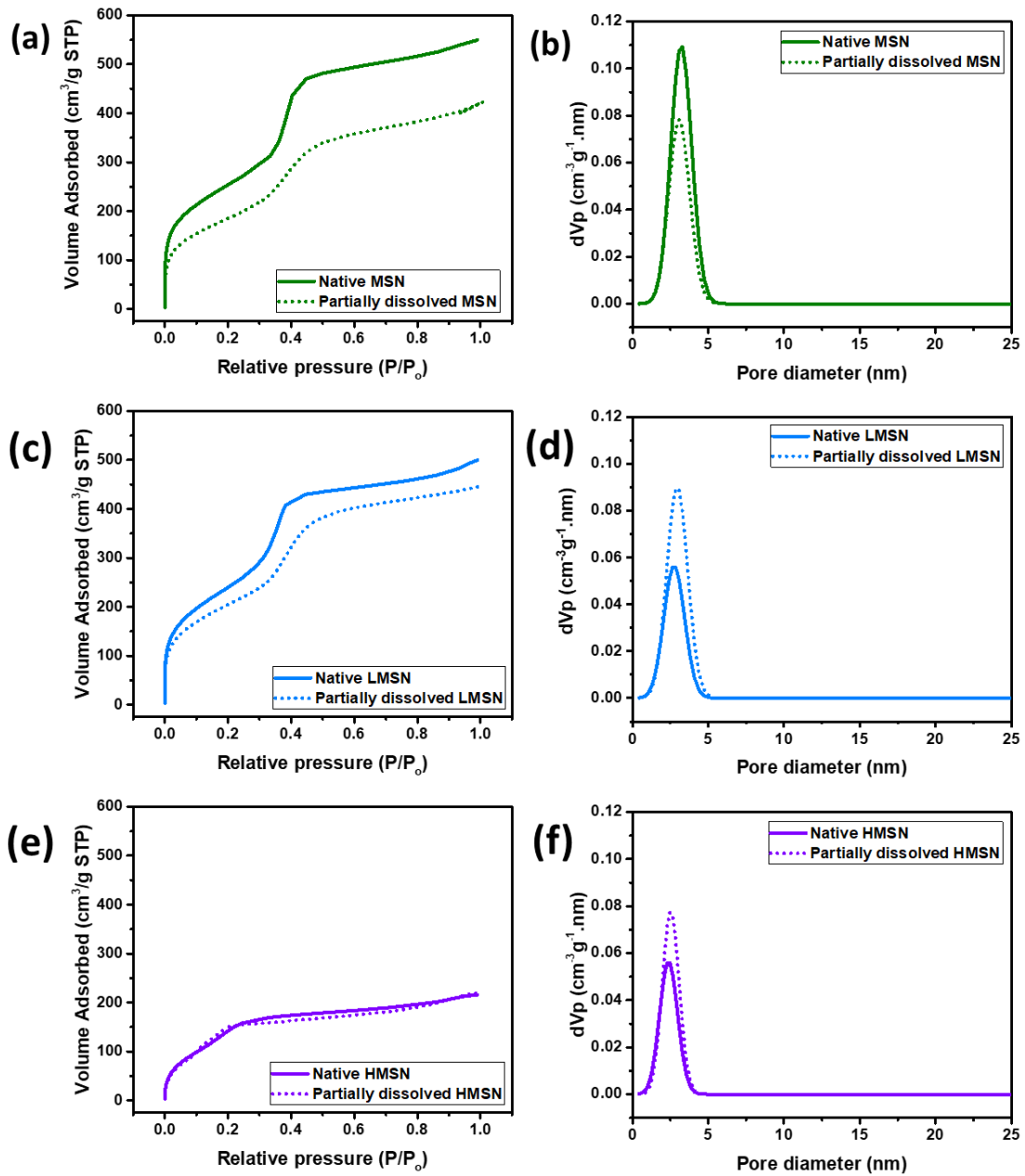


Figure 4.30: Nitrogen adsorption isotherms (a, c and e) and derived pore size distributions (b, d and f) of native and partially dissolved MSN, LMSN and HMSN after 170 hours at pH 9, respectively

4.4 Stability of TFN membranes

4.4.1 Influence of MSN nanofillers dissolution on TFN membrane separation performance and barrier layer structure

The stability of separation performance of the TFC and the various TFN membranes was studied under cross-flow conditions at an operating pressure of 16 bars for a total of 120 h at each pH value. **Table 4.8** shows the relative variation in both permeance and salt rejection after

completion of the desalination experiment. At pH 5, LMSN_TFN and HMSN_TFN membranes revealed more stable permeance and salt rejection than MSN_TFN membranes which showed a significant increase in permeance and decrease in salt rejection as can also be seen in **Figure 4.31 (a, b)**. The dissolution of LMSN and HMSN at pH 5 is relatively slow (cf. **Figures 4.24 and 4.26**) which indicates their stability in that pH condition. This is probably the reason for the stability of the respective TFN membranes at pH 5. MSN dissolution rate at pH 5 is significantly higher than for OTS-functionalized NPs (cf. **Figure 4.26**) which explains the lower stability of MSN_TFN membranes.

In case of pH 9, the variation in both permeance and salt rejection of all TFN membranes is larger than at pH 5 (cf. **Table 4.8**), indicating less stable performance compared to the reference TFC membrane. However, TFN membranes with either LMSN or HMSN achieved significantly better stability compared to MSN_TFN membranes, as can also be seen in **Figure 4.31 (c, d)**. The much stronger decline in the permeance of MSN_TFN membranes over time at pH 9 compared to pH 5 is most likely because the rate of dissolution of MSN at pH 9 is much higher (cf. **Section 4.3**). Because of the presence of OTS - based organic layer in case of LMSN and HMSN, on the other hand, their respective TFN membranes achieved better stability and obviously improved the separation performance.

Table 4.8: Relative variations of permeance and salt rejection for all membranes during 240 h filtration of NaCl solution at pH 5 and pH 9, (+) sign means parameter increase and (-) sign means parameter decrease.

Membrane	Permeance variation (%)		Rejection variation (%)	
	pH 5	pH 9	pH 5	pH 9
TFC	-5.5	-5.1	-0.8	+0.5
MSN_TFN	+20.5	+23.1	-4.2	-34.5
LMSN_TFN	+5.4	+15.0	-1.2	-6.1
HMSN_TFN	+7.2	+19.0	-2.9	-8.2

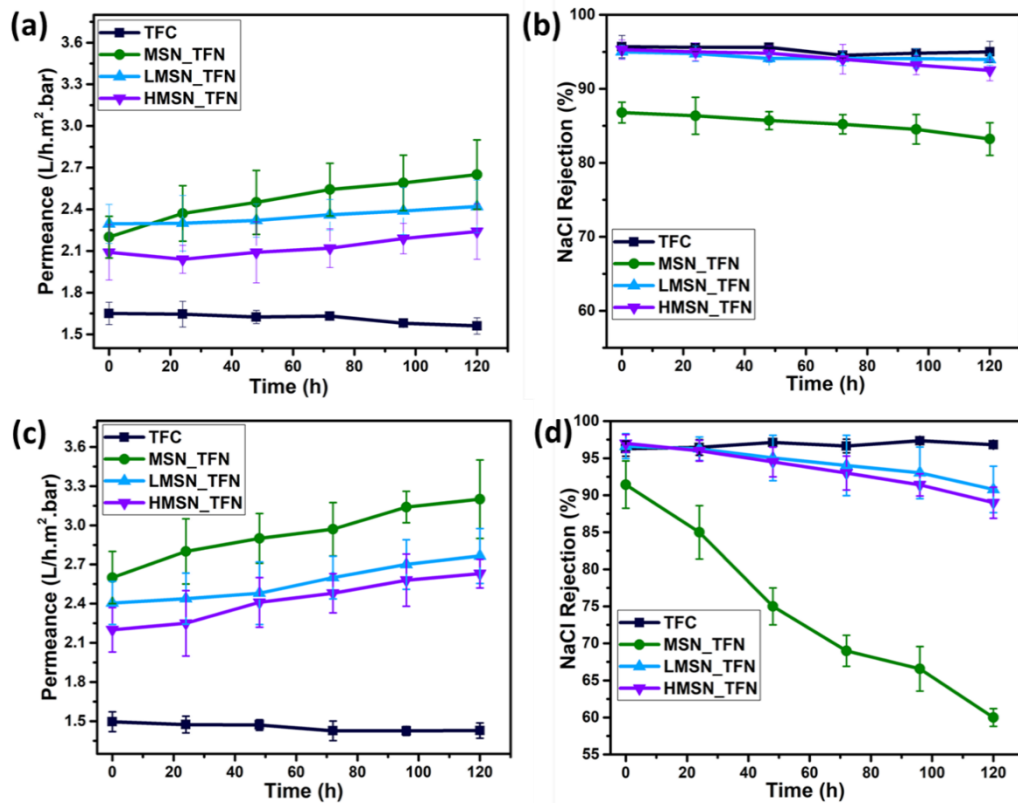


Figure 4.31: Long-term separation performance of TFC and TFN membranes for first 120 h at pH 5 (a, b) and for second 120 h at pH 9 (c, d) using the same membrane.

Figure 4.32 shows the SEM images of the top surfaces of TFC and TFN membranes with different MSN nanofillers before and after filtration experiments. The common “ridge and valley” structure of PA layer was observed for all membranes even for the tested membranes. Nevertheless, the top surface of the TFN membranes varies with the variation of the nanofiller, i.e. unfunctionalized or OTS functionalized MSN (cf. Figures 4.20 & 4.23).

The instability of the nanofiller might lead to their removal from the PA layer [177] or creation of voids around partially dissolved NPs in the PA layer.

Because the quantity of the nanofillers used for fabrication of these membranes is quite low (0.005 w/v%), it was assumed that they are completely covered with the PA layer (cf. Figure 4.20). Therefore, leaching of the entire NP is essentially avoided in case of LMSN and HMSN due to the very good integration in the PA film, thanks to their hydrophobic outer surface properties. However, in case of unfunctionalized MSN, the hydrophilic surface of NPs obviously leads to their aggregation in the organic solvent and thus to an uneven distribution in the PA layer (cf. Figure 4.32), and therefore they could be dissolved and/or removed, leading to voids or defects.

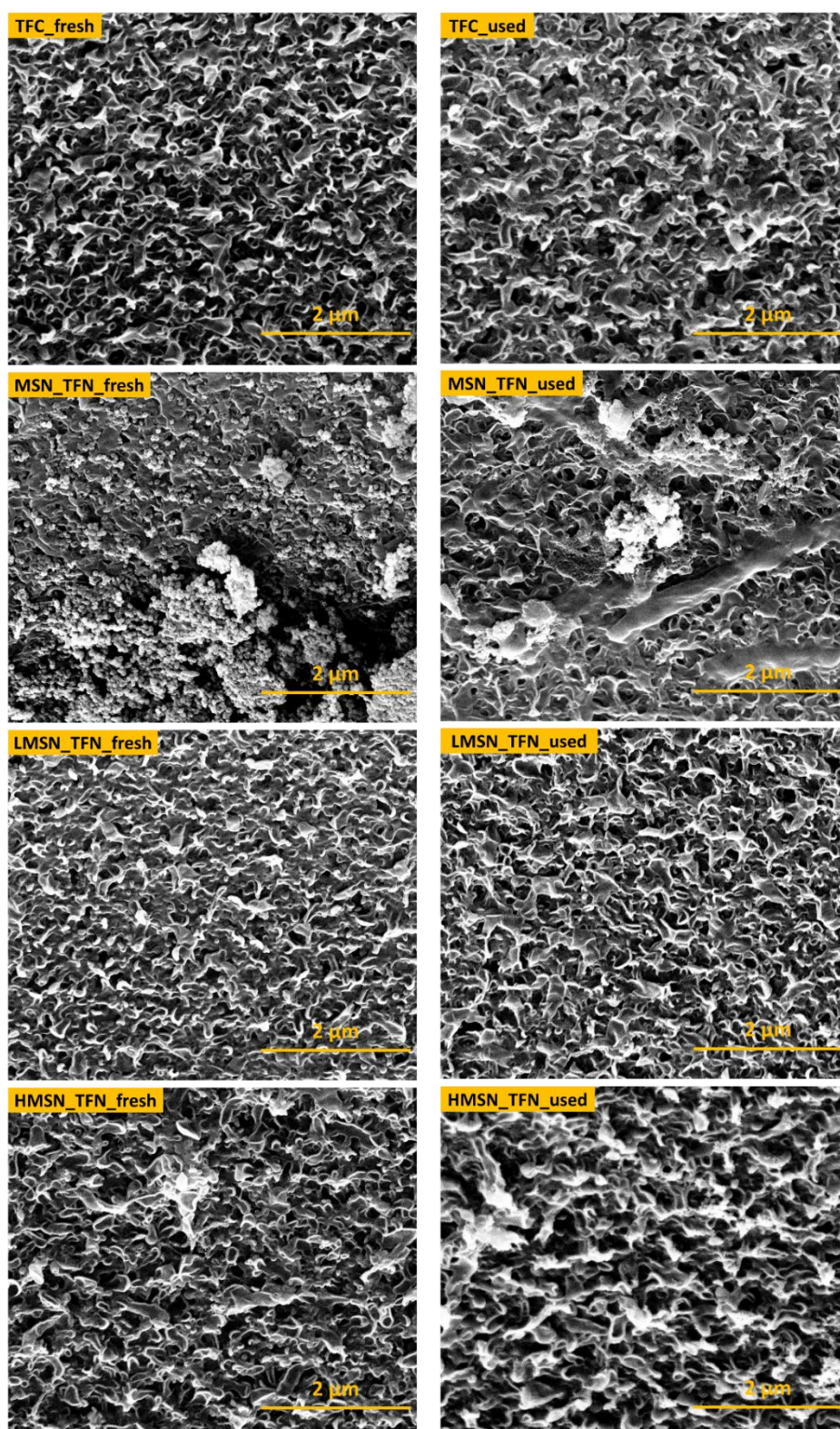


Figure 4.32: SEM images of TFC and TFN membranes before and after filtration of NaCl solution for 120 hours at pH 5 and thereafter 120 hours at pH 9

In order to clarify the role of different nanofiller instability on the properties of TFN membranes, the impact of NPs dissolution on the durability of the PA barrier layer was investigated in an additional experiment. Toward this aim, solutions of dextran with different molecular weight (4 kDa to 2000 kDa) were filtrated through the membranes which had previously been tested with NaCl solutions for 240 h (120 h for each pH). The average hydrodynamic diameter for each dextran fraction was estimated based on the correlation between Stokes diameter and molecular weight of dextran according to **Equation 4.9** [222].

$$d_s(\text{nm}) = 0.066 \times MM^{0.46} \quad \text{(Equation 4.9)}$$

Where MM is the molecular weight (kg/mol).

The average diameter values are summarized in **Table 4.9**. Analogous dextran feed solutions were filtered through the native membranes (before desalination experiments), and the obtained results (**Figure 4.33 (a)**) showed that all membranes were able to reject $\geq 99\%$ of all dextrans (this may correspond to quantitative rejection considering the detection limit of the used method based on TOC), indicating that the membranes had no defects with sizes in the lowest nm range.

The results after long-time desalination experiments (**Figure 4.33 (b)**) demonstrate that the rejection of the reference TFC membrane and of the LMSN_TFN membrane was still higher than 99% for all dextrans, indicating no micro-/mesoporous defects. For the HMSN_TFN membrane, the rejection of dextran 4 kDa (3 nm) was less than 99% while the data for the other dextrans were above 99%. This may confirm again the lower stability against dissolution for HMSN than for LMSN, due to the less well assembled OTS layer on the external surface (cf. **Section 4.1.2**), which could be the reason of the slight decline in the 4 kDa dextran for the HMSN_TFN membranes after long-time tests. Rejection of all dextrans was lower than 99% for MSN_TFN membranes; the lowest value (92%) was observed for dextran 4 kDa. This observation could suggest that the dissolution of MSN created some defects in the barrier layer which is sufficient to make it no longer able to reject the large dextran molecules.

In comparison, LMSN_TFN and HMSN_TFN membranes had largely improved stability as a result of not percolated and well dispersed nanofillers inside the PA layer as well as their higher resistance toward dissolution in aqueous solutions. The unchanged surface morphology of the TFN membranes after desalination experiments compared to the native membranes (cf. **Figure 4.32**) could also support this interpretation, but detailed statements are not possible due to resolution limitations of the SEM analyses.

Table 4.9: Average hydrodynamic diameter of different dextrans used in filtration experiments

Molecular weight (kg/mol)	diameter (nm)
4	3
35	8
100	13
200	18
2000	52

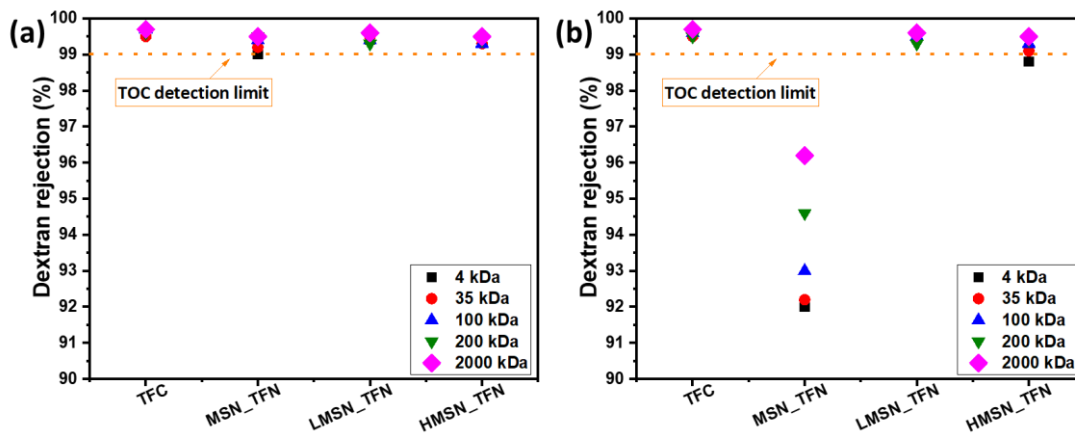


Figure 4.33: Rejection of dextran with different average molecular weight (4 kDa - 2000 kDa; feed concentration 1 g/L in water) for a) the native membranes and b) the previously tested membranes for desalination performance for 120 h at pH 5 and 120 h at pH 9 (cf. Figure 4.32).

4.5 Influence of silane molecule size used for MSN functionalization

In this section, we studied the characterization of both MSN and the respective TFN membranes in case of using a smaller silane molecule such as methyltrichlorosilane (MTS) instead of OTS for MSN functionalization. In addition, the influence of the shorter alkyl chain on the stability of the particles and membranes was studied. The results of this section were compared to the obtained result with OTS as organic functionalization agent.

4.5.1 Influence of MTS functionalization on MSN properties:

The nitrogen adsorption was measured for MSN functionalized with different MTS concentration (0.5 -5 w/w). The specific surface areas and the corresponding pore diameters are shown in **Table 4.10**.

Table 4.10: BET surface area and pore diameter of LMSN and HMSN obtained after functionalization at different MTS concentrations

MTS concentration (w/w)	BET surface area (m ² /g)		Pore diameter (nm)	
	LMSN	HMSN	LMSN	HMSN
0	1095		3.0	
0.5	1074	929	2.8	2.9
1	1058	826	2.8	2.8
3	1005	818	2.8	2.9
5	984	648	2.7	2.9

According to the table, the decrease in the surface area of HMSN is more significant than for LMSN, which indicates the internal pores have been functionalized with the MTS molecules. Nevertheless, the change in pore diameter is insignificant in both LMSN and HMSN. These results are quite dissimilar to OTS results. The decline in surface area because MTS and OTS grafting was calculated and summarized in **Table 4.11**. As can be seen, the decline in surface area for MTS functionalized NPs is always lower than the OTS case, even in case of HMSN with high MTS concentration. This is mainly attributed to the very small size of MTS molecule which can functionalize the wall of the interior pores without filling the whole pore or closing the pore entrance as in case of the big OTS molecule. This is also supported by the insignificant change in the pore diameter of HMSN in case of MTS compared to the large decrease in case of OTS (cf. **Table 4.3**)

Table 4.11: Decline of surface area for functionalized MSN with MTS and OTS

OTS concentration (w/w)	Decline of surface area (%)			
	MTS_HMSN	MTS_LMSN	OTS_HMSN	OTS_LMSN
0.5	15.0	2.0	47.0	2.7
1	25.5	3.0	92.0	24.5
3	25.0	8.0	94.0	26.0
5	41.0	10.0	95.0	35.0

The TGA was also measured for MSN functionalized with different MTS concentration as presented in **Figure 4.34**. As can be observed, the weight loss increased with increasing MTS concentration and is higher for HMSN than for LMSN at the same MTS concentration. This was expected, due to the large surface accessible for silanization in case of HMSN. Similar results were obtained for the OTS functionalized NPs. Nevertheless, the latter showed much

higher weight loss at the same concentrations, due to the big difference of alkyl chain length (cf. **Figure 4.9**). The number of methylsilanes per area was also estimated (**Table 4.12**) using the same assumptions which are previously explained in **Section 4.1.2.1**.

According to the results in **Table 4.12**, the covering (number of MTS molecules/nm²) increases with increasing the MTS concentration for both LMSN and HMSN, because increasing the organic content.

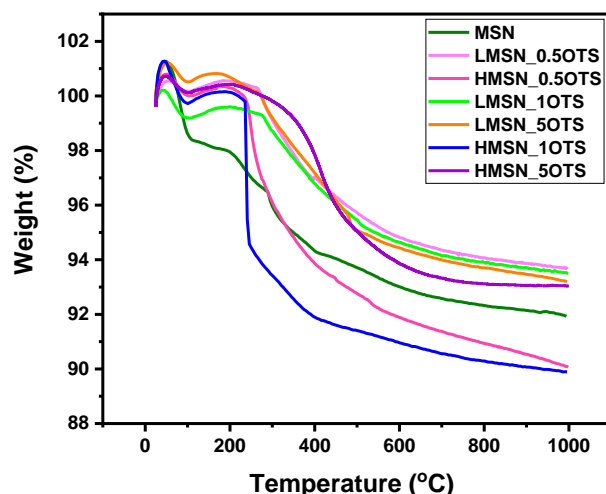


Figure 4.34: TGA of unfunctionalized MSN and functionalized LMSN and HMSN with different MTS content

Table 4.12: Organic content and estimated surface density of MTS for LMSN and HMSN

Sample	MTS concentration (w/w)	Organic content (wt.%)	Number of MTS molecules /nm ²
LMSN	0.5	1.78	0.96
	1	2.54	1.45
	5	5.44	3.53
HMSN	0.5	2.36	0.10
	1	3.64	0.16
	5	5.68	0.27

4.5.2 Influence of MTS functionalization on the TFN membrane performance

In order to investigate the influence of silane molecule size on the membrane performance, the separation performance of the MSN_TFN membranes was determined at different MTS concentrations and the results were compared to the performance of the corresponding MSN_TFN membranes with OTS – functionalized nanofillers.

As can be seen in **Figure 4.35**, in case of LMSN_TFN membranes, the permeance increased at low MTS concentration and then decreased at MTS concentrations higher than 1 w/w. The salt rejection more than 90% is still observed even at higher MTS concentrations. The membrane performance at 1 w/w MTS concentration is abnormal and not obey the general trend, which could be due to an experimental error. In case of HMSN, the permeance improved compared to the reference TFC membrane but is lower than the permeance of LMSN_TFN membranes. This was expected because the mesopore channels in LMSN are more hydrophilic than in HMSN. What was unexpected is the low rejection of HMSN_TFN membranes, which couldn't be explained. Nevertheless, the deprotonated silanol groups ($\equiv\text{Si-OH} \leftrightarrow \text{SiO}^- + \text{H}^+$) inside the mesopores may play a role in such performance. The number of unfunctionalized silanol groups in the mesopores of LMSN is much higher than in HMSN, which could provide the interior pores with a negative charge [223,224]. This may achieve better retention of the charged ions by a Donnan-like effect, which is not existing in HMSN_TFN membranes (with MTS functional group).

It is interesting to note that the permeance of the MSN_TFN membranes was significantly improved in case of MTS rather than the corresponding membranes with OTS (cf. **Figure 4.15**). It was attributed that the OTS molecules can block the pore entrance due to the large size of OTS molecule compared to the MTS molecules. As a result, MTS functionalization could allow water transport through the pore channels of MSN even at the high concentration level.

The lowest MTS concentration in case of LMSN_TFN membranes produced the highest separation performance, 94.5% salt rejection and $3.6 \text{ L/h}\cdot\text{m}^2\cdot\text{bar}$. This result confirms again that the lowest amount of hydrophobic functional groups is quite desired to increase the integrity of MSN inside the PA matrix. On the other hand, the permeance decreased at the higher concentration of MTS (cf. **Figure 4.35**). The reason could be attributed to the increased hydrophobicity of the nanofillers internal pores which couldn't be tested.

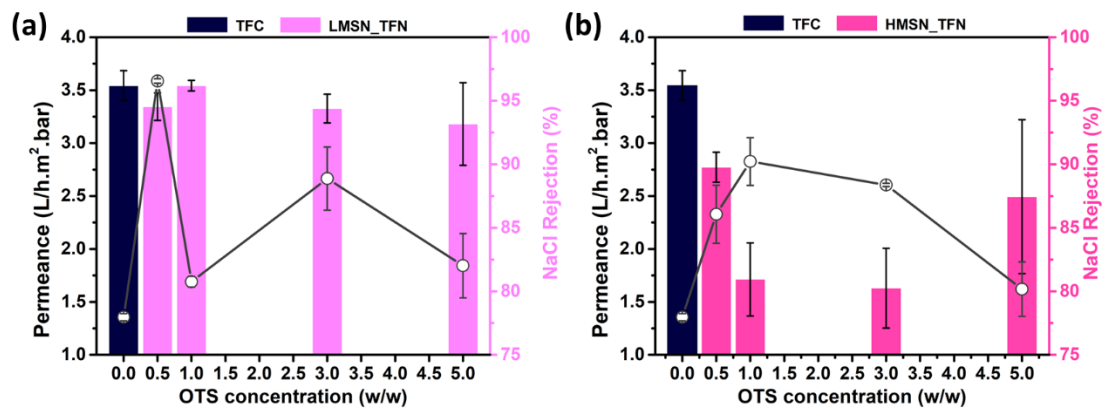


Figure 4.35: Effect of MTS concentration during MSN functionalization on the permeability and NaCl rejection of TFN membranes prepared at NPs loading of 0.01 w/v%: a) LMSN and b) HMSN

The separation performance of the LMSN_TFN membranes at 0.5 w/w MTS was studied at different LMSN loading. The result, in **Figure 4.36**, shows that both permeance and salt rejection are higher at the low NPs loading, the maximum at 0.005 w/v%, then the membranes revealed lower performance at higher loading. This is very similar to the performance in case of LMSN_TFN with OTS (cf. **Figure 4.19**). The low separation performance beyond 0.005 w/v% NPs loading, was attributed to the aggregation of the nanofiller which led to more exposure at the outer membrane surface along with increasing density of defects in the PA layer (see **Section 4.2.3**).

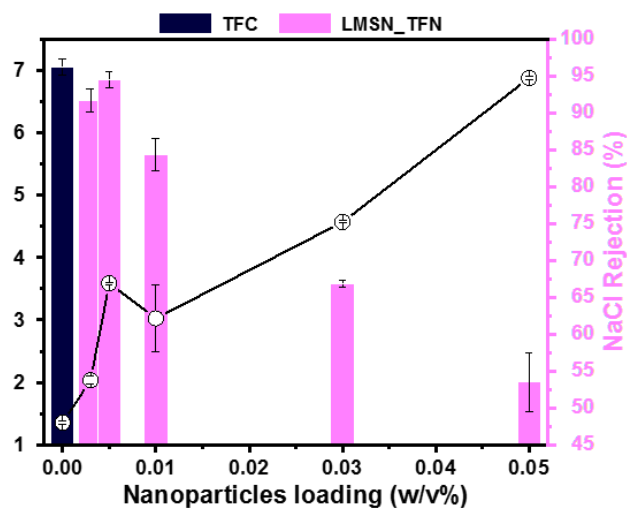


Figure 4.36: Effect of LMSN (MTS concentration during MSN functionalization 0.5 w/w) loading in TFN membranes on permeability and NaCl rejection during desalination

In order to know the influence of the MSN functionalization with smaller size silane (MTS) on the respective TFN membranes, the long-term separation performance was studied (for 240 h). As can be seen in **Figure 4.37**, the permeance increased in the first 120 h in aqueous NaCl

solution at pH 5 by $0.55 \text{ L/h}\cdot\text{m}^2\cdot\text{bar}$. Then the solution with a pH 9 was used and a more pronounced increase was visible in the next 120 h. The increase in permeance here is $1.5 \text{ L/h}\cdot\text{m}^2\cdot\text{bar}$. At the same time a decrease of the retention is visible. In the acidic feed solution, the decrease is rather small (-1.8%), while the alkaline solution has a stronger influence on the retention of the membrane (-7.5%) which could be explained by the dissolution of the particles. This slightly less stability of the LMSN_TFN membranes with MTS than the same membrane with OTS could be because of the long alkyl chain of OTS which can provide MSN with higher hydrophobic properties than the only CH_3 in MTS. The more hydrophobic nanofillers, the better distribution and integration inside the PA layer. This is observed along the rejection values of MSN_TFN membranes with OTS are always better than the corresponding membranes with MTS.

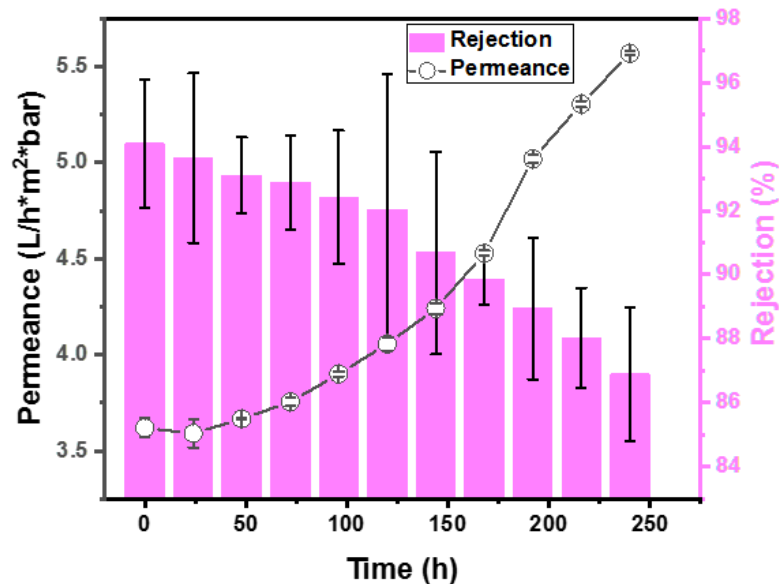


Figure 4.37: Long-term separation performance of LMSN_TFN membranes with 0.5 w/w MTS for 120 h at pH 5 and 120 h at pH 9 using the same membrane

Chapter 5

5. Conclusions

The thin film nanocomposite (TFN) membranes received increasing attention over the last decade. The main purpose of these membranes is to obtain more enhanced solvent permeability than TFC membranes, without compromising solute rejection. This improved permeance is achieved by imbedding NPs (mostly porous) in the selective layer.

Throughout this project, MSN was used as nanofillers for the PA TFN membranes because their highly ordered structure and due to their simple synthesis and modification. MSN were synthesized using sol-gel method in presence of TEOS as a silica precursor and CTAB as a template surfactant. The particle diameter was controlled by optimizing the CTAB/TEOS molar ratio. MSN sample prepared at CTAB/TEOS = 0.1 was selected to be the optimum which had a particle diameter of ≈ 80 nm and pore diameter ≈ 3.3 nm. MSN were then functionalized with OTS. The functionalization was successfully controlled to modify only the external surface of NPs (LMSN) or both external and internal pores surfaces (HMSN).

Nitrogen adsorption measurement was utilized to investigate the influence of OTS functionalization on the S_{BET} , d_p and V_p of MSN. It was found that all of them decrease by increasing the OTS concentration, especially in case of HMSN, because the grafting occurred in absence of surfactant which led to functionalizing the internal pores causing pore blocking. This blocking was explained through two scenarios; first OTS can truly fill the pores completely or second, it just closes the pore entrance. Both scenarios can result in decreasing the nitrogen adsorption. TGA was also carried out to evaluate the thermal stability of the synthesized MSN and to estimate the amount of OTS grafted. It was found that, at high concentration of OTS, a self assembled monolayer can be formed on the surface of MSN. However, the number of OTS molecule/nm² for LMSN is always higher than HMSN at the same OTS concentration because the lower surface area exposed to the functionalization in case of LMSN compared to the higher surface area in case of HMSN. Other characterization methods were employed such as SEM, TEM and XRD to study the morphology and porous structure of the obtained particles and FTIR to qualitatively confirm the occurrence of functionalization.

The functionalized NPs were used thereafter as nanofillers to prepare TFN membranes. The nanofillers were impregnated into the polyamide film in a separate step between MPD soaking of the PES support and TMC addition during the IP process.

Physicochemical properties of TFC and TFN membranes were characterized with SEM, ATR-FTIR, zeta potential and contact angle measurements. The initial performance of the TFN membranes was characterized using RO filtration of pure water, pure ethanol and 2000 ppm NaCl solution.

Overall, because the hydrophobic nature of OTS, it was found that, the more OTS concentration in the functionalized nanofillers, the more decline in water permeability. Consequently, the pure water permeability of LMSN_TFN membranes was always higher than HMSN_TFN membranes at the same OTS concentration and NPs loading. In case of LMSN, the hydrophilicity of the internal pores was preserved which facilitate the transport of water or ethanol. Due to the internal pore functionalization in HMSN, the pure water permeability was declined, and ethanol permeability was improved compared to the reference TFC membrane. This is most likely due to the hydrophobic properties of OTS inside the pores, creating resistance toward the flow of water, but not to the flow of ethanol. The influence of NPs loading on the separation performance was also studied, the results showed an improvement of permeance and salt rejection was observed at lower loading while at higher loading the performance deteriorated. This was attributed to the good integration of nanofillers and better coverage with the PA layer was achieved at the low loading, that was also confirmed by SEM, zeta potential and contact angle measurements. LMSN_TFN membranes at LMSN loading of 0.005 w/v% and OTS concentration 0.5 w/w produced about 65% higher permeance than the reference TFC membrane without sacrificing the membrane selectivity (NaCl rejection > 95%).

The effect of OTS functionalization on the dissolution of MSN in aqueous solution at different pH values was also studied. The dissolved silica concentration was spectrophotometrically determined using molybdsilicate method. The dissolution of the unfunctionalized MSN was observed at both pH values. Nevertheless, the dissolution rate was higher at pH 9 due to the more effective deprotonation of silicic acid to highly soluble silicate ions. OTS functionalization significantly improved the stability of MSN against dissolution in aqueous phase, particularly at pH 5. It was observed from XRD and TEM data that the mesoporous structure was strongly influenced by the dissolution of the unfunctionalized MSN; the mesopore content was reduced which was also confirmed by results from nitrogen adsorption isotherms, revealing reduction of S_{BET} , d_p and V_p values after partial dissolution. In contrast, nitrogen adsorption data for LMSN and HMSN revealed only minor changes, confirming the effect of the protective organic layer on the particle surface in terms of significantly improving nanofiller stability against dissolution effects.

Furthermore, the influence of nanofiller dissolution on the stability of the corresponding TFN membranes was investigated. Overall, LMSN_TFN and HMSN_TFN membranes revealed a noteworthy improved performance stability compared to the MSN_TFN membranes. In the latter membranes, the agglomeration of hydrophilic MSN in the PA barrier layer did not only lead to reducing the overall separation performance as indicated by lower salt rejection,

but also apparently promoted the dissolution of the embedded nanofiller. This created mesoporous defects in the barrier layer which had been identified by filtration of dextran solutions.

Differences between the two types of OTS-functionalized nanofillers had also been identified and explained based on results of structure analyses. LMSN_TFN membranes showed the largest improvement in the initial separation performance among the all tested membranes (higher permeance at the same salt rejection compared to the reference TFC membrane without nanofiller), and the best long-term stability compared to the HMSN_TFN and MSN_TFN membranes.

It has been also shown that using MTS as a very small silane molecule in the functionalization of MSN instead of the large OTS molecule has a positive impact on the permeance of the respective TFN membranes. The small size of MTS did not show any pore blocking during functionalization of the interior pores even at the high MTS concentration, which could explain why the permeance is always higher compared to the membranes with OTS. On the other hand, the rejection values of LMSN_TFN or HMSN_TFN membranes with OTS are always higher than the corresponding membranes with MTS. This could be attributed to the long alkyl chain of OTS, which can provide MSN with higher hydrophobic properties than the only CH₃ in MTS. The more hydrophobic nanofillers, the better distribution and integration inside the PA layer. Therefore, more robust PA layer.

To conclude, the obtained results from this PhD thesis imply that, the well-designed organic protective layers on such porous nanofillers can simultaneously enhance the intrinsic separation performance, as well as the stability of MSN-containing TFN membranes, in particular at pH 5. However, it is not recommended to utilize these membranes for long-term filtration of the feed solution at higher pH to avoid the instability of the nanofillers which affect the separation performance.

6. Outlook

Based on the conclusions of this work and challenges faced during the course of this research and experiments, the following suggestions can be taken into account:

- Further experiments with other alkyltrichlorosilanes with different alkylchain length may provide better understanding for the relation between the kind of used silane and the stability of both nanofillers and TFN membranes.
- The influence of other filler properties includes the pore size, the particle size, and the shape, on the membrane permeability and selectivity need to be studied to get a more comprehensive picture about the role of nanofillers on separation.
- As a direct method to understand the separation mechanism of the TFN membranes and investigate the role of the porous nanofillers on water transport, positron annihilation spectroscopy can also offer additional understanding in the layered structure and providing some information about the voids which could be created between the PA and the inserted nanofillers [63,225]. This can be achieved by comparing three different membranes, the TFC membrane without any nanofillers inside, one TFN membrane containing nonporous silica functionalized with the same silane molecules and one TFN membranes containing LMSN.
- Additionally, it would be interesting to quantify the amount of incorporated fillers. It could be possible to use a highly sensitive analytical inductively coupled plasma (ICP) to determine the nanofillers concentration. To do this, the TFN membrane is allowed to be thermally treated until ignite the organic matrix and the inorganic residue is analyzed using ICP. This inorganic residue is an indicator of how much fillers were truly incorporated in the barrier layer.
- The high pure ethanol permeability obtained by the LMSN_TFN and HMSN_TFN membranes is quite impressive and indicate that these membranes may be attractive in organic solvent nanofiltration (OSN). However, using PES as a support could limit this application because it is not tolerant to many solvents and can be dissolve or swill in their presence. Using ceramic membrane as a support for TFN membranes is very new idea and it is expected to provide the membranes with the required chemical stability toward the various organic solvents [226].

7. References

- [1] B.M. Popkin, K.E. D’Anci, I.H. Rosenberg, Water, hydration, and health, *Nutrition Reviews*. 68 (2010) 439–458. doi:10.1111/j.1753-4887.2010.00304.x.
- [2] S. Burn, M. Hoang, D. Zarzo, F. Olewniak, E. Campos, B. Bolto, O. Barron, Desalination techniques — A review of the opportunities for desalination in agriculture, *Desalination*. 364 (2015) 2–16. doi:10.1016/J.DESAL.2015.01.041.
- [3] R.F. Service, Desalination freshens up, *Science*. 313 (2006) 1088 LP-1090. doi:10.1126/science.313.5790.1088.
- [4] WWAP, The united nations world water development report 2018: Nature-based solutions for water, (2018).
- [5] M. Shatat, M. Worall, S. Riffat, Opportunities for solar water desalination worldwide: Review, *Sustainable Cities and Society*. 9 (2013) 67–80. doi:10.1016/j.scs.2013.03.004.
- [6] G. Meerganz Von Medeazza, Water desalination as a long-term sustainable solution to alleviate global freshwater scarcity? A North-South approach, *Desalination*. 169 (2004) 287–301. doi:10.1016/J.DESA1.2004.04.001.
- [7] A. Ali, R.A. Tufa, F. Macedonio, E. Curcio, E. Drioli, Membrane technology in renewable-energy-driven desalination, *Renewable and Sustainable Energy Reviews*. 81 (2018) 1–21. doi:10.1016/j.rser.2017.07.047.
- [8] W.H. Organisation, Silver in drinking water: Background document for the development of WHO guidelines for drinking water quality, (1996).
- [9] W.H. Organisation, Guidelines for drinking-water quality, incorporating first and second addenda, (n.d.).
- [10] S.F. Anis, R. Hashaikeh, N. Hilal, Reverse osmosis pretreatment technologies and future trends: A comprehensive review, *Desalination*. 452 (2019) 159–195. doi:10.1016/j.desal.2018.11.006.
- [11] M. Elimelech, W.A. Phillip, The future of seawater desalination: Energy, technology, and the environment, *Science*. 333 (2011) 712 LP-717. <http://science.sciencemag.org/content/333/6043/712.abstract>.
- [12] K.P. Lee, T.C. Arnot, D. Mattia, A review of reverse osmosis membrane materials for desalination-Development to date and future potential, *Journal of Membrane Science*. 370 (2011) 1–22. doi:10.1016/j.memsci.2010.12.036.
- [13] M. Li, Reducing specific energy consumption in Reverse Osmosis (RO) water desalination: An analysis from first principles, *Desalination*. 276 (2011) 128–135. doi:10.1016/J.DESAL.2011.03.031.
- [14] G.-R. Xu, J.-N. Wang, C.-J. Li, Strategies for improving the performance of the polyamide thin film composite (PA-TFC) reverse osmosis (RO) membranes: Surface modifications and nanoparticles incorporations, *Desalination*. 328 (2013) 83–100. doi:10.1016/J.DESAL.2013.08.022.
- [15] B.-H. Jeong, E.M.V. Hoek, Y. Yan, A. Subramani, X. Huang, G. Hurwitz, A.K. Ghosh, A. Jawor, Interfacial polymerization of thin film nanocomposites: A new concept for reverse osmosis membranes, *Journal of Membrane Science*. 294 (2007) 1–7. doi:10.1016/J.MEMSCI.2007.02.025.
- [16] W.J. Lau, S. Gray, T. Matsuura, D. Emadzadeh, J. Paul Chen, A.F. Ismail, A review on polyamide thin film nanocomposite (TFN) membranes: History, applications, challenges and approaches, *Water Research*. 80 (2015) 306–324. doi:10.1016/j.watres.2015.04.037.
- [17] J. Yin, E.S. Kim, J. Yang, B. Deng, Fabrication of a novel thin-film nanocomposite (TFN) membrane containing MCM-41 silica nanoparticles (NPs) for water purification, *Journal of Membrane Science*. 423–424 (2012) 238–246. doi:10.1016/j.memsci.2012.08.020.
- [18] L. Liu, G. Zhu, Z. Liu, C. Gao, Effect of MCM-48 nanoparticles on the performance of

- thin film nanocomposite membranes for reverse osmosis application, *Desalination*. 394 (2016) 72–82. doi:10.1016/J.DESAL.2016.04.028.
- [19] H. Dong, X.-Y. Qu, L. Zhang, L.-H. Cheng, H.-L. Chen, C.-J. Gao, Preparation and characterization of surface-modified zeolite-polyamide thin film nanocomposite membranes for desalination, *Desalination and Water Treatment*. 34 (2011) 6–12.
- [20] C.P. Guthrie, E.J. Reardon, Metastability of MCM-41 and Al-MCM-41, *The Journal of Physical Chemistry A*. 112 (2008) 3386–3390. doi:10.1021/jp710434y.
- [21] A.L.-T. Pham, D.L. Sedlak, F.M. Doyle, Dissolution of mesoporous silica supports in aqueous solutions: Implications for mesoporous silica-based water treatment processes, *Applied Catalysis B: Environmental*. 126 (2012) 258–264. doi:10.1016/J.APCATB.2012.07.018.
- [22] W.L. Ang, A.W. Mohammad, N. Hilal, C.P. Leo, A review on the applicability of integrated/hybrid membrane processes in water treatment and desalination plants, *Desalination*. 363 (2015) 2–18. doi:https://doi.org/10.1016/j.desal.2014.03.008.
- [23] A. Gil, L.A. Galeano, M.Á. Vicente, Applications of advanced oxidation processes (AOPs) in drinking water treatment, 1st ed., Springer, 2019. <http://gen.lib.rus.ec/book/index.php?md5=8761c7132c744368411c2e9f796aec69>.
- [24] M.M. Pendergast, E.M.V. V Hoek, A review of water treatment membrane nanotechnologies, *Energy & Environmental Science*. 4 (2011) 1946–1971. doi:10.1039/C0EE00541J.
- [25] C. Binnie, M. Kimber, Basic water treatment, The Royal Society of Chemistry, 2009.
- [26] R.E. Kesting, The four tiers of structure in integrally skinned phase inversion membranes and their relevance to the various separation regimes, *Journal of Applied Polymer Science*. 41 (1990) 2739–2752. doi:10.1002/app.1990.070411120.
- [27] D.M. Warsinger, S. Chakraborty, E.W. Tow, M.H. Plumlee, C. Bellona, S. Loutatidou, L. Karimi, A.M. Mikelonis, A. Achilli, A. Ghassemi, L.P. Padhye, S.A. Snyder, S. Curcio, C.D. Vecitis, H.A. Arafat, J.H. Lienhard, A review of polymeric membranes and processes for potable water reuse, *Progress in Polymer Science*. 81 (2018) 209–237. doi:10.1016/j.progpolymsci.2018.01.004.
- [28] M. Ulbricht, Advanced functional polymer membranes, *Polymer*. 47 (2006) 2217–2262. doi:10.1016/j.polymer.2006.01.084.
- [29] M.A. Shannon, P.W. Bohn, M. Elimelech, J.G. Georgiadis, B.J. Mariñas, A.M. Mayes, Science and technology for water purification in the coming decades, *Nature*. 452 (2008) 301–310. doi:10.1038/nature06599.
- [30] S.M. Dittami, S. Heesch, J.L. Olsen, J. Collén, Transitions between marine and freshwater environments provide new clues about the origins of multicellular plants and algae, *Journal of Phycology*. 53 (2017) 731–745. doi:10.1111/jpy.12547.
- [31] L. Henthorne, B. Boysen, State-of-the-art of reverse osmosis desalination pretreatment, *Desalination*. 356 (2015) 129–139. doi:10.1016/j.desal.2014.10.039.
- [32] S. Bhojwani, K. Topolski, R. Mukherjee, D. Sengupta, M.M. El-Halwagi, Technology review and data analysis for cost assessment of water treatment systems, *Science of the Total Environment*. 651 (2019) 2749–2761. doi:10.1016/j.scitotenv.2018.09.363.
- [33] S. Loutatidou, B. Chalermthai, P.R. Marpu, H.A. Arafat, Capital cost estimation of RO plants: GCC countries versus southern Europe, *Desalination*. 347 (2014) 103–111. doi:10.1016/j.desal.2014.05.033.
- [34] L.F. Greenlee, D.F. Lawler, B.D. Freeman, B. Marrot, P. Moulin, Reverse osmosis desalination: Water sources, technology, and today’s challenges, *Water Research*. 43 (2009) 2317–2348. doi:10.1016/J.WATRES.2009.03.010.
- [35] M.A. Abdelkareem, M. El Haj Assad, E.T. Sayed, B. Soudan, Corrigendum to “Recent progress in the use of renewable energy sources to power water desalination plants” [*Desalination* 435(2018) 97–113](S0011916417321306)(10.1016/j.desal.2017.11.018),

- Desalination. 444 (2018) 178. doi:10.1016/j.desal.2018.05.003.
- [36] T.Y. Cath, A.E. Childress, M. Elimelech, Forward osmosis: Principles, applications, and recent developments, *Journal of Membrane Science*. 281 (2006) 70–87. doi:10.1016/J.MEMSCI.2006.05.048.
- [37] D.L. Shaffer, J.R. Werber, H. Jaramillo, S. Lin, M. Elimelech, Forward osmosis: Where are we now?, *Desalination*. 356 (2015) 271–284. doi:10.1016/J.DESAL.2014.10.031.
- [38] R.W. Baker, Reverse Osmosis, in: *Membrane Technology and Applications*, 2004. doi:doi:10.1002/0470020393.ch5.
- [39] S. Kasemset, A. Lee, D.J. Miller, B.D. Freeman, M.M. Sharma, Effect of polydopamine deposition conditions on fouling resistance, physical properties, and permeation properties of reverse osmosis membranes in oil/water separation, *Journal of Membrane Science*. 425–426 (2013) 208–216. doi:10.1016/J.MEMSCI.2012.08.049.
- [40] M. Vourch, B. Balannec, B. Chaufer, G. Dorange, Treatment of dairy industry wastewater by reverse osmosis for water reuse, *Desalination*. 219 (2008) 190–202. doi:10.1016/J.DESAL.2007.05.013.
- [41] C.E. Reid, E.J. Breton, Water and ion flow across cellulosic membranes, *J. Appl. Polym. Sci.* 1 (1959) 133–143. doi:10.1002/app.1959.070010202.
- [42] S. Loeb, S. Sourirajan, Sea water demineralization by means of an osmotic membrane, in: *Saline Water Conversion—II*, American Chemical Society, 1963: pp. 117-132 SE–9. doi:doi:10.1021/ba-1963-0038.ch009.
- [43] K.J. Edgar, C.M. Buchanan, J.S. Debenham, P.A. Rundquist, B.D. Seiler, M.C. Shelton, D. Tindall, Advances in cellulose ester performance and application, *Progress in Polymer Science*. 26 (2001) 1605–1688. doi:10.1016/S0079-6700(01)00027-2.
- [44] H.H. Hoehn, J.W. Richter, Aromatic polyimide, polyester and polyamide separation membranes, US Patent USRE30351 E, 1980.
- [45] L. Credali, P. Parrini, Properties of piperazine homopolyamide films, *Polymer*. 12 (1971) 717–729. doi:10.1016/0032-3861(71)90087-5.
- [46] R.G. Sudak, Reverse osmosis, in: *Handbook of Industrial Membrane Technology*, Noyes Publication, New Jersey, 1990.
- [47] G. Congjie, Development and extension of seawater desalination by reverse osmosis, *Chinese Journal of Oceanology and Limnology*. 21 (2003) 40–45. doi:10.1007/BF02842760.
- [48] W. Yan, Z. Wang, J. Wu, S. Zhao, J. Wang, S. Wang, Enhancing the flux of brackish water TFC RO membrane by improving support surface porosity via a secondary pore-forming method, *Journal of Membrane Science*. 498 (2016) 227–241. doi:10.1016/J.MEMSCI.2015.10.029.
- [49] J.E. Cadotte, Reverse osmosis membrane, US Patent US4039440 A, 1977.
- [50] J.E. Cadotte, Interfacially synthesized reverse osmosis membrane, US Patent 4277344, 1981.
- [51] R.E. Larson, J.E. Cadotte, R.J. Petersen, The FT-30 seawater reverse osmosis membrane--element test results, *Desalination*. 38 (1981) 473–483. doi:10.1016/S0011-9164(00)86092-0.
- [52] C. Kong, T. Shintani, T. Tsuru, “Pre-seeding”-assisted synthesis of a high performance polyamide-zeolite nanocomposite membrane for water purification, *New Journal of Chemistry*. 34 (2010) 2101–2104. doi:10.1039/c0nj00581a.
- [53] G.M. Geise, H.-S. Lee, D.J. Miller, B.D. Freeman, J.E. McGrath, D.R. Paul, Water purification by membranes: The role of polymer science, *Journal of Polymer Science Part B: Polymer Physics*. 48 (2010) 1685–1718. doi:10.1002/polb.22037.
- [54] L. Ni, J. Meng, X. Li, Y. Zhang, Surface coating on the polyamide TFC RO membrane for chlorine resistance and antifouling performance improvement, *Journal of Membrane Science*. 451 (2014) 205–215. doi:10.1016/J.MEMSCI.2013.09.040.

- [55] P.W. Morgan, *Condensation polymers: by interfacial and solution methods*, 1st ed., Interscience Publishers, New York, 1965.
- [56] H. Park, Y. Jung, S. Hong, Y. Kwon, Effects of interfacial polymerization conditions on performance of poly amide reverse osmosis membranes and optimization of polymerization conditions by statistical methodology, *Desalination and Water Treatment*. 74 (2017) 1–11.
- [57] M.J.T. Raaijmakers, N.E. Benes, Current trends in interfacial polymerization chemistry, *Progress in Polymer Science*. 63 (2016) 86–142. doi:10.1016/J.PROGPOLYMSCI.2016.06.004.
- [58] V. Freger, Kinetics of film formation by interfacial polycondensation, *Langmuir*. 21 (2005) 1884–1894. doi:10.1021/la048085v.
- [59] T.D. Matthews, H. Yan, D.G. Cahill, O. Coronell, B.J. Mariñas, Growth dynamics of interfacially polymerized polyamide layers by diffuse reflectance spectroscopy and Rutherford backscattering spectrometry, *Journal of Membrane Science*. 429 (2013) 71–80. doi:10.1016/J.MEMSCI.2012.11.040.
- [60] V. Freger, Nanoscale heterogeneity of polyamide membranes formed by interfacial polymerization, *Langmuir*. 19 (2003) 4791–4797. doi:10.1021/la020920q.
- [61] A. Nowbahar, V. Mansard, J.M. Mecca, M. Paul, T. Arrowood, T.M. Squires, Measuring interfacial polymerization kinetics using microfluidic interferometry, *Journal of the American Chemical Society*. 140 (2018) 3173–3176. doi:10.1021/jacs.7b12121.
- [62] B. Ukrainsky, G.Z. Ramon, Temperature measurement of the reaction zone during polyamide film formation by interfacial polymerization, *Journal of Membrane Science*. 566 (2018) 329–335. doi:10.1016/J.MEMSCI.2018.09.011.
- [63] S.H. Kim, S.-Y.Y. Kwak, T. Suzuki, Positron annihilation spectroscopic evidence to demonstrate the flux-enhancement mechanism in morphology-controlled thin-film composite (TFC) membrane, *Environmental Science & Technology*. 39 (2005) 1764–1770. doi:10.1021/es049453k.
- [64] W.R. Bowen, J.S. Welfoot, Modelling the performance of membrane nanofiltration—critical assessment and model development, *Chemical Engineering Science*. 57 (2002) 1121–1137. doi:10.1016/S0009-2509(01)00413-4.
- [65] K. Košutić, L. Kaštelan-Kunst, B. Kunst, Porosity of some commercial reverse osmosis and nanofiltration polyamide thin-film composite membranes, *Journal of Membrane Science*. 168 (2000) 101–108. doi:10.1016/S0376-7388(99)00309-9.
- [66] S.M.J. Zaidi, F. Fadhillah, Z. Khan, A.F. Ismail, Salt and water transport in reverse osmosis thin film composite seawater desalination membranes, *Desalination*. 368 (2015) 202–213. doi:10.1016/J.DESAL.2015.02.026.
- [67] J.G. Wijmans, R.W. Baker, The solution-diffusion model: a review, *Journal of Membrane Science*. 107 (1995) 1–21. doi:10.1016/0376-7388(95)00102-I.
- [68] J. Wang, D.S. Dlamini, A.K. Mishra, M.T.M. Pendergast, M.C.Y. Wong, B.B. Mamba, V. Freger, A.R.D. Verliefde, E.M.V. Hoek, A critical review of transport through osmotic membranes, *Journal of Membrane Science*. 454 (2014) 516–537. doi:10.1016/J.MEMSCI.2013.12.034.
- [69] C. Bartels, R. Franks, S. Rybar, M. Schierach, M. Wilf, The effect of feed ionic strength on salt passage through reverse osmosis membranes, *Desalination*. 184 (2005) 185–195. doi:10.1016/J.DESAL.2005.04.032.
- [70] J.M. Peeters, J.P. Boom, M.H. Mulder, H. Strathmann, Retention measurements of nanofiltration membranes with electrolyte solutions, *Journal of Membrane Science*. 145 (1998) 199–209. doi:10.1016/S0376-7388(98)00079-9.
- [71] W. Zhou, L. Song, Experimental study of water and salt fluxes through reverse osmosis membranes, *Environmental Science & Technology*. 39 (2005) 3382–3387. doi:10.1021/es0403561.

- [72] M. Roux, M. Bloom, Ca^{2+} , Mg^{2+} , Li^+ , Na^+ , and K^+ distributions in the headgroup region of binary membranes of phosphatidylcholine and phosphatidylserine as seen by deuterium NMR., *Biochemistry*. 29 (1990) 7077–7089.
- [73] J. Mattai, H. Hauser, R.A. Demel, G.G. Shipley, Interactions of metal ions with phosphatidylserine bilayer membranes: effect of hydrocarbon chain unsaturation, *Biochemistry*. 28 (1989) 2322–2330.
- [74] R.W. Baker, *Membrane Technology and Applications*, 2nd ed., John Wiley & Sons, Ltd, 2004.
- [75] R.R. Sharma, R. Agrawal, S. Chellam, Temperature effects on sieving characteristics of thin-film composite nanofiltration membranes: pore size distributions and transport parameters, *Journal of Membrane Science*. 223 (2003) 69–87. doi:10.1016/S0376-7388(03)00310-7.
- [76] A.E. Childress, M. Elimelech, Relating nanofiltration membrane performance to membrane charge (electrokinetic) characteristics, *Environmental Science & Technology*. 34 (2000) 3710–3716. doi:10.1021/es0008620.
- [77] Z. Chen, K. Ito, H. Yanagishita, N. Oshima, R. Suzuki, Y. Kobayashi, Correlation study between free-volume holes and molecular separations of composite membranes for reverse osmosis processes by means of variable-energy positron annihilation techniques, *The Journal of Physical Chemistry C*. 115 (2011) 18055–18060. doi:10.1021/jp203888m.
- [78] T. Fujioka, B.E. O'Rourke, K. Michishio, Y. Kobayashi, N. Oshima, H. Kodamatani, T. Shintani, L.D. Nghiem, Transport of small and neutral solutes through reverse osmosis membranes: Role of skin layer conformation of the polyamide film, *Journal of Membrane Science*. 554 (2018) 301–308. doi:10.1016/j.memsci.2018.02.069.
- [79] V. Freger, Swelling and morphology of the skin layer of polyamide composite membranes: An atomic force microscopy study, *Environmental Science & Technology*. 38 (2004) 3168–3175. doi:10.1021/es034815u.
- [80] H. Yan, X. Miao, J. Xu, G. Pan, Y. Zhang, Y. Shi, M. Guo, Y. Liu, The porous structure of the fully-aromatic polyamide film in reverse osmosis membranes, *Journal of Membrane Science*. 475 (2015) 504–510. doi:10.1016/j.memsci.2014.10.052.
- [81] A.K. Ghosh, B.H. Jeong, X. Huang, E.M.V. Hoek, Impacts of reaction and curing conditions on polyamide composite reverse osmosis membrane properties, *Journal of Membrane Science*. 311 (2008) 34–45. doi:10.1016/j.memsci.2007.11.038.
- [82] J. Muscatello, E.A. Müller, A.A. Mostofi, A.P. Sutton, Multiscale molecular simulations of the formation and structure of polyamide membranes created by interfacial polymerization, *Journal of Membrane Science*. 527 (2017) 180–190. doi:10.1016/J.MEMSCI.2016.11.024.
- [83] J. Xu, H. Yan, Y. Zhang, G. Pan, Y. Liu, The morphology of fully-aromatic polyamide separation layer and its relationship with separation performance of TFC membranes, *Journal of Membrane Science*. 541 (2017) 174–188. doi:10.1016/j.memsci.2017.06.057.
- [84] A.K. Ghosh, E.M.V. Hoek, Impacts of support membrane structure and chemistry on polyamide–polysulfone interfacial composite membranes, *Journal of Membrane Science*. 336 (2009) 140–148. doi:10.1016/J.MEMSCI.2009.03.024.
- [85] T. Fujioka, N. Oshima, R. Suzuki, W.E. Price, L.D. Nghiem, Probing the internal structure of reverse osmosis membranes by positron annihilation spectroscopy: Gaining more insight into the transport of water and small solutes, *Journal of Membrane Science*. 486 (2015) 106–118. doi:10.1016/j.memsci.2015.02.007.
- [86] L. Song, M. Elimelech, Theory of concentration polarization in crossflow filtration, *Journal of the Chemical Society, Faraday Transactions*. 91 (1995) 3389–3398. doi:10.1039/FT9959103389.
- [87] W.J. Lau, A.F. Ismail, N. Misdan, M.A. Kassim, A recent progress in thin film composite

- membrane: A review, *Desalination*. 287 (2012) 190–199.
doi:10.1016/J.DESAL.2011.04.004.
- [88] M. Liu, C. Yu, Y. Wu, Z. Lü, S. Yu, C. Gao, In situ modification of polyamide reverse osmosis membrane module for improved fouling resistance, *Chemical Engineering Research and Design*. 141 (2019) 402–412. doi:10.1016/J.CHERD.2018.11.009.
- [89] F. Perreault, M.E. Tousley, M. Elimelech, Thin-film composite polyamide membranes functionalized with biocidal graphene oxide nanosheets, *Environmental Science and Technology Letters*. 1 (2013) 71–76. doi:10.1021/ez4001356.
- [90] H. Maddah, A. Chogle, Biofouling in reverse osmosis: phenomena, monitoring, controlling and remediation, *Applied Water Science*. 7 (2017) 2637–2651. doi:10.1007/s13201-016-0493-1.
- [91] A. Matin, Z. Khan, S.M.J. Zaidi, M.C. Boyce, Biofouling in reverse osmosis membranes for seawater desalination: Phenomena and prevention, *Desalination*. 281 (2011) 1–16. doi:10.1016/J.DESAL.2011.06.063.
- [92] A.F. Ismail, M. Padaki, N. Hilal, T. Matsuura, W.J. Lau, Thin film composite membrane — Recent development and future potential, *Desalination*. 356 (2015) 140–148. doi:10.1016/J.DESAL.2014.10.042.
- [93] A. Akbari, E. Aliyarizadeh, S.M. Mojallali Rostami, M. Homayoonfal, Novel sulfonated polyamide thin-film composite nanofiltration membranes with improved water flux and anti-fouling properties, *Desalination*. 377 (2016) 11–22. doi:10.1016/J.DESAL.2015.08.025.
- [94] H. Wu, X.L. Chen, X. Huang, H.M. Ruan, Y.L. Ji, L.F. Liu, C.J. Gao, A novel semi-aromatic polyamide TFC reverse osmosis membrane fabricated from a dendritic molecule of trimesoylamidoamine through a two-step amine-immersion mode, *RSC Advances*. 7 (2017) 39127–39137. doi:10.1039/c7ra07298h.
- [95] B. Khorshidi, T. Thundat, B.A. Fleck, M. Sadrzadeh, Thin film composite polyamide membranes: parametric study on the influence of synthesis conditions, *RSC Advances*. 5 (2015) 54985–54997. doi:10.1039/c5ra08317f.
- [96] R. Ma, Y. Ji, X. Weng, Q. An, C. Gao, High-flux and fouling-resistant reverse osmosis membrane prepared with incorporating zwitterionic amine monomers via interfacial polymerization, *Desalination*. 381 (2016) 100–110. doi:10.1016/J.DESAL.2015.11.023.
- [97] Y. Xu, X. Gao, X.X. Wang, Q. Wang, Z. Ji, X.X. Wang, T. Wu, C. Gao, Highly and Stably Water Permeable Thin Film Nanocomposite Membranes Doped with MIL-101 (Cr) Nanoparticles for Reverse Osmosis Application, *Materials*. 9 (2016). doi:10.3390/ma9110870.
- [98] M. Liu, S. Yu, J. Tao, C. Gao, Preparation, structure characteristics and separation properties of thin-film composite polyamide-urethane seawater reverse osmosis membrane, *Journal of Membrane Science*. 325 (2008) 947–956. doi:10.1016/J.MEMSCI.2008.09.033.
- [99] J.R. Werber, S.K. Bull, M. Elimelech, Acyl-chloride quenching following interfacial polymerization to modulate the water permeability, selectivity, and surface charge of desalination membranes, *Journal of Membrane Science*. 535 (2017) 357–364. doi:10.1016/J.MEMSCI.2017.04.041.
- [100] I.M.A. ElSherbiny, R. Ghannam, A.S.G. Khalil, M. Ulbricht, Isotropic macroporous polyethersulfone membranes as competitive supports for high performance polyamide desalination membranes, *Journal of Membrane Science*. 493 (2015) 782–793. doi:10.1016/j.memsci.2015.05.064.
- [101] G. Xu, J. Xu, H. Feng, H. Zhao, S. Wu, Tailoring structures and performance of polyamide thin film composite (PA-TFC) desalination membranes via sublayers adjustment—a review, *Desalination*. 417 (2017) 19–35. doi:10.1016/J.DESAL.2017.05.011.

- [102] A. Tiraferri, M. Elimelech, Direct quantification of negatively charged functional groups on membrane surfaces, *Journal of Membrane Science*. 389 (2012) 499–508. doi:10.1016/J.MEMSCI.2011.11.018.
- [103] N. Misdan, A.F. Ismail, N. Hilal, Recent advances in the development of (bio)fouling resistant thin film composite membranes for desalination, *Desalination*. 380 (2016) 105–111. doi:10.1016/j.desal.2015.06.001.
- [104] E. Ostuni, R.G. Chapman, R.E. Holmlin, S. Takayama, G.M. Whitesides, A survey of structure–property relationships of surfaces that resist the adsorption of protein, *Langmuir*. 17 (2001) 5605–5620. doi:10.1021/la010384m.
- [105] S. Yu, G. Yao, B. Dong, H. Zhu, X. Peng, J. Liu, M. Liu, C. Gao, Improving fouling resistance of thin-film composite polyamide reverse osmosis membrane by coating natural hydrophilic polymer sericin, *Separation and Purification Technology*. 118 (2013) 285–293. doi:10.1016/J.SEPPUR.2013.07.018.
- [106] S. Azari, L. Zou, Using zwitterionic amino acid L-DOPA to modify the surface of thin film composite polyamide reverse osmosis membranes to increase their fouling resistance, *Journal of Membrane Science*. 401–402 (2012) 68–75.
- [107] P.H.H. Duong, K. Daumann, P.-Y. Hong, M. Ulbricht, S.P. Nunes, Interfacial polymerization of zwitterionic building blocks for high-flux nanofiltration membranes, *Langmuir*. (2018). doi:10.1021/acs.langmuir.8b00960.
- [108] Y. Zhang, Z. Wang, W. Lin, H. Sun, L. Wu, S. Chen, A facile method for polyamide membrane modification by poly(sulfobetaine methacrylate) to improve fouling resistance, *Journal of Membrane Science*. 446 (2013) 164–170. doi:10.1016/J.MEMSCI.2013.06.013.
- [109] J. Meng, Z. Cao, L. Ni, Y. Zhang, X. Wang, X. Zhang, E. Liu, A novel salt-responsive TFC RO membrane having superior antifouling and easy-cleaning properties, *Journal of Membrane Science*. 461 (2014) 123–129. doi:10.1016/J.MEMSCI.2014.03.017.
- [110] H.Z. Shafi, A. Matin, Z. Khan, A. Khalil, K.K. Gleason, Surface modification of reverse osmosis membranes with zwitterionic coatings: A potential strategy for control of biofouling, *Surface and Coatings Technology*. 279 (2015) 171–179.
- [111] M. Barboiu, Artificial water channels – incipient innovative developments, *Chemical Communications*. 52 (2016) 5657–5665. doi:10.1039/C6CC01724J.
- [112] Y. Zhao, A. Vararattanavech, X. Li, C. HélixNielsen, T. Vissing, J. Torres, R. Wang, A.G. Fane, C.Y. Tang, Effects of proteoliposome composition and draw solution types on separation performance of aquaporin-based proteoliposomes: implications for seawater desalination using aquaporin-based biomimetic membranes, *Environmental Science & Technology*. 47 (2013) 1496–1503.
- [113] X. Li, S. Chou, R. Wang, L. Shi, W. Fang, G. Chaitra, C.Y. Tang, J. Torres, X. Hu, A.G. Fane, Nature gives the best solution for desalination: Aquaporin-based hollow fiber composite membrane with superior performance, *Journal of Membrane Science*. 494 (2015) 68–77. doi:10.1016/J.MEMSCI.2015.07.040.
- [114] N. Ma, J. Wei, S. Qi, Y. Zhao, Y. Gao, C.Y. Tang, Nanocomposite substrates for controlling internal concentration polarization in forward osmosis membranes, *Journal of Membrane Science*. 441 (2013) 54–62. doi:10.1016/J.MEMSCI.2013.04.004.
- [115] K.C. Wong, P.S. Goh, A.F. Ismail, Gas separation performance of thin film nanocomposite membranes incorporated with polymethyl methacrylate grafted multi-walled carbon nanotubes, *International Biodeterioration and Biodegradation*. 102 (2015) 339–345. doi:10.1016/j.ibiod.2015.02.007.
- [116] R. Narayan, U.Y. Nayak, A.M. Raichur, S. Garg, Mesoporous silica nanoparticles: A comprehensive review on synthesis and recent advances, *Pharmaceutics*. 10 (2018). doi:10.3390/pharmaceutics10030118.
- [117] S.Y. Lee, H.J. Kim, R. Patel, S.J. Im, J.H. Kim, B.R. Min, Silver nanoparticles

- immobilized on thin film composite polyamide membrane: characterization, nanofiltration, antifouling properties, *Polymers for Advanced Technologies*. 18 (2007) 562–568. doi:10.1002/pat.918.
- [118] B. Rajaeian, A. Rahimpour, M.O. Tade, S. Liu, Fabrication and characterization of polyamide thin film nanocomposite (TFN) nanofiltration membrane impregnated with TiO₂ nanoparticles, *Desalination*. 313 (2013) 176–188. doi:10.1016/J.DESAL.2012.12.012.
- [119] Y. Fang, J.S. Duranceau, Study of the effect of nanoparticles and surface morphology on reverse osmosis and nanofiltration membrane productivity, *Membranes*. 3 (2013). doi:10.3390/membranes3030196.
- [120] P. Cay-Durgun, C. McCloskey, J. Konecny, A. Khosravi, M.L. Lind, Evaluation of thin film nanocomposite reverse osmosis membranes for long-term brackish water desalination performance, *Desalination*. 404 (2017) 304–312. doi:10.1016/J.DESAL.2016.10.014.
- [121] H. Dong, L. Zhao, L. Zhang, H. Chen, C. Gao, W.S. Winston Ho, High-flux reverse osmosis membranes incorporated with NaY zeolite nanoparticles for brackish water desalination, *Journal of Membrane Science*. 476 (2015) 373–383. doi:10.1016/J.MEMSCI.2014.11.054.
- [122] C. Van Goethem, R. Verbeke, S. Hermans, R. Bernstein, I.F.J.J. Vankelecom, Controlled positioning of MOFs in interfacially polymerized thin-film nanocomposites, *Journal of Materials Chemistry A*. 4 (2016) 16368–16376. doi:10.1039/C6TA05175H.
- [123] M. Kadhom, J. Yin, B. Deng, A thin film nanocomposite membrane with MCM-41 silica nanoparticles for brackish water purification, *Membranes*. 6 (2016) 50. doi:10.3390/membranes6040050.
- [124] M.E.A. Ali, L. Wang, X. Wang, X. Feng, Thin film composite membranes embedded with graphene oxide for water desalination, *Desalination*. 386 (2016) 67–76. doi:10.1016/J.DESAL.2016.02.034.
- [125] M. Fathizadeh, H.N. Tien, K. Khivantsev, Z. Song, F. Zhou, M. Yu, Polyamide/nitrogen-doped graphene oxide quantum dots (N-GOQD) thin film nanocomposite reverse osmosis membranes for high flux desalination, *Desalination*. 451 (2019) 125–132. doi:10.1016/J.DESAL.2017.07.014.
- [126] H.D. Lee, H.W. Kim, Y.H. Cho, H.B. Park, Experimental evidence of rapid water transport through carbon nanotubes embedded in polymeric desalination membranes, *Small*. 10 (2014) 2653–2660. doi:10.1002/sml.201303945.
- [127] M. Bao, G. Zhu, L. Wang, M. Wang, C. Gao, Preparation of monodispersed spherical mesoporous nanosilica-polyamide thin film composite reverse osmosis membranes via interfacial polymerization, *Desalination*. 309 (2013) 261–266. doi:10.1016/j.desal.2012.10.028.
- [128] A. Tiraferri, Y. Kang, E.P. Giannelis, M. Elimelech, Highly Hydrophilic Thin-Film Composite Forward Osmosis Membranes Functionalized with Surface-Tailored Nanoparticles, *ACS Applied Materials & Interfaces*. 4 (2012) 5044–5053. doi:10.1021/am301532g.
- [129] P.G. Ingole, M.I. Baig, W.K. Choi, H.K. Lee, Synthesis and characterization of polyamide/polyester thin-film nanocomposite membranes achieved by functionalized TiO₂ nanoparticles for water vapor separation, *Journal of Materials Chemistry A*. 4 (2016) 5592–5604. doi:10.1039/C6TA00100A.
- [130] H. Dong, X.X.-Y. Qu, L. Zhang, L.-H.L. Cheng, H.H.-L. Chen, C.-J.C. Gao, P. Taylor, H. Dong, L. Zhang, H.H.-L. Chen, X.X.-Y. Qu, L. Zhang, L.-H.L. Cheng, H.H.-L. Chen, C.-J.C. Gao, Preparation and characterization of surface-modified zeolite-polyamide thin film nanocomposite membranes for desalination, *Desalination and Water Treatment*. 34 (2011) 6–12.

- [131] J. Duan, Y. Pan, F. Pacheco, E. Litwiller, Z. Lai, I. Pinnau, High-performance polyamide thin-film-nanocomposite reverse osmosis membranes containing hydrophobic zeolitic imidazolate framework-8, *Journal of Membrane Science*. 476 (2015) 303–310. doi:10.1016/j.memsci.2014.11.038.
- [132] R. Pang, K. Zhang, Fabrication of hydrophobic fluorinated silica-polyamide thin film nanocomposite reverse osmosis membranes with dramatically improved salt rejection, *Journal of Colloid and Interface Science*. 510 (2018) 127–132. doi:10.1016/J.JCIS.2017.09.062.
- [133] J. Shen, C. Yu, H. Ruan, C. Gao, B. Van der Bruggen, Preparation and characterization of thin-film nanocomposite membranes embedded with poly(methyl methacrylate) hydrophobic modified multiwalled carbon nanotubes by interfacial polymerization, *Journal of Membrane Science*. 442 (2013) 18–26. doi:10.1016/J.MEMSCI.2013.04.018.
- [134] N. Misdan, W.J. Lau, A.F. Ismail, Seawater Reverse Osmosis (SWRO) desalination by thin-film composite membrane Current development, challenges and future prospects, *Desalination*. 287 (2012) 228–237.
- [135] H. Zhao, S. Qiu, L. Wu, L. Zhang, H. Chen, C. Gao, Improving the performance of polyamide reverse osmosis membrane by incorporation of modified multi-walled carbon nanotubes, *Journal of Membrane Science*. 450 (2014) 249–256. doi:10.1016/J.MEMSCI.2013.09.014.
- [136] M.T.M. Pendergast, J.M. Nygaard, A.K. Ghosh, E.M.V. Hoek, Using nanocomposite materials technology to understand and control reverse osmosis membrane compaction, *Desalination*. 261 (2010) 255–263. doi:10.1016/J.DESAL.2010.06.008.
- [137] E.M.V. Hoek, M.T.M. Pendergast, A.K. Ghosh, Nanotechnology-based membranes for water purification, in: *Nanotechnology Applications for Clean Water*, William Andrew Publishing, 2014: pp. 133–154. doi:10.1016/B978-1-4557-3116-9.00009-3.
- [138] G.L. Jadav, P.S. Singh, Synthesis of novel silica-polyamide nanocomposite membrane with enhanced properties, *Journal of Membrane Science*. 328 (2009) 257–267. doi:10.1016/J.MEMSCI.2008.12.014.
- [139] M. Namvar-Mahboub, M. Pakizeh, S. Davari, Preparation and characterization of UZM-5/polyamide thin film nanocomposite membrane for dewaxing solvent recovery, *Journal of Membrane Science*. 459 (2014) 22–32. doi:10.1016/J.MEMSCI.2014.02.014.
- [140] M.L. Lind, A.K. Ghosh, A. Jawor, X. Huang, W. Hou, Y. Yang, E.M. V Hoek, Influence of zeolite crystal size on zeolite-polyamide thin film nanocomposite membranes, *Langmuir*. 25 (2009) 10139–10145. doi:10.1021/la900938x.
- [141] M. Fathizadeh, A. Aroujalian, A. Raisi, Effect of added NaX nano-zeolite into polyamide as a top thin layer of membrane on water flux and salt rejection in a reverse osmosis process, *Journal of Membrane Science*. 375 (2011) 88–95. doi:10.1016/J.MEMSCI.2011.03.017.
- [142] T. Liu, F. Zhang, Y. Song, Y. Li, Revitalizing carbon supercapacitor electrodes with hierarchical porous structures, *Journal of Materials Chemistry A*. 5 (2017) 17705–17733. doi:10.1039/c7ta05646j.
- [143] N. Hao, L. Li, F. Tang, Facile preparation of ellipsoid-like MCM-41 with parallel channels along the short axis for drug delivery and assembly of Ag nanoparticles for catalysis, *Journal of Materials Chemistry A*. 2 (2014) 11565–11568. doi:10.1039/C4TA01820F.
- [144] E. Da'na, Adsorption of heavy metals on functionalized-mesoporous silica: A review, *Microporous and Mesoporous Materials*. 247 (2017) 145–157. doi:10.1016/j.micromeso.2017.03.050.
- [145] M. Vallet-Regí, M. Colilla, I. Izquierdo-Barba, M. Manzano, Mesoporous silica nanoparticles for drug delivery: Current insights, *Molecules (Basel, Switzerland)*. 23 (2017) 47. doi:10.3390/molecules23010047.

- [146] Y. Wang, Q. Zhao, N. Han, L. Bai, J. Li, J. Liu, E. Che, L. Hu, Q. Zhang, T. Jiang, S. Wang, Mesoporous silica nanoparticles in drug delivery and biomedical applications, *Nanomedicine: Nanotechnology, Biology and Medicine*. 11 (2015) 313–327. doi:10.1016/J.NANO.2014.09.014.
- [147] Q. Li, Z. Li, H. Yu, X. Pan, X. Wang, Y. Wang, J. Song, Effects of ordered mesoporous silica on the performances of composite nanofiltration membrane, *Desalination*. 327 (2013) 24–31. doi:10.1016/j.desal.2013.08.002.
- [148] D.L. Sparks, D.L. Sparks, Sorption phenomena on soils, *Environmental Soil Chemistry*. (2003) 133–186. doi:10.1016/B978-012656446-4/50005-0.
- [149] K.S.W. Sing, D.H. Everett, R.A.W. Haul, L. Moscou, R.A. Pierotti, J. Rouquerol, T. Siemieniewska, Reporting physisorption data for gas/solid systems, *Handbook of Heterogeneous Catalysis*. (2008). doi:10.1002/9783527610044.hetc0065.
- [150] J.S. Beck, K.D. Schmitt, J.B. Higgins, J.L. Schlenkert, J.C. Vartuli, W.J. Roth, M.E. Leonowicz, C.T. Kresge, C.T.W. Chu, D.H. Olson, E.W. Sheppard, A new family of mesoporous molecular sieves prepared with liquid crystal templates, *Journal of the American Chemical Society*. 114 (1992) 10834–10843. doi:10.1021/ja00053a020.
- [151] L.T. Gibson, Mesosilica materials and organic pollutant adsorption: Part A removal from air, *Chemical Society Reviews*. 43 (2014) 5163–5172. doi:10.1039/c3cs60096c.
- [152] V. Chiola, J.E. Ritsko, C.D. Vanderpool, Process for producing low-bulk density silica, US3556725A, 1971.
- [153] F. Di Renzo, H. Cambon, R. Dutartre, A 28-year-old synthesis of micelle-templated mesoporous silica, *Microporous Materials*. 10 (1997) 283–286. doi:10.1016/S0927-6513(97)00028-X.
- [154] T. Yanagisawa, T. Shimizu, K. Kuroda, C. Kato, The Preparation of Alkyltriethylammonium-Kaneinite Complexes and Their Conversion to Microporous Materials, *Bulletin of the Chemical Society of Japan*. 63 (1990) 988–992. doi:10.1246/bcsj.63.988.
- [155] T. Kimura, K. Kuroda, Ordered mesoporous silica derived from layered silicates, *Advanced Functional Materials*. 19 (2009) 511–527. doi:10.1002/adfm.200800647.
- [156] D. Zhao, Q. Huo, J. Feng, B.F. Chmelka, G.D. Stucky, Nonionic triblock and star diblock copolymer and oligomeric surfactant syntheses of highly ordered, hydrothermally stable, mesoporous silica structures, *Journal of the American Chemical Society*. 120 (1998) 6024–6036. doi:10.1021/ja974025i.
- [157] W. Stober, E. Bohn, Controlled growth of monodisperse silica spheres in the micron size range, *Journal of Colloid and Interface Science*. 26 (1968) 62–69. doi:10.1589/jpts.29.112.
- [158] S.H. Wu, H.P. Lin, Synthesis of mesoporous silica nanoparticles, *Chemical Society Reviews*. 42 (2013) 3862–3875. doi:10.1039/c3cs35405a.
- [159] A. Labidi, M. Serghini, S. Karoui, N. Ben Mustapha, J. Boubaker, A. Filali, Epilepsy, pemphigus and celiac disease: An exceptional association, *Tunisie Medicale*. 92 (2014) 585–586. doi:10.1155/2012/132424.
- [160] Z.A. Alothman, A review: Fundamental aspects of silicate mesoporous materials, *Materials*. 5 (2012) 2874–2902. doi:10.3390/ma5122874.
- [161] J. Wen, G.L. Wilkes, Organic/inorganic hybrid network materials by the sol-gel approach, *Chemistry of Materials*. 8 (1996) 1667–1681. doi:10.1021/cm9601143.
- [162] H.K. Schmidt, E. Geiter, M. Mennig, H. Krug, C. Becker, R.-P. Winkler, The sol-gel process for nano-technologies: New nanocomposites with interesting optical and mechanical properties, *Journal of Sol-Gel Science and Technology*. 13 (1998) 397–404. doi:10.1023/A:1008660909108.
- [163] C.A. Milea, C. Bogatu, A. Duță, The influence of parameters in silica sol-gel process, *Bulletin of the Transilvania University of Braşov Series I: Engineering Sciences*. 4

- (2011) 59–66. doi:10.1021/la402205j.
- [164] H.P. Lin, C.Y. Mou, Structural and morphological control of cationic surfactant-templated mesoporous silica, *Accounts of Chemical Research*. 35 (2002) 927–935. doi:10.1021/ar000074f.
- [165] P. Alexandridis, U. Olsson, B. Lindman, A record nine different phases (four cubic, two hexagonal, and one lamellar lyotropic liquid crystalline and two micellar solutions) in a ternary isothermal system of an amphiphilic block copolymer and selective solvents (water and oil), *Langmuir*. 14 (1998) 2627–2638. doi:10.1021/la971117c.
- [166] N.K. Raman, M.T. Anderson, C.J. Brinker, Template-based approaches to the preparation of amorphous, nanoporous silicas, *Chemistry of Materials*. 8 (1996) 1682–1701. doi:10.1021/cm960138+.
- [167] N. Pal, A. Bhaumik, Soft templating strategies for the synthesis of mesoporous materials: Inorganic, organic-inorganic hybrid and purely organic solids, *Advances in Colloid and Interface Science*. 189–190 (2013) 21–41. doi:10.1016/j.cis.2012.12.002.
- [168] Y. Wan, Zhao, On the Controllable Soft-Templating Approach to Mesoporous Silicates, *Chemical Reviews*. 107 (2007) 2821–2860. doi:10.1021/cr068020s.
- [169] W. Feng, L.-D. Sun, Y.-W. Zhang, C.-H. Yan, Synthesis and assembly of rare earth nanostructures directed by the principle of coordination chemistry in solution-based process, *Coordination Chemistry Reviews*. 254 (2010) 1038–1053. doi:10.1016/J.CCR.2010.02.007.
- [170] Y.T. Shi, H.Y. Cheng, Y. Geng, H.M. Nan, W. Chen, Q. Cai, B.H. Chen, X.D. Sun, Y.W. Yao, H. De Li, The size-controllable synthesis of nanometer-sized mesoporous silica in extremely dilute surfactant solution, *Materials Chemistry and Physics*. 120 (2010) 193–198. doi:10.1016/j.matchemphys.2009.10.045.
- [171] H. Yamada, C. Urata, S. Higashitamori, Y. Aoyama, Y. Yamauchi, K. Kuroda, Critical roles of cationic surfactants in the preparation of colloidal mesostructured silica, *ACS Applied Materials & Interfaces*. 6 (2014) 3491–3500. doi:10.1021/am405633r.
- [172] X. Lv, L. Zhang, F. Xing, H. Lin, Controlled synthesis of monodispersed mesoporous silica nanoparticles: Particle size tuning and formation mechanism investigation, *Microporous and Mesoporous Materials*. 225 (2016) 238–244. doi:10.1016/j.micromeso.2015.12.024.
- [173] M. Yu, L. Zhou, J. Zhang, P. Yuan, P. Thorn, W. Gu, C. Yu, A simple approach to prepare monodisperse mesoporous silica nanospheres with adjustable sizes, *Journal of Colloid and Interface Science*. 376 (2012) 67–75. doi:10.1016/J.JCIS.2012.03.014.
- [174] Y. Chiang, H. Lian, S. Leo, S. Wang, Y. Yamauchi, K. Wu, Controlling particle size and structural properties of mesoporous silica nanoparticles using the taguchi method, *The Journal of Physical Chemistry C*. 115 (2011) 13158–13165. doi:10.1021/jp201017e.
- [175] B.G. Cha, J.H. Jeong, J. Kim, Extra-Large Pore Mesoporous Silica Nanoparticles Enabling Co-Delivery of High Amounts of Protein Antigen and Toll-like Receptor 9 Agonist for Enhanced Cancer Vaccine Efficacy, *ACS Central Science*. 4 (2018) 484–492. doi:10.1021/acscentsci.8b00035.
- [176] F.K. Crundwell, On the mechanism of the dissolution of quartz and silica in aqueous solutions, *ACS Omega*. 2 (2017) 1116–1127.
- [177] G.S. Lai, W.J. Lau, S.R. Gray, T. Matsuura, R.J. Gohari, M.N. Subramanian, S.O. Lai, C.S. Ong, A.F. Ismail, D. Emazadah, A practical approach to synthesize polyamide thin film nanocomposite (TFN) membranes with improved separation properties for water/wastewater treatment, *Journal of Materials Chemistry A*. 4 (2016) 4134–4144.
- [178] H. Wu, B. Tang, P. Wu, Optimizing polyamide thin film composite membrane covalently bonded with modified mesoporous silica nanoparticles, *Journal of Membrane Science*. 428 (2013) 341–348. doi:10.1016/j.memsci.2012.10.053.
- [179] G. Zhu, M. Bao, Z. Liu, C. Gao, Preparation of spherical mesoporous aminopropyl-

- functionalized MCM-41 and its application in polyamide thin film nanocomposite reverse osmosis membranes, *Desalination and Water Treatment*. 57 (2016) 25411–25420. doi:10.1080/19443994.2016.1156028.
- [180] J.L. Paris, M. Colilla, I. Izquierdo-Barba, M. Manzano, M. Vallet-Regí, Tuning mesoporous silica dissolution in physiological environments: a review, *Journal of Materials Science*. 52 (2017) 8761–8771. doi:10.1007/s10853-017-0787-1.
- [181] I. Izquierdo-Barba, M. Colilla, M. Manzano, M. Vallet-Regí, In vitro stability of SBA-15 under physiological conditions, *Microporous and Mesoporous Materials*. 132 (2010) 442–452.
- [182] T. Yokoi, H. Yoshitake, T. Tatsumi, Synthesis of amino-functionalized MCM-41 via direct co-condensation and post-synthesis grafting methods using, *Materials Science*. (2004) 951–957.
- [183] J.Y. Lee, C.H. Chen, S. Cheng, H.Y. Li, Adsorption of Pb(II) and Cu(II) metal ions on functionalized large-pore mesoporous silica, *International Journal of Environmental Science and Technology*. 13 (2016) 65–76. doi:10.1007/s13762-015-0841-y.
- [184] X.S. Zhao, G.Q. Lu, Modification of MCM-41 by surface silylation with trimethylchlorosilane and adsorption study, *The Journal of Physical Chemistry B*. 102 (1998) 1556–1561. doi:10.1021/jp972788m.
- [185] S. Huh, J.W. Wiench, B.G. Trewyn, S. Song, M. Pruski, V.S.-Y. Lin, Tuning of particle morphology and pore properties in mesoporous silicas with multiple organic functional groups, *Chem. Commun.* (2003) 2364–2365. doi:10.1039/B306255D.
- [186] P. Silberzan, L. Leger, D. Ausserre, J.J. Benattar, Silanation of silica surfaces. A new method of constructing pure or mixed monolayers, *Langmuir*. 7 (1991) 1647–1651. doi:10.1021/la00056a017.
- [187] F. de Juan, E. Ruiz-Hitzky, Selective functionalization of mesoporous silica, *Advanced Materials*. 12 (2000) 430–432. doi:10.1002/(SICI)1521-4095(200003)12:6<430::AID-ADMA430>3.0.CO;2-3.
- [188] D.S. Shephard, W. Zhou, T. Maschmeyer, J.M. Matters, C.L. Roper, S. Parsons, B.F.G. Johnson, M.J. Duer, Site-directed surface derivatization of MCM-41: Use of high-resolution transmission electron microscopy and molecular recognition for determining the position of functionality within mesoporous materials, *Angewandte Chemie International Edition*. 37 (1998) 2719–2723. doi:10.1002/(SICI)1521-3773(19981016)37:19<2719::AID-ANIE2719>3.0.CO;2-6.
- [189] M.H. Lim, A. Stein, Comparative studies of grafting and direct syntheses of inorganic–organic hybrid mesoporous materials, *Chemistry of Materials*. 11 (1999) 3285–3295. doi:10.1021/cm990369r.
- [190] M. Bouchoucha, R. C.-Gaudreault, M.-A. Fortin, F. Kleitz, Mesoporous silica nanoparticles: selective surface functionalization for optimal relaxometric and drug loading performances, *Advanced Functional Materials*. 24 (2014) 5911–5923.
- [191] Q. Cai, Z.-S.S. Luo, W.-Q.Q. Pang, Y.-W.W. Fan, X.-H.H. Chen, F.-Z.Z. Cui, Dilute solution routes to various controllable morphologies of MCM-41 silica with a basic medium, *Chemistry of Materials*. 13 (2001) 258–263. doi:10.1021/cm990661z.
- [192] V. Loryuenyong, T. Muanghom, T. Apinyanukul, P. Rutthongjan, Synthesis of templated mesoporous silica nanoparticles under base catalysis, *Advances in Applied Ceramics*. (2011). doi:10.1179/1743676111Y.0000000024.
- [193] A. Hakeem, R. Duan, F. Zahid, C. Dong, B. Wang, F. Hong, X. Ou, Y. Jia, X. Lou, F. Xia, Dual stimuli-responsive nano-vehicles for controlled drug delivery: Mesoporous silica nanoparticles end-capped with natural chitosan, *Chemical Communications*. 50 (2014) 13268–13271. doi:10.1039/c4cc04383a.
- [194] A.E.G. Berg, L.S. Clesceri, A.D. Eaton, Standard methods for the examination of water and wastewater, 22nd ed., American Public Health Association, 2012.

- [195] T. Coradin, D. Eglin, J. Livage, The silicomolybdc acid spectrophotometric method and its application to silicate/biopolymer interaction studies, *Spectroscopy*. 18 (2004) 567–576. doi:10.1155/2004/356207.
- [196] E.M. Combatt Caballero, D. Palacio Badel, M. Palencia Luna, Organic acids to eliminate interference by phosphorus in the analysis of silicon by molecular absorption, *Revista Facultad Nacional de Agronomía*. 70 (2017) 8183–8189. doi:10.15446/rfna.v70n2.64523.
- [197] T. Kamada, T. Ohara, T. Shintani, T. Tsuru, Controlled surface morphology of polyamide membranes via the addition of co-solvent for improved permeate flux, *Journal of Membrane Science*. 467 (2014) 303–312. doi:10.1016/j.memsci.2014.03.072.
- [198] A.P. GmbH, SurPASS Operating Procedures, Anton Paar GmbH, Graz, Austria, 2012.
- [199] T.J.V. Prazeres, M. Beija, F. V. Fernandes, P.G.A. Marcelino, J.P.S. Farinha, J.M.G. Martinho, Determination of the critical micelle concentration of surfactants and amphiphilic block copolymers using coumarin 153, *Inorganica Chimica Acta*. 381 (2012) 181–187. doi:10.1016/J.ICA.2011.09.013.
- [200] C.T. Kresge, M.E. Leonowicz, W.J. Roth, J.C. Vartuli, J.S. Beck, Ordered mesoporous molecular sieves synthesized by a liquid-crystal template mechanism, *Nature*. 359 (1992) 710. <https://doi.org/10.1038/359710a0>.
- [201] W. Sangchoom, R. Mokaya, High temperature synthesis of exceptionally stable pure silica MCM-41 and stabilisation of calcined mesoporous silicas via refluxing in water, *Journal of Materials Chemistry*. 22 (2012) 18872–18878. doi:10.1039/C2JM33837H.
- [202] M.R. Mello, D. Phanon, G.Q. Silveira, P.L. Llewellyn, C.M. Ronconi, Amine-modified MCM-41 mesoporous silica for carbon dioxide capture, *Microporous and Mesoporous Materials*. 143 (2011) 174–179. doi:10.1016/J.MICROMESO.2011.02.022.
- [203] G. Berlier, L. Gastaldi, S. Sapino, I. Miletto, E. Bottinelli, D. Chirio, E. Ugazio, MCM-41 as a useful vector for rutin topical formulations: Synthesis, characterization and testing, *International Journal of Pharmaceutics*. 457 (2013) 177–186. doi:10.1016/J.IJPHARM.2013.09.018.
- [204] M. Pirouzmand, B. Nikzad-kojanag, S.K. Seyed-Rasulzade, Surfactant containing Ca/MCM-41 as a highly active, green and reusable catalyst for the transesterification of canola oil, *Catalysis Communications*. 69 (2015) 196–201. doi:10.1016/J.CATCOM.2015.06.021.
- [205] I.M. Tidswell, B.M. Ocko, P.S. Pershan, S.R. Wasserman, G.M. Whitesides, J.D. Axe, X-ray specular reflection studies of silicon coated by organic monolayers (alkylsiloxanes), *Physical Review B*. 41 (1990) 1111.
- [206] Q. Wei, Z.-X. Zhong, Z.-R. Nie, J.-L. Li, F. Wang, Q.-Y. Li, Catalytically active gold nanoparticles confined in periodic mesoporous organosilica (PMOs) by a modified external passivation route, *Microporous and Mesoporous Materials*. 117 (2009) 98–103. doi:10.1016/J.MICROMESO.2008.06.033.
- [207] K.Y. Chow, D.J.W. Grant, Surface analysis of griseofulvin powders by krypton adsorption: Evaluation of specific surface area, BET constant C and polanyi adsorption potential, *Powder Technology*. 56 (1988) 209–223. doi:10.1016/0032-5910(88)80031-7.
- [208] B.J.A. Tarboush, D. Rana, T. Matsuura, H.A. Arafat, R.M. Narbaitz, Preparation of thin-film-composite polyamide membranes for desalination using novel hydrophilic surface modifying macromolecules, *Journal of Membrane Science*. 325 (2008) 166–175.
- [209] H.A. Shawky, S.-R. Chae, S. Lin, M.R. Wiesner, Synthesis and characterization of a carbon nanotube/polymer nanocomposite membrane for water treatment, *Desalination*. 272 (2011) 46–50. doi:10.1016/J.DESAL.2010.12.051.
- [210] A. Peyki, A. Rahimpour, M. Jahanshahi, Preparation and characterization of thin film composite reverse osmosis membranes incorporated with hydrophilic SiO₂

- nanoparticles, *Desalination*. 368 (2015) 152–158. doi:10.1016/J.DESAL.2014.05.025.
- [211] J. Deere, E. Magner, J.G. Wall, B.K. Hodnett, Mechanistic and structural features of protein adsorption onto mesoporous silicates, *The Journal of Physical Chemistry B*. 106 (2002) 7340–7347. doi:10.1021/jp0139484.
- [212] S. Yu, X. Liu, J. Liu, D. Wu, M. Liu, C. Gao, Surface modification of thin-film composite polyamide reverse osmosis membranes with thermo-responsive polymer (TRP) for improved fouling resistance and cleaning efficiency, *Separation and Purification Technology*. 76 (2011) 283–291. doi:10.1016/J.SEPPUR.2010.10.017.
- [213] M. Zargar, Y. Hartanto, B. Jin, S. Dai, Understanding functionalized silica nanoparticles incorporation in thin film composite membranes: Interactions and desalination performance, *Journal of Membrane Science*. 521 (2017) 53–64.
- [214] Y. Tardy, The chemistry of silica solubility, polymerization, colloid and surface properties, and biochemistry, Ralf K. Iler, 1979, *Sciences Géologiques, Bulletins et Mémoires*. 35 (1982) 93.
- [215] V.W. Truesdale, J.E. Greenwood, A. Rendell, The rate-equation for biogenic silica dissolution in seawater--new hypotheses, *Aquatic Geochemistry*. 11 (2005) 319–343.
- [216] K. Braun, A. Pochert, M. Beck, R. Fiedler, J. Gruber, M. Lindén, Dissolution kinetics of mesoporous silica nanoparticles in different simulated body fluids, *Journal of Sol-Gel Science and Technology*. 79 (2016) 319–327.
- [217] B. Marler, U. Oberhagemann, S. Vortmann, H. Gies, Influence of the sorbate type on the XRD peak intensities of loaded MCM-41, *Microporous Materials*. 6 (1996) 375–383. doi:10.1016/0927-6513(96)00016-8.
- [218] S.M. Alahmadi, S. Mohamad, M.J. Maah, Synthesis and characterization of mesoporous silica functionalized with calix[4]arene derivatives, *International Journal of Molecular Sciences*. 13 (2012) 13726–13736. doi:10.3390/ijms131013726.
- [219] K. Möller, J. Kobler, T. Bein, Colloidal suspensions of nanometer-sized mesoporous silica, *Advanced Functional Materials*. 17 (2007) 605–612.
- [220] B. Gouze, J. Cambedouzou, S. Parres-Maynadie, D. Rébiscoul, How hexagonal mesoporous silica evolves in water on short and long term: Role of pore size and silica wall porosity, *Microporous and Mesoporous Materials*. 183 (2014) 168–176.
- [221] J.G. Croissant, Y. Fatiev, N.M. Khashab, Degradability and clearance of silicon, organosilica, silsesquioxane, silica mixed oxide, and mesoporous silica nanoparticles, *Advanced Materials*. 29 (2017) 1604634. doi:10.1002/adma.201604634.
- [222] P. Aimar, M. Meireles, V. Sanchez, A contribution to the translation of retention curves into pore size distributions for sieving membranes, *Journal of Membrane Science*. 54 (1990) 321–338.
- [223] J. Chen, Q. Li, R. Xu, F. Xiao, Distinguishing the silanol groups in the mesoporous molecular sieve MCM-41, *Angewandte Chemie International Edition in English*. 34 (1996) 2694–2696.
- [224] M. Prokopowicz, J. Żeglinski, A. Szewczyk, A. Skwira, G. Walker, Surface-activated fibre-like SBA-15 as drug carriers for bone diseases, *AAPS PharmSciTech*. 20 (2019) 17.
- [225] H. Chen, W.S. Hung, C.H. Lo, S.H. Huang, M.L. Cheng, G. Liu, K.R. Lee, J.Y. Lai, Y.M. Sun, C.C. Hu, R. Suzuki, T. Ohdaira, N. Oshima, Y.C. Jean, Free-volume depth profile of polymeric membranes studied by positron annihilation spectroscopy: layer structure from interfacial polymerization, *Macromolecules*. 40 (2007) 7542–7557.
- [226] L. Xia, J. Ren, M. Weyd, J.R. McCutcheon, Ceramic-supported thin film composite membrane for organic solvent nanofiltration, *Journal of Membrane Science*. 563 (2018) 857–863. doi:10.1016/J.MEMSCI.2018.05.069.
- [227] A.S. Stillwell, M.E. Webber, Predicting the specific energy consumption of reverse osmosis desalination, *Water (Switzerland)*. 8 (2016) 1–18. doi:10.3390/w8120601.

Appendix A

List of Tables

Table 1-1: Specific energy consumption (SEC) for desalinating raw water with concentration of 35,000 mg/L at 50% recovery and < 500 ppm product water quality by different desalination technologies	2
<i>Table 2-1: Pressure driven membranes characterizations</i>	7
<i>Table 2-2: Feedwater characterization by TDS content</i>	8
Table 2-3: Additives and their influence on PA TFC membrane performance	20
Table 2-4: Overview of filler materials in TFN membranes and comparison of their performance with control TFC membranes; ↑, ↓ and ↔ indicate an increase, decrease, and remain same, respectively. All membranes were tested in NaCl (2000 ppm) except [131] in brackish water	25
Table 3-1: Materials and chemicals used for preparation, functionalization, and determination of dissolved concentration of MSN.....	46
Table 3-2: Materials and chemicals used for preparation, characterization, and performance evaluation of the membranes.....	47
Table 4-1: Particle size of synthesized MSN from analysis of SEM images and DLS measurements of aqueous dispersions depending on the molar ratio of CTAB to TEOS	62
Table 4-2: Organic content and estimated surface density of OTS for LMSN and HMSN.....	67
Table 4-3: Overview on data for pore structure characterization for LMSN and HMSN obtained after functionalization at different OTS concentrations	70
Table 4-4: Maximum thickness of LMSN layer deposited on base PES membrane before IP, estimated from effective density of NPs powder measured by mercury porosimetry as well as concentration and volume of nanoparticle dispersion applied to the membrane sample area .	83
Table 4.5: A performance comparison of TFN membranes in the literatures to this work	85
Table 4.6: Particle size analysis of the different silica NPs before and after partial dissolution in aqueous solution at pH 9	90
Table 4.7: Characteristic porosity data of unfunctionalized and OTS-functionalized MSN before and after 170 h exposure at room temperature in water at pH 9, obtained from nitrogen adsorption measurement.....	93
Table 4.8: Relative variations of permeance and salt rejection for all membranes during 240 h filtration of NaCl solution at pH 5 and pH 9, (+) sign means parameter increase and (-) sign means parameter decrease.	95
Table 4.9: Average hydrodynamic diameter of different dextrans used in filtration experiments	99
Table 4.10: BET surface area and pore diameter of LMSN and HMSN obtained after functionalization at different MTS concentrations.....	100
Table 4.11: Decline of surface area for functionalized MSN with MTS and OTS.....	100
Table 4.12: Organic content and estimated surface density of MTS for LMSN and HMSN	101

List of Figures

Figure 1.1: Typical Seawater RO plant cost composition	2
Figure 1.2: Scheme illustrating the incorporation of different MSN nanofillers inside the PA layer and the structure of functionalized MSN	4
Figure 2.1: Total capacity installed by different desalination technologies. RO: Reverse Osmosis; MSF: Multi-stage flash; MED: Multi-effect distillation; ED/EDR: Electrodialysis/Electrodialysis Reversal; NF/SR: Nanofiltration/Sulfate Removal.	9
Figure 2.2: Schematic showing the water flow direction across the FO and RO membranes ..	9
Figure 2.3: Schematic of the TFC membrane structure and its composition.....	11
Figure 2.4: Schematic illustration of possible molecular structure of network and aggregate pores in aromatic PA TFC membranes synthesized by reaction of MPD and TMC	13
Figure 2.5: Schematic diagram illustrating the shielding of Donnan potential due to a) high feed salinity and b) divalent cations. The figure adapted from	15
Figure 2.6: (a) SEM of the top PA surface, (b) the back side of the PA layer, (c) high magnification SEM image of the top PA surface and (d) schematic illustration for cross-sectional morphology of PA film	17
Figure 2.7: Schematic of preparation of AQP-based hollow fiber membrane	23
Figure 2.8: Scheme illustrating the structure of TFN membranes	24
Figure 2.9: Schematic representation of preparation of TFN membranes by pre-seeding approach from	27
Figure 2.10: Schematic representation of (a) the evaporation-controlled filler positioning (EFP) and (b) the conventional TFN membrane preparation methods adapted from	28
Figure 2.11: Schematic diagram for the types of interaction between the NPs and the PA matrix	30
Figure 2.12: IUPAC classification of pores based on pore width	31
Figure 2.13: Schematic figure illustrating the definition of adsorbent, adsorbate and adsorptive	32
Figure 2.14: The six main types of adsorption isotherms according to IUPAC classification	32
Figure 2.15: Structure of mesoporous M41S materials: (a) hexagonal MCM-41, (b) cubic MCM-48 and (c) lamellar MCM-50	34
Figure 2.16: Scheme illustrating the sol-gel general reactions	35
Figure 2.17: Effect of pH on the silica condensation rate, charge properties and charge density on the surface of the silica species	37
Figure 2.18: Surfactant molecule and its behavior in water	37
Figure 2.19: Chemical structure of some common surfactants	39
Figure 2.20: Formation of mesoporous structure: (a) cooperative self-assembly and (b) true liquid crystal templating process	40
Figure 2.21: Formation of mesoporous structure: (a) cooperative self-assembly and (b) true liquid crystal templating process	43
Figure 2.22: Schematic representation of the silanization reaction process using trichlorosilane molecules.....	43
Figure 2.23: Methods of selective grafting on external and internal surfaces of MSN; the first method proposed by De Juan and Ruitz-Hitzky and the second method proposed by Shephard et al.	45
Figure 3.1: Schematic diagram illustrating preparation and functionalization of MSN	49
Figure 3.2: Image of (a) computer-controlled casting machine, and (b) coagulation bath	53

Figure 3.3: Schematic diagram for PA TFN membrane preparation	54
Figure 3.4: Illustration of (a) the glass module, and (b) the rubber roller used in PA preparation	55
Figure 3.5: Dead-end filtration cell	57
Figure 3.6: Cross-flow filtration cell	58
Figure 4.1: Schematic preparation of MSN via sol-gel process	59
Figure 4.2: SEM images of MSN obtained at different CTAB/TEOS molar ratios: a) 0.018, b) 0.035, c) 0.054, d) 0.1 and e) 0.18	60
Figure 4.3: TEM micrograph of MSN prepared with different CTAB/TEOS molar ratio	61
Figure 4.4: (a) small angle XRD for MSN and (b) nitrogen adsorption isotherm at standard temperature and pressure (STP) as well as estimated pore size distribution (inset) of MSN. .	63
Figure 4.5: (a) FTIR spectra and (b) TGA of as-synthesized, calcinated and solvent-extracted MSN	64
Figure 4.6: Dispersibility of (a) unfunctionalized MSN and (b) OTS-functionalized MSN in n-hexane; left: Image just after shaking the bottles; right: image after 30 minutes of sonication	64
Figure 4.7: Schematic representation for the surface functionalization of MSN (OTS grafting inside the pores leads to their water “hating” character: HMSN; preventing OTS grafting inside the pores leads to water “loving” character: LMSN)	65
Figure 4.8: FTIR spectra for a) LMSN, b) HMSN, each obtained at different concentration of OTS (OTS/MSN ratio = 0.5 - 5 w/w) during the functionalization	66
Figure 4.9: Thermogravimetric analysis of unfunctionalized MSN and functionalized LMSN and HMSN with different OTS content	66
Figure 4.10: Nitrogen adsorption isotherms of (a) LMSN, (b) HMSN, obtained by using different OTS concentration, along with the data for unmodified MSN, and (c) Detailed view on nitrogen adsorption isotherms for HMSN	69
Figure 4.11: Scheme illustrating the two scenarios of pore blocking in HMSN in	71
Figure 4.12: ATR FT-IR spectra of TFC and TFN membranes at different LMSN loading (functionalized with 0.5 w/w OTS)	73
Figure 4.13: Effect of OTS concentration during MSN functionalization on the water contact angle of TFN membranes: a) with LMSN and b) with HMSN. The NPs loading in TFN membranes is 0.01 w/v%	74
Figure 4.14: Effect of OTS concentration during MSN functionalization on the zeta potential of TFN membranes: a) with LMSN and b) with HMSN. The NPs loading in TFN membranes is 0.01 w/v%	75
Figure 4.15: Effect of OTS concentration during MSN functionalization on the permeability and NaCl rejection of TFN membranes prepared at NPs loading of 0.01 w/v%: a) LMSN and b) HMSN	76
Figure 4.16: Effect of OTS concentration during MSN functionalization on: a) pure water permeability; b) pure ethanol permeability; for TFN membranes prepared at fixed NP loading (0.01 w/v%); data for TFC membranes prepared under identical conditions for comparison. .	77
Figure 4.17: Effect of MSN pores hydrophilicity on the rate of membrane wettability change; TFN membranes prepared using either LMSN or HMSN at fixed NP loading (0.01 w/v%), OTS concentration during MSN functionalization was 0.5 w/w	78
Figure 4.18: Effect of LMSN (OTS concentration during MSN functionalization 0.5 w/w) loading in TFN membranes on: a) zeta potential as a function of pH; b) water contact angle	80

Figure 4.19: Effect of LMSN (OTS concentration during MSN functionalization 0.5 w/w) loading in TFN membranes on permeability and NaCl rejection during desalination.....	81
Figure 4.20: Top surface SEM images at different magnifications of TFC and TFN membranes with different LMSN loading (OTS concentration during functionalization 0.5 w/w)	82
Figure 4.21: SEM cross-section images of TFC and TFN membranes with different loading of LMSN (OTS concentration during MSN functionalization 0.5 w/v%)	83
Figure 4.22: Permeance and NaCl rejection during RO experiments (2 g/L NaCl in water as feed) of TFC and TFN membranes. The NP loading for TFN membranes is 0.005 w/v%	84
Figure 4.23: SEM of the top surface of MSN_TFN membrane at 0.005 w/v% loading.....	84
Figure 4.24: Dissolution of MSN, LMSN and HMSN at (a) pH 5 and (b) pH 9. The initial solid concentration was 2 g/L and the initial pH was adjusted using HCl and NaOH to pH 5 and pH 9, respectively.....	85
Figure 4.25: Plots of $\ln(C_0 - C_t/C_0)$ vs. time to calculate the dissolution rate constant of MSN (a,b), LMSN (c,d) and HMSN (e,f) at pH 5 and pH 9, respectively	87
Figure 4.26: Rate constant of dissolution of MSN, LMSN and HMSN during the first 12 hours of the experiments at pH 5 and pH 9.....	88
Figure 4.27_ Small angle XRD of the native MSN (a, b), LMSN (c,d) and HMSN (e,f) before and after the partially dissolved in water at pH 9 after 170 hours, respectively	89
Figure 4.28: SEM micrograph of the native MSN (a, b), LMSN (c,d) and HMSN (e,f) before and after the partial dissolution in water at pH 9 after 170 hours, respectively	91
Figure 4.29: SEM micrograph of the native MSN (a, b), LMSN (c,d) and HMSN (e,f) before and after the partial dissolution in water at pH 9 after 170 hours, respectively	92
Figure 4.30: Nitrogen adsorption isotherms (a, c and e) and derived pore size distributions (b, d and f) of native and partially dissolved MSN, LMSN and HMSN after 170 hours at pH 9, respectively.....	94
Figure 4.31: Long-term separation performance of TFC and TFN membranes for first 120 h at pH 5 (a, b) and for second 120 h at pH 9 (c, d) using the same membrane.	96
Figure 4.32: SEM images of TFC and TFN membranes before and after filtration of NaCl solution for 120 hours at pH 5 and thereafter 120 hours at pH 9.....	97
Figure 4.33: Rejection of dextran with different average molecular weight (4 kDa - 2000 kDa; feed concentration 1 g/L in water) for a) the native membranes and b) the previously tested membranes for desalination performance for 120 h at pH 5 and 120 h at pH 9 (cf.....	99
Figure 4.34: TGA of unfunctionalized MSN and functionalized LMSN and HMSN with different MTS content	101
Figure 4.35: Effect of MTS concentration during MSN functionalization on the permeability and NaCl rejection of TFN membranes prepared at NPs loading of 0.01 w/v%: a) LMSN and b) HMSN	103
Figure 4.36: Effect of LMSN (MTS concentration during MSN functionalization 0.5 w/w) loading in TFN membranes on permeability and NaCl rejection during desalination.....	103
Figure 4.37: Long-term separation performance of LMSN_ TFN membranes with 0.5 w/w MTS for 120 h at pH 5 and 120 h at pH 9 using the same membrane	104

List of Equations

Equation 2.1: Fick's law of diffusion	13
Equation 2.2: Water flux in RO membrane according to solution-diffusion model	14
Equation 2.3: Salt flux in RO membrane according to solution-diffusion model.....	14
Equation 2.4: Van't Hoff equation.....	14
Equation 2.5: Calculation of salt rejection	14
Equation 3.1: Calculation of dissolved silica concentration	50
Equation 3.2: calculation of number of grafted OTS molecules per nm ²	52
Equation 3.3: Calculation of number of OTS moles	52
Equation 3.4: Calculation of weight loss %	52
Equation 3.5: Calculation of surface area	52
Equation 3.6: Calculation of the mass of SiO ₂	52
Equation 3.7: Helmholtz-Smoluchowski equation.....	55
Equation 3.8: Pure liquid permeability	56
Equation 3.9: Calculation of permeance under RO conditions	57
Equation 4.1: Bragg's equation	62
Equation 4.2: Caluclation of the unit cell.....	62
Equation 4.3: First-order rate constant equation	86

Abbreviations

(In order of appearance in text)

PA	Polyamide
NPs	Nanoparticles
TFN	Thin film nanocomposite
MSN	Mesoporous silica nanoparticles
OTS	Octadecyltrichlorosilane
MTS	Methyltrichlorosilane
IP	Interfacial polymerization
TFC	Thin film composite
WWDR	World water development report
TDS	Total dissolved solid
WHO	World health organization
RO	Reverse osmosis
SEC	Specific Energy Consumption
KWh	Kilowatt-hours
BWRO	Brackish water reverse osmosis
SWRO	Seawater reverse osmosis
ED	Electrodialysis
EDR	Electrodialysis reversal
MVC	Mechanical vapor compression
FO	Forward osmosis
MD	Membrane distillation
MSF	Multi-stage flash;
MED	Multiple effect distillation
MEB	Multi-effect boiling.
LMSN	Hydrophilic pores mesoporous silica nanoparticles
HMSN	Hydrophobic pores mesoporous silica nanoparticles
ppm	Part per million
TVC	Thermal vapor compression
NF/SR	Nanofiltration/Sulfate Removal
PSf	Polysulfone
MPD	m-phenylene diamine
TMC	1,3,5-benzenetricarbonyl trichloride or (tri- mesoyl chloride)
PALS	Positron annihilation lifetime spectroscopy
PFM	Pore-flow model
SDM	Solution-diffusion model
J_w	Water flux
J_s	Salt flux
C_{feed}	Solute concentration in feed solution
C_{permeate}	Solute concentration in permeate solution
π	Osmotic pressure
ΔP	Transmembrane pressure
C	Molar concentration of salt in feed solution
R	Universal gas constant
T	Absolute temperature
IEP	Isoelectric point

PIP	Piperazine
TEA	Triethylamine
IPA	Isopropyl alcohol
HMPA	Hexamethyl phosphoramidate
DMSO	Dimethylsulfoxide
CSA	Camphor sulfonic acid
DMF	N,N-Dimethylformamide
PES	Polyethersulfone
PEG	Polyethylene glycol
GA	Glutaraldehyde
AQPs	Aquaporins
MMMs	Mixed matrix membranes
OSN	Organic solvent nanofiltration
Ag	Silver
TiO ₂	Titanium dioxide
SiO ₂	Silicon dioxide
APTES	Aminopropyltriethoxysilane
MOF	Metal–organic frameworks
GO	Graphene oxide
N-GOQD	Nitrogen-doped graphene oxide quantum dots
CNTs	Carbon nanotubes
EFP	Evaporation-controlled filler positioning
IUPAC	International union of pure and applied chemistry
P/Po	Relative pressure
CnTMA	Alkyltrimethylammonium bromide
MCM-41	Mobil composition of matter No. 41
TEOS	Tetraethyl orthosilicate
SBA-15	Santa Barbara amorphous No. 15
TMOS	Tetramethyl orthosilicate
CTAB	Cetyltrimethylammonium bromide
LCT	Liquid crystal templating
CMC	Critical micelle concentration
SDS	Sodium dodecyl sulphate
CSA	Cooperative self-assembly
H ₂ O ₂	Hydrogenperoxide
MeOH	Methanol
DLS	Dynamic light scattering
XRD	X-ray powder diffractometer
BET	Brunauer–Emmett–Teller
DFT	Density functional theory
MPa	Megapascal
SEM	Scanning electron microscopy
TEM	Transmission electron microscopy
FEG	Field emission gun
ATR-FTIR	Attenuated total reflectance-Fourier transform infrared
OC	Organic content
TGA	Thermogravimetric analysis
N _{OTS}	Number of the alkyl group of OTS molecules per square nanometer
n _A	Number of moles of grafted OTS molecules

NA	Avogadro's constant
S	Surface area
M ₂₀₀	Residual weight of the sample at 200 °C
M ₆₀₀	Residual weight of the sample at 600 °C
MCH	Molecular weight of C18 chain of OTS
SBET-SiO ₂	BET surface area of SiO ₂
MOTS	Group weight of grafted OTS on the silica surface
VIPS	Vapor induced phase separation
NMP	N-methyl-2-pyrrolidone
PVP	Polyvinylpyrrolidone
RH	Relative humidity
DI	Deionized
ζ	Zeta potential
η	Electrolyte viscosity
ε ₀	Vacuum permittivity
ε	Dielectric coefficient
L	Length of the streaming channel
A	Cross section of the streaming channel
CA	Contact angle
m	Mass of a permeate
ρ	Liquid density
kDa	Kilodalton
PDI	Polydispersity index
λ	Wavelength
a ₀	The repeat distance between two pore centres in MSN (the unit cell)
d _p	Average pore diameter
V _p	Pore volume

Appendix B

Curriculum vitae

The CV is not included in the online version for privacy reasons

The CV is not included in the online version for privacy reasons